

AB INITIO COMPUTATIONAL APPLICATIONS OF ELECTRONIC STRUCTURE
AND SPECTROSCOPIC PROPERTIES OF BULK CRYSTALLINE MATERIALS

DISSERTATION IN
Physics
And
Chemistry

Presented to the Faculty of the University
of Missouri-Kansas City in partial fulfillment of
the requirements for the degree

DOCTOR OF PHILOSOPHY

By
Liaoyuan Wang

B.Sc., University of Science and Technology of China, 2001
M.Sc., University of Science and Technology of China, 2006
M.Sc., University of Missouri – Kansas City, 2010

Kansas City, Missouri
2013

© 2013

LIAOYUAN WANG

ALL RIGHTS RESERVED

AB INITIO COMPUTATIONAL APPLICATIONS TO ELECTRONIC STRUCTURE
AND SPECTROSCOPIC PROPERTIES OF BULK CRYSTALLINE MATERIALS

Liaoyuan Wang, Candidate for the Doctor of Philosophy Degree

University of Missouri – Kansas City, 2013

ABSTRACT

Boron-rich compounds and elemental boron have amazing chemical, physical and mechanical properties, but puzzling structures. The uncertain stoichiometric value of foreign elements in boron-rich compounds greatly influences the physical and chemical properties. To study this effect, pure elemental boron which has six allotropes (α -r-B₁₂, γ -B₂₈, α -t-B₅₁, β -r-B₁₀₆, β -t-B₁₉₀, and α -Ga type) reasonably becomes a suitable candidate. In this work, the electronic structures and spectroscopic properties [x-ray absorption near edge structure (XANES) and optical dielectric functions] of elemental boron were systematically studied using an *ab initio* orthogonalized linear combination of atomic orbitals (OLCAO) method. Based on available experimental data, the calculated electronic structure, dielectric functions and XANES spectra reproduce the experimental measurements very well.

Electronic structures show that α -r-B₁₂, γ -B₂₈, β -r-B₁₀₆, B₁₁C-CBC and B₁₂O₂ are indirect semiconductors; α -t-B₅₁, β -t-B₁₉₀ and α -Ga type boron are metallic or semi-metallic materials. Based on the electronic structures of α -Ga type and β -t-B₁₉₀, they both probably have poor conductivity; however the mechanisms are very different: the density of states of α -Ga type shows that there is a pseudogap existing, while the band structure of β -t-B₁₉₀ at the Fermi level shows very few flat states existing.

By investigating the XANES spectra for a series of perfect icosahedra built up with different bond lengths, XANES spectra of icosahedra in crystal structure of α -r-B₁₂, γ -B₂₈, α -t-B₅₁, β -r-B₁₀₆, and β -t-B₁₉₀ all have three dominant characteristic peak features in the energy range of 195-215eV. This result was also observed in the ico-XANES spectra of B₁₁C-CBC and B₁₂O₂ which are typical representatives in the family of boron-rich compounds. The low energy limit increases with the atomic number of the foreign atoms rising while the upper energy limit remains constant (215eV). Ico-XANES spectra show correlation between XANES and either bond length, crystal structure, or defects.

In this work, a MAX phase material becomes a good candidate to study XANES spectrum since same type of phase has same crystal structure but different elements, and different phases consist of same type of elements but different crystal structures. XANES spectra of MAX phase materials [phase (211) and (312)] show correlations between XANES and either the element type, the 1st and 2nd nearest neighbors, or the crystal structure.

APPROVAL PAGE

The faculty listed below, appointed by the Dean of the School of Graduate Studies have examined a dissertation titled “*ab initio* Computational Applications of Electronic Structure and Spectroscopic Properties of Bulk Crystalline Materials,” presented by Liaoyuan Wang, candidate for the Doctor of Philosophy degree, and certify that in their opinion it is worthy of acceptance.

Supervisory Committee

Wai-Yim Ching, Ph.D., Committee Chair

Department of Physics & Astronomy

Michael Kruger, Ph.D.

Department of Physics & Astronomy

Anthony Caruso, Ph.D.

Department of Physics & Astronomy

Nathan A. Oyler, Ph.D.

Department of Chemistry

Zhonghua Peng, Ph.D.

Department of Chemistry

CONTENTS

ABSTRACT	iii
LIST OF ILLUSTRATIONS	ix
LIST OF TABLES	xiii
ACKNOWLEDGEMENTS	xiv
Chapter	
1 INTRODUCTION	1
1.1 Context	1
1.2 Motivation and Outline	5
2 THEORETICAL METHODS	6
2.1 Density Functional Theory	7
2.1.1 Introduction	7
2.1.2 The Basics of Density Functional Theory: The Hohenberg-Kohn Theorems	8
2.1.3 Kohn-Sham Equation	10
2.1.4 Exchange correlation Functional	14
2.2 Orthogonalized linear combination of atomic orbitals (OLCAO) method	16
2.2.1 Introduction	16
2.2.2 The Atomic Basis Functions	17
2.2.3 The Site-Decomposed Potential Function	18
2.2.4 Secular Equations	19
2.2.5 Electron Density Representation	20
2.3 Electronic Structure and Spectroscopic Properties Calculation	22
3 ELECTRONIC STRUCTURE AND SPECTROSCOPIC PROPERTIES OF ELEMENTAL BORON	26
3.1 Introduction	26

3.1.1 History	26
3.1.2 Difficulty and Challenge	27
3.1.3 Crystal Structure of Elemental Boron	29
3.1.4 Distortion of Icosahedron In Elemental Boron	34
3.1.5 Three-Center Two-Electron Bonds	39
3.2 Electronic Structure	40
3.3 XANES Spectra	49
3.3.1 XANES Spectra of α -r-B ₁₂ and β -r-boron	49
3.3.2 XANES Spectrum of an Isolated Boron Icosahedron and Elemental Boron Phases	50
3.4 Valence Band Optical Properties	55
3.5 Conclusion	58
4 ELECTRONIC STRUCTURE AND SPECTROSCOPIC PROPERTIES OF BORON-RICH COMPOUNDS	60
4.1 Introduction	60
4.2 Crystal Structure and Structure Modeling	62
4.3 Electronic Structure and Optical Properties	67
4.4 XANES/ELNES Spectra	75
4.4.1 XANES Spectra of α -r-B ₁₂ , B ₁₁ C-CBC, and B ₁₂ O ₂	75
4.4.2 Comparison of XANES Spectra for Elemental Boron and B ₁₁ C-CBC and B ₁₂ O ₂	83
4.5 Conclusions	85
5 ELECTRONIC STRUCTURE AND SPECTROSCOPIC PROPERTIES OF MAX PHASE MATERIALS	88
5.1 Introduction	88
5.2 Results on XANES/ELNES spectra	90

5.2.1 Electronic Structures of Ti_2AlC , Ti_2AlN , Cr_2AlC , Nb_2AlC , and Ti_3AlC_2	90
5.2.2 Comparison with Experiment on the K-edges in Ti_2AlC , Ti_2AlN , and Nb_2AlC Crystals	92
5.2.3 Calculated Edge Spectra in Cr_2AlC and Ti_3AlC_2	97
5.2.4 Results on Al-K and Al-L ₃ Edges in All Five MAX phases	99
5.2.5 Relation to the Electronic Structure of the MAX Phases for Excited State	103
5.2.6 Anisotropy in the XANES/ELNES Spectra	106
5.3 Conclusion	111
6 SUMMARY AND FUTURE WORK	112
6.1 Overview	112
6.2 Prospects of Future Work	115
REFERENCES	116
VITA	129

ILLUSTRATIONS

Figure	Page
1 Schematic view of the relationship between analytical theory, experiment, and computer simulation ⁴	2
2 The phase diagram of elemental boron.....	28
3 Crystal structures of (a) α -r-B ₁₂ , (b) γ -B ₂₈ , (c) α -t-B ₅₁ , (d) β -r-B ₁₀₆ , (e) β -t-B ₁₉₀ , and (f) α -Ga type boron. In ordered systems (α -r-B ₁₂ , γ -B ₂₈ , and α -Ga type boron), different colors represent the different nonequivalent sites. In disordered systems (α -t-B ₅₁ , β -r-B ₁₀₆ , and β -t-B ₁₉₀), different colors represent geometrical clusters, such as isolated icosahedron, icosahedral cluster, and individual isolated site. The specific sites in β -r-B ₁₀₆ , such as B9 and B10, are colored magenta although they belong to clusters T2 and T1, respectively.	29
4 Radial pair distribution function of crystalline elemental boron	34
5 Scheme for the variance of bond angles with (a) terminations of an angle moving on the sphere, (b) vertex moving outside/inside the sphere, and (c) terminations of an angle moving outside/inside the sphere.	36
6 (a) Bond angle distribution and (b) RPDFs for α -r-B ₁₂	37
7 (a) Bond angle distribution of intra-icosahedron and (b) RPDFs for γ -B ₂₈	38
8 Polar sites and equatorial sites in α -r-B ₁₂	40
9 Calculated band structures of (a) α -r-B ₁₂ , (b) γ -B ₂₈ , (c) α -t-B ₅₁ , (d) β -r-B ₁₀₆ , (e) β -t-B ₁₉₀ , and (f) α -Ga type boron.....	43
10 Calculated TDOS of α -r-B ₁₂ , γ -B ₂₈ , α -t-B ₅₁ , β -r-B ₁₀₆ , β -t-B ₁₉₀ , and α -Ga type boron (The vertical red line denotes the Fermi level).	44
11 Calculated PDOS of (a) the icosahedron and (b) the boron pair in γ -B ₂₈	45
12 Calculated PDOS of (a) the icosahedron and (b) the isolated boron atoms in α -t-B ₅₁	45
13(a) TDOS and Ico-PDOS of β -r-B ₁₀₆ ; (“TOTAL Edge” represents the sum of density of states of icosahedra along edges A, B and C; “Edges A”, “Edges B”, and “Edges C” represent the DOS of each single icosahedron along the edges; “Corner” represents the DOS of the icosahedron at the lattice corner; “T1” and “T2” represent grouped PDOS for icosahedral clusters); (b)TDOS and PDOS of special sites in β -r-B ₁₀₆ (“B1”, “B2”, “B8”, “B9”, and “B10” represent specific sites in β -r-B ₁₀₆).	46

14 Ico-PDOS of isolated icosahedron (I1 to I8), icosahedral cluster (C1 to C4), and isolated sites (S1 - S10, group in two each) in β -t-B ₁₉₀ . The atom-resolved PDOS of sites S1 and S2 (also S3 and S4, S5 and S6, etc.) are the same and are put together.	48
15 Experimental and calculated XANES spectra of (a) α -r-B ₁₂ ^{102,103} and (b) β -r-Boron ¹⁰²	50
16 (a) XANES spectra of perfect icosahedron models with different bond lengths; (b) Energy shifts of peak locations with the changes of the bond lengths.	51
17 XANES spectra of the perfect icosahedron model (B ₁₂), α -r-B ₁₂ , γ -B ₂₈ , α -t-B ₅₁ , β -r-B ₁₀₆ , β -t-B ₁₉₀ , and α -Ga type boron.....	53
18 XANES spectra of icosahedral clusters in α -r-B ₁₂ , α -t-B ₅₁ , γ -B ₂₈ , β -r-B ₁₀₆ , and β -t-B ₁₉₀	54
19 Experimental ¹⁰² (red) and calculated (black) dielectric functions (ϵ_1 , ϵ_2) for α -r-B ₁₂ (a, b) and β -r-boron(c, d).....	55
20 Calculated real (ϵ_1 black) and imaginary (ϵ_2 red) component of the complex dielectric functions of (a) semiconductors (α -r-B ₁₂ , γ -B ₂₈ , and β -r-B ₁₀₆) and (b) metals (α -t-B ₅₁ , β -t-B ₁₉₀ , and α -Ga type boron).....	57
21 (a) Scheme for polar and equatorial site in α -r-B ₁₂ ; crystal structure of (b) α -r-B ₁₂ , (c) B ₁₁ C-CBC, (d) B ₁₂ O ₂	64
22 Calculated band structures of: (a) α -r-B ₁₂ , (b) B ₄ C, and (c) B ₁₂ O ₂ (The red line denotes the Fermi level).....	68
23 Calculated total DOS and PDOS of α -r-B ₁₂ . (a) Total; (b) B _{polar} ; (c) B _{equat}	69
24 Calculated total DOS and PDOS of B ₁₂ O ₂ . (a) Total; (b) B _{polar} ; (c) B _{equat} ; (d) O.	69
25 Calculated total DOS and PDOS of B ₄ C. (a) Total; (b) B _{polar} ; (c) B _{equat} ; (d) B in the chain; (e) C in the center of the chain; (f) C in the icosahedron at the polar site.	70
26 Calculated directionally averaged real and imaginary of the optical dielectric function of: (a) α -r-B ₁₂ , (b) B ₄ C, and (c) B ₁₂ O ₂	73
27 Comparison of the axial and planar components of the imaginary part of the optical dielectric function in: (a) α -r-B ₁₂ , (b) B ₄ C, and (c) B ₁₂ O ₂	74
28 Calculated B-K edge in α -B ₁₂ . Top panel is total weighted sum of individual spectra from polar and equatorial B atoms (lower panels).....	76

29	Calculated (a) B-K edge and (b) C-K edge in B ₁₁ C-CBC. For both figures, the top two panels individually show total K-edge, the rest panels show the K-edge for different sites.....	77
30	Comparison between the calculated and the measured ELNES spectra in B ₄ C: (a) B-K; The calculated spectrum is shifted by 4.47 eV to align the main peak with experiment ¹⁰⁸ ; (b) C-K. The calculated spectrum is shifted by 4.50 eV to align the main peak with experiment (ref. ¹⁰⁹ , top, ¹¹⁰ , middle.).....	79
31	Calculated B-K edge in B ₁₂ O ₂ . Top panel is the weighted sum and the lower panels are the spectra from polar and equatorial B sites.....	80
32	Comparison of the calculated (total) and the measured B-K edge (a), and O-K edge (b). The calculated spectrum is shifted by 3.94 eV for B-K and 5.69 eV for O-K to align the main peaks with experiment.	81
33	Comparison of the calculated B-K spectra (total) of (a) α -r-B ₁₂ , (b) B ₄ C, and (c) B ₁₂ O ₂	83
34	Calculated XANES spectra of B-K of B ₁₁ C-CBC and α -r-B ₁₂	85
35	Crystal structure of (a) (211) phase, (b) (312) phase.....	90
36	Band structures of (a) Ti ₂ AlC, (b) Ti ₂ AlN, (c) Cr ₂ AlC, (d) Nb ₂ AlC, (e) Ti ₃ AlC ₂ (red line denotes Fermi level).	91
37	Band structures of (a) Ti ₂ AlC, (b) Ti ₂ AlN, (c) Cr ₂ AlC, (d) Nb ₂ AlC, (e) Ti ₃ AlC ₂ (red line denotes Fermi level).	92
38	Comparison of experimental (from ref. xx) and calculated XANES spectra: (a) Ti-K of Ti ₂ AlC, (b) C-K of Ti ₂ AlC; (c) Ti-K of Ti ₂ AlN, (d) N-K of Ti ₂ AlN; (e) Nb-K of Nb ₂ AlC.	95
39	Calculated (y-axis) vs. experimental (x-axis) values of spectral features of: (a) Ti-K in Ti ₂ AlC, (b) C-K in Ti ₂ AlC, (c) Ti-K in Ti ₂ AlN and (d) N-K in Ti ₂ AlN	96
40	Calculated spectra of (a) Cr-K in Cr ₂ AlC compared with (b) Nb-K in Nb ₂ AlC, and (c) C-K in Cr ₂ AlC and (d) C-K in Nb ₂ AlC.....	98
41	Comparison of calculated Ti-K in (a) Ti ₂ AlC and (b) Ti ₃ AlC ₂ , and C-K in (c) Ti ₂ AlC and (d) Ti ₃ AlC ₂	99
42	Calculated Al-K edges in Ti ₂ AlC, Ti ₂ AlN, Ti ₃ AlC ₂ , Cr ₂ AlC and Nb ₂ AlC	101
43	Calculated Al-L ₃ edges in Ti ₂ AlC, Ti ₂ AlN, Ti ₃ AlC ₂ , Cr ₂ AlC and Nb ₂ AlC.	102

44	Top panel: Calculated M-K edges in Ti_2AlC , Ti_2AlN , Ti_3AlC_2 , Cr_2AlC , and Nb_2AlC . Lower panel, the excited calculated total PDOS for the p-components in the CB and their contribution from each type of elements M, Al, X.....	105
45	Directionally resolved XANES spectra of (a) Ti-K in Ti_2AlC , Ti_2AlN , Ti_3AlC_2 ; (b) Cr-K in Cr_2AlC ; (c) Nb-K in Nb_2AlC (blue solid line denotes x-y plane; red dot line denotes z-direction).....	108
46	Directionally resolved XANES spectra of (a) Al-K and (b) Al-L ₃ in Ti_2AlC , Ti_2AlN , Ti_3AlC_2 , Cr_2AlC and Nb_2AlC (blue solid line denotes x-y plane; red dot line denotes z-direction).....	109
47	Directionally resolved XANES spectra of (a) C-K in Ti_2AlC , Cr_2AlC , Nb_2AlC , Ti_3AlC_2 ; (b) N-K in Ti_2AlN (blue solid line denotes x-y plane; red dot line denotes z-direction).....	110

TABLES

Table	Page
1 Cell parameters and space group symmetries for the six crystalline elemental boron phases.....	33
2 Measured and calculated band gaps (eV) of α -r-B ₁₂ , γ -B ₂₈ , and β -r-B ₁₀₆	44
3 Relaxation summary of five different configurations of boron carbide B ₄ C.....	66
4 Crystals structure parameters of α -r-B ₁₂ , B ₄ C, and B ₁₂ O ₂ . Bond lengths are in Å.	66
5 Shift in energy to align the main peak in the calculated spectra with experiment.....	94
6 Distances (Å) between M and the 1 st (2 nd) nearest neighbors in the five MAX phases.....	104

ACKNOWLEDGEMENTS

The lyric of a Chinese song says “...no myself alive without your taking care...” It is true: No my achievement without your aid!

I would like to express my gratitude to my advisor, Dr. Wai-Yim Ching, for his excellent guidance, severe criticism but selfless aid, continuous support throughout this work. I am also impressed by his diligence, wisdom, intelligence and time management.

I am grateful to Dr. Anthony Caruso and Dr. Michael Kruger of the Department of Physics and Astronomy, Dr. Zhonghua Peng and Dr. Nathan Oyler of the Chemistry Department for their valuable discussion, insightful comments and suggestion in my research and kindly serving in my supervisory committee.

I sincerely appreciate my parents, Mr. Guoxiang Wang and Mrs. Jinhua Wang. Without their persistent supports, there is not my achievement. Also, I want to express my gratitude to my fiancée, Bo Zhang, who provides me much encouragement in spirit and care in life.

Specially, I express my gratitude to my American family, William Beard and Mary Beard. They help me to improve my English, learn American culture, and offer me free dorm. Without their aid, I cannot focus on my research.

While involved with the electronic structure group at UMKC, the group members, especially Dr. Paul Rulis, are the vital source of assistance and support. For that I am very grateful. I also sincerely appreciate my friends, especially Mr. Naseer Dari, Mr. Yuxiang Mo, and Mr. Marcus Driver, who discussed with me in research and helped me a lot during pursuit of my Ph.D. degree.

Finally, I would like to thank the University of Missouri-Kansas City, the Department of physics and astronomy at UMKC, and the US Department of Energy for their monetary and resource support through scholarship, travel grants, and training courses.

For my family and those people who helped me

CHAPTER 1

INTRODUCTION

1.1 Context

Human history is also a history about the development of new materials and new techniques (synthesis and measurements). The emergence of new materials always accompanies a breakthrough on new techniques. Conversely, new materials spur research progress on new techniques. A huge amount of new materials have been synthesized and studied, and new techniques have made great progress. Nevertheless, research on materials is often limited by the current experimental techniques.

The structure of a material, as is well known, determines its physical and chemical properties. However, the structure of the material, especially for nano material, amorphous material, complicated compound or solid material, is very hard to determine due to those challenges originating from the nature of the materials and the methods of synthesis, measurements, and applications. For an instance, crystalline elemental boron, an electron-deficient material, is usually synthesized under high temperature^{1,2} (over 1000 °C), and under high pressure^{1,23} (\geq GPa), so that the impurities and structural defects (such as vacancy, self-interstitial atoms, substitution impurity atoms, interstitial impurity atoms) cannot be avoided under such extreme conditions. The electron deficient property determines that the solid boron needs interstitial atom or foreign atom to compensate for the deficiency but how to arrange these defects is still unclear. And the complicated cluster (icosahedron or icosahedral clusters) in most solid phases makes the research more difficult. Traditional x-ray diffraction (XRD) techniques cannot determine the structures without the aid of other techniques, such as nuclear magnetic resonance (NMR), extended x-ray

absorption fine structure (EXAFS), x-ray absorption near structure (XANES), and electron energy loss near edge structure (ELNES). Even so, many structures have not yet been confirmed since these techniques do not show the structures directly, instead the properties which are related to the structures. To figure out the structure, different models need to be built up or modified and then the computer simulation is repeatedly used to verify whether the calculated properties based on these models agree with experimental results. These iterations are continued until a right model is found.

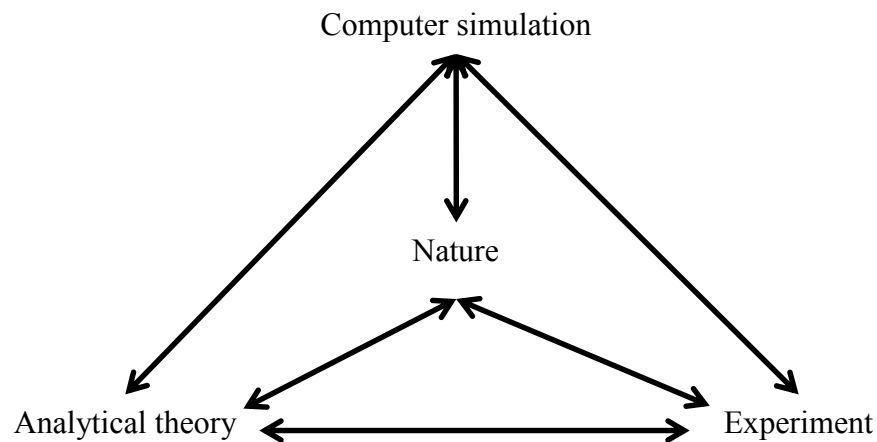


Fig. 1 Schematic view of the relationship between analytical theory, experiment, and computer simulation⁴

The above example has presented the relation between experiment and computer simulation. In fact, computer simulation is based on both analytical theory and modern computer techniques. Fig. 1⁴ shows the relationship between analytical theory, experiment, and computer simulation with each other. The traditional method to understand the phenomenon of nature is to compare the experimental result with theoretical concept. However, the limitation of computational capabilities, at that moment, resulted in inadequate models, an inaccurate approximation, over simplification, or all of the above which led to discrepancies between output of an analytical theory and experimental results.

With the development of computer techniques, computational simulation including computational physics, computational chemistry, etc. gradually fixed these problems and has become an important and irreplaceable complementary technique and tool.

Computational simulation is essentially to solve equations using numerical method. In material fields, it consists of two parts (steps): to solve equations using numerical methods and to calculate physical and chemical properties using different theories. The solution for those equation(s) is an evaluation of certain operations $f(x)$ if these operations $f(x)$ can be formulated. Using numeric methods, the solutions are expressed in a set of discrete points and usually need to be approximated by certain numerical method. Based on the solutions (basis) and associated with a certain theory, these solutions are used to simulate physical and chemical properties. Applied in different fields, computational science derives different branches, such as computational physics, computational chemistry. The research within this dissertation is part of computational physics.

Computational simulation has its specific advantages compared to experimental science. First, not all experiments can be performed or tracked. Computational simulation can simulate a process or status which may not be easy to perform (such as nuclei replacement experiments) or track (such as the transition process for a spectrum) in experiments. Second, the computer simulations can also provide more insight and detailed understanding. For example, the measured x-ray absorption near edge structure (XANES) spectrum only records the electron absorption coefficient which does not include any information on the electron-transition process. To understand the spectrum, the electron transition for XANES can be simulated as the change between initial states and final states (refer chapter 2). Third, computational simulation can predict some properties of a material

that might have not been measured due to the limitation of experimental techniques or some other reasons. If simulations based on those known experimental measured structures are consistent with the measured properties, the simulations based on theoretical models (unknown or improved according to the experiment measurements) could help to understand correlations between properties and theoretical models. Usually, the structure of a material is related to those synthetic conditions, such as pressure, temperature, electric and/or magnetic fields. Thus, experiments can be further conducted forward to the predicted direction controlling certain synthetic conditions. Finally, the cost in computations is relatively much lower than that of experiments.

Everything has two sides, so does computational simulation. First of all, not all phenomena can be formulated and accurately digitalized. Even though some phenomena can be formulated, there is not a solution for the equations or it will cost forever to get the solution based on the current computational power. Second, any approximations applied in the calculation have their premises and may lead to a wrong result even though the premise can be satisfied. Thus, the calculated results have to be verified by the experimental measurements. If the calculation disagrees with the experimental results, each step including the theoretical model, approximation, computational method and so on, have to be checked to find what reason caused the errors, and then the calculation has to be performed and tested again. Sometimes, the iteration may cost more time, money, and human resources, so the cost is not economic. Although there exist these limitations, computational simulation has made great progress and has been playing a more and more important and irreplaceable role.

1.2 Motivation and Outline

This work presented within this dissertation will focus on the electronic structure and spectroscopic properties [XANES spectrum, and optical property] based on *ab initio* density functional theory (DFT). These properties for crystalline elemental boron, boron-rich compounds, and MAX phase materials are calculated and studied using orthogonalized linear combination atomic orbitals (OLCAO) method. The research on XANES spectra of boron icosahedral models can help to investigate the characteristic features of boron icosahedral clusters. The correlations between XANES spectra and bond length (or/and bond angle) can be understood based on these boron icosahedral models. Furthermore, the XANES spectra of crystalline elemental boron and boron-rich compounds can be interpreted based on the understanding of boron icosahedral models. On property side, electronic structure is employed to interpret the XANES and optical properties although this interpretation is a little rough. On material side, the study of the XANES spectrum of MAX help to individually understand the correlations between XANES spectra and element types, crystalline structures.

In this dissertation, associated with the calculation of electronic structure and spectroscopic properties, the methods of calculation are described in chapter 2. Chapters 3-5 involve case studies which include the electronic structure and spectroscopic properties of elemental boron (chapter 3), boron-rich compounds (chapter 4) and MAX phase materials (chapter 5). Chapter 6 shows the summary of the work and problems, and then shows the perspective for the future work.

CHAPTER 2

THEORETICAL METHODS

Most true systems are many-electron systems which comprise single atoms, the most elementary building blocks of ordinary matter, all kinds of molecules, ranging from dimers to proteins, as well as mesoscopic systems. Generally, all these systems are studied in two types of states: ground state and excited state⁵. For research on the ground state, the most interesting and important property is the structural property which is related to the shell structure and electric/magnetic moments. The ground state determines the stability (usually discussed in bond energy determined by electronic nature or bonds between atoms) of a system and other properties (electrical conductivity, thermal conductivity, etc.). For research on the excited state, the electronic excitation spectra are the most notable dynamical spectroscopic properties, including optical properties, and XANES, which show excitation energy of optical properties and the scattering processes⁵.

There are two basic approaches to study these properties⁵. One is an approach using a model Hamiltonian and the other one is *ab initio* (1st principles) approach. The prior one uses the isolatable available information (usually experimental) on a system to construct a model Hamiltonian. This makes model Hamiltonian simpler than the other method (*ab initio* method). However, the model Hamiltonian method becomes very sensitive to inputs since it needs to adjust the parameters to match the experimental or some *ab initio* results. In this dissertation, only the *ab initio* method will be discussed. In section 2.1, density functional theory (DFT) will be briefly reviewed. Based on DFT and a couple of important approximations, the OLCAO method will be shortly shown in section 2.2. VASP is only

used for relaxation and will not be introduced here. And the last section will show how to calculate electronic structure and spectroscopic properties.

2.1 Density Functional Theory

2.1.1 Introduction

Ab initio methods consist of solving Schrödinger equation and then simulating the physical or chemical properties based on the prior calculated solutions. To be general, we are considering a collection of an arbitrary number of electrons which are enclosed in a large box and moving under the influence of an external potential $V_{ext}(r)$ and the mutual Coulomb repulsion. The Hamiltonian has the form

$$H = T + V + U \quad 2-1$$

where

$$T = \frac{1}{2} \langle \psi | \nabla^2 | \psi \rangle = \frac{1}{2} \langle \nabla \psi | \nabla \psi \rangle \equiv \frac{1}{2} \int \nabla \psi^*(\vec{r}) \nabla \psi(\vec{r}) d\vec{r} \quad 2-2$$

$$V \equiv \int V_{ext}(\vec{r}) \psi^*(\vec{r}) \psi(\vec{r}) d\vec{r} \quad 2-3$$

$$U = \frac{1}{2} \int \frac{1}{|\vec{r}-\vec{r}'|} \psi^*(\vec{r}) \psi^*(\vec{r}') \psi(\vec{r}) \psi(\vec{r}') d\vec{r} d\vec{r}' \quad 2-4$$

Here, atomic units are used. Based on time independent (stationary state) Schrödinger equation, $H \psi = E \psi$. Here, ψ denote the ground states which are nondegenerate. The electronic density in the ground state ψ can be presented by

$$\rho(\vec{r}) \equiv (\psi, \psi^*(\vec{r}) \psi(\vec{r}) \psi) \quad 2-5$$

which is clearly a functional of $V_{ext}(\vec{r})$. All above statements are not in terms of functional theory, instead they are written as basic quantum concepts. Hohenberg and Kohn⁶ proved

that $\rho(\vec{r})$ is a functional of $V_{ext}(\vec{r})$ in 1964. Since then, the density functional theory (DFT) grew rapidly and became a fully-fledged theory.

2.1.2 The Basics of Density Functional Theory: The Hohenberg-Kohn Theorems

DFT is a quantum mechanical modeling method used in physics and chemistry to investigate the electronic structure (principally the ground state) of many-body systems, in particular atoms, molecules, and the condensed phases⁵. The Thomas-Fermi theory⁶ about electron gas is the earliest literature on DFT which can be tracked, however, it was not until the Hohenberg-Kohn (HK)⁶ theorems were proposed in 1964 that DFT was put on a firm theoretical footing. The HK theorems⁶ state

(1) The electron density $\rho(\vec{r})$ in the ground state is a functional of the external potential $V_{external}(\vec{r})$ [denoted as $V_{ext}(\vec{r})$];

(2) The external potential $V_{ext}(r)$ is a unique functional of density $\rho(\vec{r})$.

Hohenberg and Kohn define a universal functional

$$F[\rho(\vec{r})] \equiv (\psi, (T+U)\psi) \quad 2-6$$

where ψ is ground state. Obviously, the external potential in the Hamiltonian is essentially separated from kinetic and inner potential. This universal functional is valid for any number of particles and any external potential. With its aid, for a given potential $V_{ext}(r)$, the energy functional

$$E_V[\rho] \equiv \int V_{ext}(\vec{r})\rho(\vec{r})d\vec{r} + F[n] \quad 2-7$$

can be proven that the minimal value of $E_V[\rho]$, for the correct $\rho(\vec{r})$, is the ground-state energy E if the condition

$$N[\rho] \equiv \int \rho(\vec{r})d\vec{r} = N \quad 2-8$$

can be satisfied.

Hohenberg and Kohn separate out the classical Coulomb energy from $F[\rho(r)]$ since the Coulomb interaction is a long range interaction. $F[\rho]$ can be written

$$F[\rho] = \frac{1}{2} \int \frac{\rho(\vec{r})\rho(\vec{r}')}{|\vec{r}-\vec{r}'|} d\vec{r}d\vec{r}' + G[\rho] \quad 2-9$$

So that $E_V[\rho]$ becomes

$$E_V[\rho] = \int V_{ext}(\vec{r})\rho(\vec{r})d\vec{r} + \frac{1}{2} \int \frac{\rho(\vec{r})\rho(\vec{r}')}{|\vec{r}-\vec{r}'|} d\vec{r}d\vec{r}' + G[\rho] \quad 2-10$$

where $G[\rho]$ is a universal functional like $F[\rho]$. According to the definition of $F[\rho]$, Eq. 2.6 and $G[\rho]$, Eq. 2.8, we can get

$$G[\rho] = \frac{1}{2} \int \nabla_r \nabla_{r'} \rho_1(\vec{r}, \vec{r}')|_{r=r'} d\vec{r} + \frac{1}{2} \int \frac{C_2(\vec{r}, \vec{r}')}{|\vec{r}-\vec{r}'|} d\vec{r}d\vec{r}' \quad 2-11$$

where $\rho(\vec{r}, \vec{r}')$ is the one-particle density matrix; and $C_2(\vec{r}, \vec{r}')$ is the two-particle correlation function defined in terms of the one- and two-particle density matrices as

$$C_2(\vec{r}, \vec{r}') = \rho_2(\vec{r}, \vec{r}'; \vec{r}, \vec{r}') - \rho_1(\vec{r}, \vec{r}')\rho_1(\vec{r}, \vec{r}') \quad 2-12$$

Therefore,

$$G(\rho) = \int g_r[\rho]d\vec{r} \quad 2-13$$

Here,

$$g_r[\rho] = \frac{1}{2} \nabla_r \nabla_{r'} \rho_1(\vec{r}, \vec{r}')|_{r=r'} + \frac{1}{2} \int \frac{C_2(\vec{r}-\frac{\vec{r}'}{2}; \vec{r}+\frac{\vec{r}'}{2})}{|\vec{r}-\vec{r}'|} d\vec{r}' \quad 2-14$$

Remarkably, $G[\rho]$ is a unique functional, however, $g_r[\rho]$ may have multiple forms.

Obviously, Hohenberg and Kohn have shown the $\rho(\vec{r})$ is the functional of kinetic energy, external potential, and number of particles in a system. However, the energy function was left unspecified. Therefore, it is impossible to solve the Schrödinger equation

without determining a Hamiltonian. To accurately express the kinetic energy and exchange-correlation energy functional, Kohn and Sham introduced a concept of non-interacting reference system which shares the same density with the real interacting system.

2.1.3 Kohn-Sham Equation

Any research approach always starts from a simple model, and then this approach is modified or improved into a more complicate model or system. The essential idea for Hohenberg, Kohn and Sham is to utilize the results from homogeneous gas in theoretical research of inhomogeneous systems. If the contribution from Hohenberg and Kohn is to separate external potential from the kinetic energy and inner potential, and prove that the $\rho(\mathbf{r})$ is the functional of external potential and kinetic energy, then the dominant work from Kohn and Sham is to introduce the orbitals into the formalism of HK theory and separate the Hamiltonian into non-interacting and interacting parts. The results from ideal non-interacting can be inherited and the interacting effects are put in exchange parts. They also find a way to obtain a set of self-consistent equations which include the exchange and correlation effects in an approximate way. The following shows their essential thought and equations.

Kohn and Sham assume the density of a system studied is slowly varying or it is very high. From HK theory, the total energy functional is eq. 2-15,

$$E_V[\rho] = \int V_{EXT}(\vec{r})\rho(\vec{r})d\vec{r} + \frac{1}{2} \iint \frac{\rho(\vec{r})\rho(\vec{r}')}{|\vec{r}-\vec{r}'|} d\vec{r}d\vec{r}' + G[\rho] \quad 2-10$$

Here, Kohn and Sham define

$$G[\rho] \equiv T_s[\rho] + E_{XC}[\rho] \quad 2-15$$

where $T_s[\rho]$ is the kinetic energy of a system of non-interacting electrons with density $\rho(\mathbf{r})$ and $E_{xc}[\rho]$ is the exchange and correlation energy of an interacting system with density $\rho(\mathbf{r})$.

For an arbitrary $\rho(\mathbf{r})$ which is sufficiently slowly varying, one can show⁶ that

$$E_{xc}[\rho] = \int \rho(\vec{r}) \epsilon_{xc}[\rho(\vec{r})] d\vec{r} \quad 2-16$$

For an N-electron system, Eq. 2.10 can be written as

$$\begin{aligned} E(\rho) &= T_s[\rho] + J[\rho] + E_{xc}[\rho] + \int \rho V_{ext} d\vec{r} \\ &= \sum_i^N \sum_s \int \psi_i^* \left(-\frac{1}{2} \nabla^2\right) \psi_i d\vec{r} + J[\rho] + E_{xc}[\rho] + \int \rho V_{ext} d\vec{r} \end{aligned} \quad 2-17$$

where $J[\rho]$ is the classical Coulomb potential.

For a non-interacting system, Hamiltonian can be written as $H=T + V$, in which there are no electron-electron repulsion terms, and for which the ground state electron density is exactly ρ . For this non-interacting system, the determinant ground state wave function is

$$\Psi_i = \det\{\psi_1, \psi_2, \dots, \psi_N\} / \sqrt{N!} \quad 2-18$$

where ψ_i are the N ground eigenstates of the one-electron Hamiltonian \hat{h}_i :

$$\hat{h}_i \psi_i = \epsilon_i \psi_i \quad 2-19$$

the electron density can be decomposed as

$$\rho = \sum_i^N \sum_s \int |\psi_i(\vec{r}, s)|^2 \quad 2-20$$

If the N orbitals are continuous and square integrable, then the density defined in (2.19) covers the N-representable ensemble. So the variational search for the minimum can be equivalent in orbital space $\{\psi_i\}$. In order to have the electron density defined in (2.2) be valid, the N orbitals must actually be orthonormal,

$$\int \psi_i^*(x)\psi_j(x)dx = \delta_{ij} \quad 2-21$$

In the variational search formula, the ground-state total energy can be written as

$$E_g = \min_{\int \psi_i^*(x)\psi_j(x)dx=\delta_{ij}} \left\{ \sum_i^N \sum_s \int \psi_i^* \left(-\frac{1}{2} \nabla^2\right) \psi_i d\vec{r} + J[\rho] + E_{xc}[\rho] + \int \rho V_{ext} d\vec{r} \right\} \quad 2-22$$

with the Lagrange Multiplier method, the condition for minimum $E[\rho]$ is

$$\delta \left\{ E[\rho] - \sum_i^N \sum_j^N \varepsilon_{ij} \int \psi_i^*(x)\psi_j(x)dx \right\} = 0 \quad 2-23$$

Here, ε_{ij} is a Hermitian matrix which can be diagonalized by a unitary transformation of the orbitals. Such a transformation leaves the density and the Hamiltonian invariant. Eq. 2.22 leads to the equations

$$\hat{H}\psi_i = \left[-\frac{1}{2} \nabla^2 + v_{eff} \right] \psi_i = \sum_i^N \varepsilon_{ij} \psi_j \quad 2-24$$

where the effective potential is defined by

$$v_{eff} = v_{ext}(\vec{r}) + \frac{\delta J[\rho]}{\delta \rho} + \frac{\delta E_{xc}[\rho]}{\delta \rho} = v_{ext}(\vec{r}) + \int \frac{\rho(r')}{|r-r'|} d\vec{r}' + v_{xc}(\vec{r}) \quad 2-25$$

Thus, the famous Kohn-Sham orbital equations are obtained in the canonical form

$$\hat{H}\psi_i = \left[-\frac{1}{2} \nabla^2 + v_{eff} \right] \psi_i = \varepsilon_i \psi_i \quad 2-26$$

The total energy can be determined from the resultant density calculated via Eq.

2.21

$$E(\rho) = \sum_i^N \varepsilon_i - J[\rho] + E_{xc}[\rho] - \int \rho v_{xc} d\vec{r} \quad 2-27$$

Here,

$$\sum_i^N \varepsilon_i = \sum_i^N \left\langle \psi_i \left| -\frac{1}{2} \nabla^2 + v_{eff} \right| \psi_i \right\rangle = T_s[\rho] + 2J[\rho] + E_{xc}[\rho] + \int \rho V_{ext} d\vec{r} \quad 2-28$$

So far, the Kohn-Sham equation turns out to be exact for the ground state without any approximation.

Kohn and Sham⁷ also show that self-consistent equations should satisfy the following condition

$$\int \delta\rho(\vec{r})d\vec{r} = 0 \quad 2-29$$

when $\rho(\mathbf{r})$ is given. The equation

$$\int \delta\rho(\vec{r}) \left\{ \varphi(\vec{r}) + \frac{\delta T_s[\rho]}{\delta\rho(\vec{r})} + \mu_{xc}(\rho(\vec{r})) \right\} d\vec{r} = 0 \quad 2-30$$

Here,

$$\varphi(\vec{r}) = v(\vec{r}) + \int \frac{\rho(\vec{r}')}{|\vec{r}-\vec{r}'|} d\vec{r}' \quad 2-31$$

And

$$\mu_{xc}(\rho) = d(\rho\epsilon_{xc}(\rho))/d\rho \quad 2-32$$

For given φ and μ , one obtains the $\rho(\mathbf{r})$ which satisfies these equations simply by solving the one-particle Schrödinger equation

$$\left\{ -\frac{1}{2}\nabla^2 + [\varphi(\vec{r}) + \mu_{xc}(\rho(\vec{r}))] \right\} \psi_i = \epsilon_i \psi_i \quad 2-33$$

and setting

$$\rho(\vec{r}) = \sum_{i=1}^N |\psi_i(\vec{r})|^2 \quad 2-34$$

Eq. 2.31-2.34 have to be solved self-consistently: One begins with an assumed $\rho(\mathbf{r})$, constructs $\varphi(\mathbf{r})$ from Eq. 2.31 and μ_{xc} Eq. 2.32, and finds a new $\rho(\mathbf{r})$ from Eq. 2.33 and Eq. 2.34. The energy is given by

$$E = \sum_i^N \epsilon_i - \iint \frac{\rho(\vec{r})\rho(\vec{r}')}{|\vec{r}-\vec{r}'|} d\vec{r}d\vec{r}' + \int \rho(\vec{r})\{\epsilon_{xc}(\rho(\vec{r})) - \mu_{xc}(\rho(\vec{r}))\}d\vec{r} = 0$$

2-35

To solve the Kohn-Sham (KS) equation, the explicit expression of the many-body and non-classical exchange correlation (XC) functional term $E_{xc}[\rho]$ must be given. The local density approximation (LDA) is one of approximations to the exchange-correlation energy functional in DFT.

2.1.4 Exchange correlation Functional

To solve KS equation, it is necessary to explicitly express the exchange correlational functional. Nowadays the most frequently used approximations include LDA^{5,8} and generalized gradient approximation (GGA)⁵. Both have the similar forms

$$E_{XC}^{LDA}[\rho] = \int f_{LDA}(\rho(\vec{r}))d\vec{r} = \int \rho(\vec{r})\epsilon_{XC}(\rho(\vec{r}))d\vec{r} \quad 2-36$$

$$E_{XC}^{GGA}[\rho] = \int f_{GGA}(\rho(\vec{r}), g(\vec{r}))d\vec{r} = \int \rho(\vec{r})\epsilon_{XC}(\rho(\vec{r}), g(\vec{r}))d\vec{r} \quad 2-37$$

where $f = \rho(\vec{r})\epsilon_{XC}$ is the local XC energy density, and ϵ_{xc} is the XC energy per electron. The notations $\vec{g}(\vec{r}) \equiv \nabla\rho(\vec{r})$, $g_i(\vec{r}) \equiv \nabla_i\rho(\vec{r})$, and $g(r) \equiv |\nabla\rho(\vec{r})|$ are used where i labels the three Cartesian coordinates. In this work, we restrict the discussion to the spin non-polarized case for simplicity. The inclusion of spin polarized electron density is trivial. Assuming the limit of slow varying density, $f_{GGA}(\rho(\vec{r}), 0) = f_{LDA}(\rho(\vec{r}))$.

There are two different strategies to determine the function f_{GGA} . One is to adjust f such that it satisfies all (or most) known properties of the XC hole and energy, and the other one is to fit f to a large data set of exactly known binding energies of atoms and molecules. The former was preferred, when constructing GGA functionals, one usually

tries to incorporate a number of known properties of the exact functional into the restricted functional form of the approximation.

The XC potential has an explicit analytical form which can be derived from Eq.

2.32

$$v_{xc}^{LDA}(\rho) = \frac{d(\rho\epsilon_{xc}^{LDA}(\rho))}{d\rho} = \epsilon_{xc}^{LDA}(\rho) + \rho \frac{d(\epsilon_{xc}^{LDA}(\rho))}{d\rho} \quad 2-38$$

whereas for GGA it is considerably more complex⁹

$$\begin{aligned} v_{xc}^{GGA} &= \frac{\partial f_{GGA}}{\partial \rho} - \nabla \frac{\partial f_{GGA}}{\partial g} \\ &= \epsilon_{xc}^{GGA} + \frac{\partial \epsilon_{xc}^{GGA}}{\partial \rho} - g \frac{\partial \epsilon_{xc}^{GGA}}{\partial g} - \rho g \frac{\partial^2 \epsilon_{xc}^{GGA}}{\partial g \partial \rho} - \frac{\rho}{g} \frac{\partial \epsilon_{xc}^{GGA}}{\partial g} \nabla^2 \rho + \frac{\rho}{g^2} \frac{\partial \epsilon_{xc}^{GGA}}{\partial g} \vec{g} \nabla g - \\ &\frac{\rho}{g} \frac{\partial^2 \epsilon_{xc}^{GGA}}{\partial g^2} \vec{g} \nabla g \end{aligned} \quad 2-39$$

Obviously, v_{xc}^{GGA} depends on the 1st and 2nd gradient of the electron density.

2.2 Orthogonalized linear combination of atomic orbitals (OLCAO) method

2.2.1 Introduction

LCAO is one of those methods to solve Schrödinger equation of a many-electron systems. Originally, the concept of LCAO in band theory was introduced by Bloch in 1928^{10,11}. At that moment, many methods were intimately related to the LCAO concept. Later on, other related methods were developed primarily to solve or avoid certain practical difficulties associated with implementing LCAO¹². All these methods tried to balance the certain technical difficulties with desired accuracy and a greater range of applicability beyond monoatomic crystals. Meanwhile, the essence of each method was borrowed or absorbed by the other methods to improve desired accuracy or efficiency and achieve a broader application. For an instance, the essence of orthogonalized plane wave (OPW) method which is considered as the 1st method capable of a practical calculation of a crystal band structure was absorbed by LCAO method and then the LCAO method was developed into OLCAO method to improve the efficiency with acceptable accuracy.

OLCAO method, the improved LCAO method, originates from the concept of a linear combination of atomic orbitals (LCAO) which can be traced to the very beginning of the quantum theory of solids when the free electron model of metals was formulated. It is the direct extension of the LCAO method, but it inherits the essential idea of early LCAO and OPW¹².

OLCAO method consists of two phases: pre-phase and post-phase¹³. The prior one is to achieve the coefficient for each term of bases and potentials. And the latter one is to perform those physical properties, such as electronic structure, spectroscopic properties. In

this dissertation, the basic theory and techniques of the OLCAO method will be presented briefly.

2.2.2 The Atomic Basis Functions

The OLCAO method¹² is derived from the traditional LCAO method with the additional of numerous modifications and extensions. All the atomic orbitals are expressed in terms of Gaussian-type orbitals (GTOs) while the potential function is expressed as a sum of atom-centered Gaussian functions. This enables the rapid analytic evaluation of multi-center integrals^{12,14}. The solid state wave function $\psi_{nk}(\vec{r})$ is expanded in terms of Bloch sums $b_{i,\gamma}(\vec{k}, \vec{r})$:

$$\psi_{nk}(\vec{r}) = \sum_{i,\gamma} C_{i,\gamma}^n(\vec{k}) b_{i,\gamma}(\vec{k}, \vec{r}) \quad 2-40$$

where

$$b_{i,\gamma}(\vec{k}, \vec{r}) = \frac{1}{\sqrt{N}} \sum_{j=1}^N e^{-i\vec{k} \cdot \vec{R}_v} u_i(\vec{r} - \vec{R}_v - \vec{t}_\gamma) \quad 2-41$$

Here,

$$u_i(r) = \left[\sum_{j=1}^N A_j r^l e^{-\alpha_j r^2} \right] \cdot Y_l^m(\theta, \varphi) \quad 2-42$$

where γ labels the atoms in the cell and i represents the orbitals' quantum number l, m . α_j and A_j are predefined coefficient which vary from element to element. And the coefficients $\{C_j\}$ are obtained through separate atomic calculations. The radial part is represented by a linear combination of a suitable number of Cartesian GTOs and the angular part consists of the real spherical harmonics. More specifically, we have

s-type: $C_s r^{n-1} \exp(-\alpha r^2)$

p-type: $C_{p,x} r^{n-2} x \exp(-\alpha r^2)$, same for y, z

d-type: $C_{d,xy} r^{n-3} xy \exp(-\alpha r^2)$, same for $yz, zx, x^2-y^2, 2z^2-x^2-y^2$

f-type: $C_{f,xyz} r^{n-4} xyz \exp(-\alpha r^2)$, same for $z(x^2-y^2), x(x^2-3y^2), y(y^2-3x^2), z(5z^2-3r^2), x(5z^2-3r^2), y(5z^2-3r^2)$

2-43

The set of atomic orbitals u_i in Eq. 2.42 includes the core orbitals, the occupied valence orbitals, and a variable number of additional empty orbitals. To enhance the efficiency without sacrificing much accuracy, the atomic orbital basis can be organized into three types, EB (extended basis), FB (full basis) and MB (minimal basis). Each basis set definition is typically used for different purposes. The MB consists of core orbitals and the occupied valence orbitals only^{8,12}. The FB contains all core orbitals, all occupied valence shell orbitals, and one additional higher shell of orbitals. The EB extends the FB by adding one more higher shell of orbitals^{8,12}. For example, the FB of boron includes $1s, 2s, 2p, 3s, 3p$; the EB consists of $1s, 2s, 2p, 3s, 3p, 4s, 4p$ (here, $3d$ has not been included for its energy is much higher than $4s, 4p$ etc.); and the MB only includes $1s, 2s, 2p$.

2.2.3 The Site-Decomposed Potential Function

An important feature of the OLCAO method¹² is the real space description of the crystal's charge density $\rho_{cry}(\vec{r})$ and the one-electron crystal potential $V_{cry}(\vec{r})$ as sums of atom-centered functions consisting of Gaussians.

$$\rho_{cry}(\vec{r}) = \sum_A \rho_A(\vec{r} - \vec{t}_A), \rho_A(\vec{r}) = \sum_{j=1}^N B_j e^{-\beta_j r^2} \quad 2-44$$

Similarly, each part of the potential function (the electron-nuclear and electron-electron Coulomb interaction V_{Coul} and the exchange-correlation potential V_{XC}) can be expressed as atom-centered functions as follows

$$V_{Coul}(\vec{r}) = \sum_A V_C(\vec{r} - \vec{t}_A), V_C(\vec{r}) = -\frac{Z_A}{r} e^{-\xi r^2} - \sum_{j=1}^N D_j e^{-\beta_j r^2} \quad 2-45$$

$$V_{XC}(\vec{r}) = \sum_A V_x(\vec{r} - \vec{t}_A), V_A(\vec{r}) = \sum_{j=1}^N F_j e^{-\beta_j r^2} \quad 2-46$$

Then the crystal potential is written as the sum of atom-centered potentials:

$$V_{cry}(\vec{r}) = \sum_A V_A(\vec{r} - \vec{t}_A), V_A(\vec{r}) = V_C(\vec{r}) + V_x(\vec{r}) \quad 2-47$$

2.2.4 Secular Equations

By substituting the wave function with a linear combination of atomic orbitals, the standard solution of the KS equation (2.26) leads to the secular equation

$$|H_{i\gamma, j\delta}(\vec{k}) - S_{i\gamma, j\delta}(\vec{k})E(\vec{k})| = 0 \quad 2-48$$

where the first and the second terms are the Hamiltonian and Overlap matrices respectively:

$$H_{i\gamma, j\delta}(\vec{k}) = \langle b_{i\gamma}(\vec{k}, \vec{r}) | \hat{H} | b_{j\delta}(\vec{k}, \vec{r}) \rangle = \sum_{\mu} \exp(-i \vec{k} \cdot \vec{R}_{\mu}) \int \mu_{i\gamma}(\vec{r} - \vec{t}_{\gamma}) \left(-\frac{1}{2} \nabla^2 + v_{eff}\right) \mu_{j\delta}(\vec{r} - \vec{t}_{\gamma} - \vec{R}_{\mu}) \quad 2-49$$

$$S_{i\gamma, j\delta}(\vec{k}) = \langle b_{i\gamma}(\vec{k}, \vec{r}) | b_{j\delta}(\vec{k}, \vec{r}) \rangle \\ = \sum_{\mu} \exp(-i \vec{k} \cdot \vec{R}_{\mu}) \int \mu_{i\gamma}(\vec{r} - \vec{t}_{\gamma}) \mu_{j\delta}(\vec{r} - \vec{t}_{\gamma} - \vec{R}_{\mu})$$

In the case of s-type GTOs (n=0), the interaction integrals have the following forms:

Overlap integral

$$I_1 = \langle S_A | S_B \rangle = \int \exp(-\alpha_A r_A^2 - \alpha_B r_B^2) d\vec{r} \quad 2-50$$

Kinetic energy integral:

$$I_2 = \langle S_A | -\nabla^2 | S_B \rangle = \int \exp(-\alpha_A r_A^2) (-\nabla^2) \exp(-\alpha_B r_B^2) d\vec{r} \quad 2-51$$

Three center integral:

$$I_3 = \left\langle S_A \left| e^{-\alpha_C r_C^2} \right| S_B \right\rangle = \int \exp(-\alpha_A r_A^2) (e^{-\alpha_C r_C^2}) \exp(-\alpha_B r_B^2) d\vec{r}$$

2-52

Three center Coulomb integral

$$I_4 = \left\langle S_A \left| \frac{e^{-\alpha_C r_C^2}}{r} \right| S_B \right\rangle = \int \exp(-\alpha_A r_A^2) \left(\frac{e^{-\alpha_C r_C^2}}{r} \right) \exp(-\alpha_B r_B^2) d\vec{r} \quad 2-53$$

Momentum integral:

$$I_5 = \left\langle S_A \left| \frac{\partial}{\partial x}, \frac{\partial}{\partial y}, \frac{\partial}{\partial z} \right| S_B \right\rangle = \int \exp(-\alpha_A r_A^2) \left(\frac{\partial}{\partial x}, \frac{\partial}{\partial y}, \frac{\partial}{\partial z} \right) \exp(-\alpha_B r_B^2) d\vec{r} \quad 2-54$$

We can see that the use of Gaussians as the ultimate basis facilitates the analytical integral calculations. Regarding the higher angular momentum orbitals such as p -type, d -type, and f -type orbitals, their expressions are shown as recursive formula:

$$\begin{aligned} & \langle (x - A_x)^{i_A} (x - A_y)^{j_A} (x - A_z)^{k_A} \widehat{S}_A | \widehat{O} | (x - B_x)^{i_B} (x - B_y)^{j_B} (x - B_z)^{k_B} \widehat{S}_B \rangle = \\ & \frac{1}{2\alpha_B} \frac{\partial}{\partial B_z} \langle (x - A_x)^{i_A} (x - A_y)^{j_A} (x - A_z)^{k_A} \widehat{S}_A | \widehat{O} | (x - B_x)^{i_B} (x - B_y)^{j_B} (x - B_z)^{k_B} \widehat{S}_B \rangle \end{aligned}$$

2-55

2.2.5 Electron Density Representation

In section 2.1, the secular equations solved using the SCF method give us the KS orbitals $\psi_{nk}(\vec{k}, \vec{r})$, from which the electron density can be derived as follows

$$\rho^v(\vec{r}) = \int_{BZ} \sum_{occ} |\psi_{nk}(\vec{k}, \vec{r})|^2 d\vec{k} \quad 2-56$$

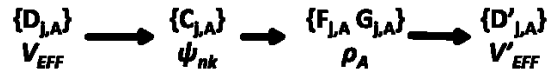
$\rho^v(\vec{r})$ represents the contribution of valence electron density whereas the core electron density $\rho^c(\vec{r})$ is obtained separately. Since the core states are highly localized and of little research interest in solids, even if the core states were orthogonalized, the accuracy would not be sacrificed, but the efficiency can be greatly improved. This is an important feature of the OLCAO method resulting from the core-orthogonalization process which performs a unitary transformation to the Hamiltonian and Overlap matrices to eliminate the non-diagonal blocks of the core states, and it has been proved extremely advantageous in complex systems. The details of core orthogonalization has been presented in Ouyang's work¹⁵ and Ching's publication¹². Here, for the detailed process will be skipped.

The core electron density and valence electron density have same form but different coefficients. The following are their formula, respectively.

$$\rho^c(\vec{r}) = \sum_j G_{j,A} \exp(-\beta_{j,A} r^2) \quad 2-57$$

$$\rho^v(\vec{r}) = \sum_j F_{j,A} \exp(-\beta_{j,A} r^2) \quad 2-58$$

In the SCF process shown below, the potential coefficients $\{D_{j,A}\}$ should be converge. The process starts from an assumed set of coefficients which are usually based on the experience.



The SCF process shown above is to achieve the coefficient for each term of bases and potentials which are both in terms of GTOs. After this process, the OLCAO method use the self-consistent potentials and related bases to calculate electronic structure and optical properties of a material. Next section will briefly introduce how to perform

electronic structure, dielectric function and XANES. The detail can be achieved from Rulis's work.¹³

2.3 Electronic Structure and Spectroscopic Properties Calculation

The electronic structure and spectroscopic, especially XANES/ELNES calculation is presented in this section to further understand the calculated spectra. In this work, Vienna *ab initio* simulation package (VASP)^{16,17} is only used to relax the structure of crystal model; the primary method used in the present work to calculate the electronic structure, XANES spectra, and optical properties of the boron crystals is the *ab initio* orthogonalized linear combination of atomic orbitals (OLCAO) method^{12,14}. The OLCAO method is highly accurate and efficient when dealing with complex and large-scale structures¹⁸⁻³¹. In this section, the procedure of OLCAO calculation will first be presented, and then important technical aspects will be briefly introduced to help understand and/or interpret the calculated results in the following chapters.

The calculation of XANES spectra has been described in detail elsewhere^{8,32}. Briefly, it consists of three parts: (1) the calculation of the initial-state-wave function of the targeted core atom which is retained in the orthogonalization to the core procedure¹²; (2) the calculation of the final state wave function, taking into account the core-hole interaction; (3) the evaluation of the transition probabilities from a core orbital of the initial state to the unoccupied conduction band of the final state. The transition probability is proportional to the square of the dipole matrix element according to Fermi's Golden rule. It should be pointed out that the selection rule is automatically imposed in the full dipole transition matrix between the initial and the final-state wave functions. This is different

from using the orbital-resolved partial density of states (PDOS) to mimic the near edge spectra without information on the transition energy. Non-unique final states (such as L_3 edge, the final states include states with $j=1/2$ and $5/2$) result in different transitions (for L_3 edge, $j=3/2 \rightarrow j=1/2$ and $j=3/2 \rightarrow j=5/2$ according to the selection rule $\Delta j = \pm 1$). The intensity of XANES absorption is usually not proportional to PDOS in terms of the two transitions and energy onsets for the two transitions are usually different. Thus, PDOS cannot be simply added up to interpret the XANES spectra. However, for K-edge, the transition energy is only determined by final states (p -resolved states) since the initial states are mono-energy s -resolved states and the energy onset is automatically unique. Noticeably, ground p -resolved PDOS does not consider the core-hole interactions. Remarkably, OLCAO method can be used to calculate orbital-resolved PDOS with considering the core-hole interactions. Thus, K-edge can be interpreted by unoccupied excited p -resolved PDOS (including total and element-resolved). We can expect that the peak structure of K-edge for a target atom would be consistent to the peak structure of total unoccupied excited p -resolved PDOS and interpreted by the element-resolved unoccupied excited p -resolved PDOS. In this dissertation, the excited p -resolved PDOS are consistent to the basic contour of B-K edge and give a direct physical image. This idea has been tested in the three types of materials (elemental boron, boron-rich compounds, and MAX phase materials). Actually, the research shows that this idea is suitable to MAX phase materials and will be interpreted using MAX phase materials. For boron and boron-rich compounds, no significant observations were achieved and more work needs to be done in the future.

Technically, to minimize the core-hole interactions between replicated cells a supercell is constructed (unless the primitive cell is big enough) so that a 10 Å minimum

distance is obtained in any direction from a target atom to a replicated target atom in a neighboring cell. The supercell sizes of all the three types of materials are listed in each chapter. To compare XANES spectra with each other, the area under the spectrum over the transition energy range is normalized to unity. The energy onset is an important quantity in the XANES spectrum. In our method, it is obtained from the total energy difference between the initial state and the final state calculations. The experimentally measured XANES spectra generally represent the sum of the spectra from different sites for the same atomic species at different sites. In the present case, only the B-K edges are measured or calculated. Computationally, the total XANES spectrum is obtained as the weighted sum of the spectra from different sites for different groups of atoms. Moreover, the anisotropy of XANES spectra can be obtained by resolving the spectra according to the Cartesian components of the dipole matrix elements into the x , y , and z directions. This is one of the advantages of the supercell OLCAO method for XANES calculation^{25,33}.

For crystals without symmetry, the structural complexity of boron or boron-rich compounds makes it very difficult to distinguish the signal of any given specific site. Therefore, it is desirable to look for characteristic XANES features from different parts of the crystals. To this end, the XANES spectra for all the crystallographically non-equivalent sites of B are calculated and they are weighted and grouped into the total spectra for a particular group of interest. Thus, for crystals of α -t-B₅₁, β -t-B₁₀₆, β -t-B₁₉₀ models and B₁₁C-CBC which have only translational symmetry (space group = 1), 51, 106, 190, and 12, B-K edges are calculated, respectively. Because the dominant structure in the crystal is the icosahedron, we also computed the XANES spectrum of an isolated icosahedron with different B-B bond lengths to be used as a baseline for understanding the icosahedra present

in elemental boron and boron-rich compounds. A series of nine perfect icosahedral models with nine different bond lengths starting from 1.69 to 2.09 Å in a cubic cell ($20 \times 20 \times 20 \text{ Å}^3$) are used to characterize the spectral features and shift in peaks. Such hypothetical models are very useful for exploring and understanding the broader features in XANES spectra of elemental boron without going into excessive details. For those crystals with symmetry, the XANES for each atom was also performed to confirm that there is not an apparent difference. The detailed parameters can be found in each chapter as well.

CHAPTER 3
ELECTRONIC STRUCTURE AND SPECTROSCOPIC PROPERTIES OF
ELEMENTAL BORON

3.1 Introduction

Elemental boron and boron-rich compounds are characterized as hard materials^{1,34,35} with broad potential applications^{1,36}. Although they both have amazing physical properties^{1,36,37}, boron-rich compounds have attracted much more research interest because they have broader potential applications and tend to be easier to manufacture. However, single crystal boron-rich compounds have rarely been synthesized experimentally^{36,38,39}. Instead of ideal crystalline phases, the experimental samples usually exist as polycrystalline or as amorphous phases that consist of twelve atom boron icosahedra (B_{12}) and other elements (C, N, O, P, and As) that may or may not be incorporated into the icosahedra. Thus, these non-boron elements strongly influence the electronic and optical properties of boron-rich compounds³⁶. The role of the non-boron elements is sometimes difficult to identify, especially given the extreme complexity of the crystal structures. Therefore, pure crystalline elemental boron, which consists only of B_{12} icosahedra, clusters of icosahedra, and individual boron atoms is a natural starting point for investigation.

3.1.1 History

The boron element was first discovered in 1808⁴⁰ and amorphous boron was first discovered by Moissan¹ in 1892. The history of elemental boron has been shrouded in controversy since then. Due to the limitations of experimental techniques, the first pure crystalline boron was not reported until 1943. Roughly, the research on crystalline

elemental boron can be divided into two periods. The first period, beginning in 1943, was a period of discovery. The first crystalline phase, α -t-boron, was synthesized by Laubengayer *et al.*⁴¹ in 1943 and its structure was then studied by Hoard *et al.*^{42,43} and found to have 50 atoms per primitive cell. Later on, the discoveries of β -r-boron and α -r-boron phases were reported by Sands *et al.*⁴⁴ in 1957 and Decker *et al.*^{45,46} in 1959. Then, in 1960 β -t-boron, with 192 atoms, was first discovered by Talley *et al.*⁴⁷. In 1965, Wentorf *et al.*⁴⁸ claimed to discover a new phase (later known as the γ -phase) without structural or detailed information except for its density. The second period began just over a decade ago with the discovery of superconductivity⁴⁹ in elemental boron phases. This discovery led to new interest in the properties of elemental boron phases, especially those related to superconductivity^{1,49-52} and nanoscale phenomena^{1,53-63}. In 2003, the α -Ga type phase was predicted by Häussermann *et al.*⁶⁴ using *ab initio* simulations. During 2008 and 2009, the γ -phase was predicted and confirmed as γ -B₂₈ by Oganov *et al.*⁴⁰ and Solozhenko *et al.*⁶⁵ with definite structural parameters. However, some significant controversies remain concerning the structure of elemental boron.^{2,66,67} In this dissertation, based on the latest experimental reports with partial occupation, the structures of α -t-B₅₁ and β -t-B₁₉₀ were modified to get the theoretical models without any partial occupation and then the theoretical models were relaxed by VASP. The electronic structure and spectroscopic properties of all crystalline elemental boron were presented and discussed.

3.1.2 Difficulty and Challenge

The allotropes of solid elemental boron include six crystalline phases, amorphous phases, and nanoscale structures. The phase diagram⁴⁰ in Fig. 2 shows the crystalline phases including the α -rhombohedral phase (α -r-phase), β -rhombohedral phase (β -r-phase),

tetragonal phase (t-phase), γ -phase, and α -Ga type phase. Among them, the tetragonal phase consists of two sub-phases (not shown in Fig. 1): α -tetragonal phase (α -t-phase) and β -tetragonal phase (β -t-phase). Even though most of these phases were experimentally discovered^{40,41,44,45,47,48,65} a long time ago, their exact structures remain controversial.^{1,2,41–47,66,68–81} On the experimental side, the controversies arise from the innate complexity of the structures and the presence of defects (impurity atoms, structural defects, structural distortion, etc.) caused by extreme preparation conditions^{40,41,46,48,65,69–72,82}. On the theoretical side, the issues of electron deficiency^{83–85} and partial occupation^{2,70,80} lead to a variety of different crystalline models^{66,67,86} for the same phase. In most cases, theoretical simulations⁸⁵ have not satisfactorily reproduced the experimental observations^{83,87–89}. Therefore, the research history of elemental boron phases is accompanied by arguments and disagreements.

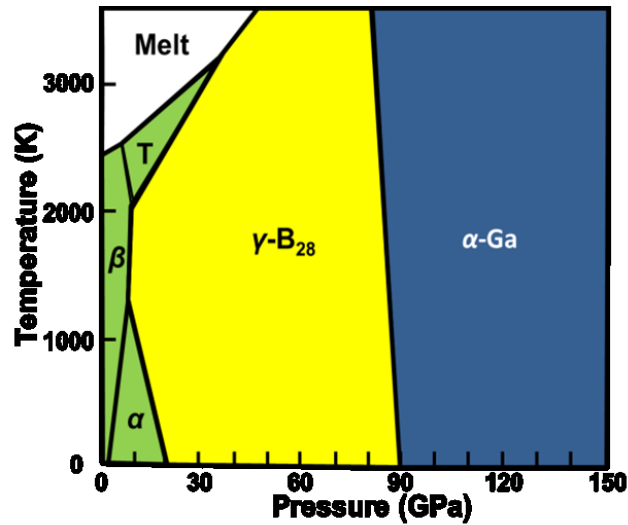


Fig. 2 The phase diagram of elemental boron.

3.1.3 Crystal Structure of Elemental Boron

Shown in Fig. 3 are the geometrical structures of the six crystalline phases of elemental boron. Aside from the α -Ga type, the structures of the other phases consist of icosahedra, icosahedral clusters, and non-icosahedral B atoms. The icosahedron is also a basic structural unit in the structure of boron-rich compounds. The understanding of structure and related properties can help to study boron-rich compounds.

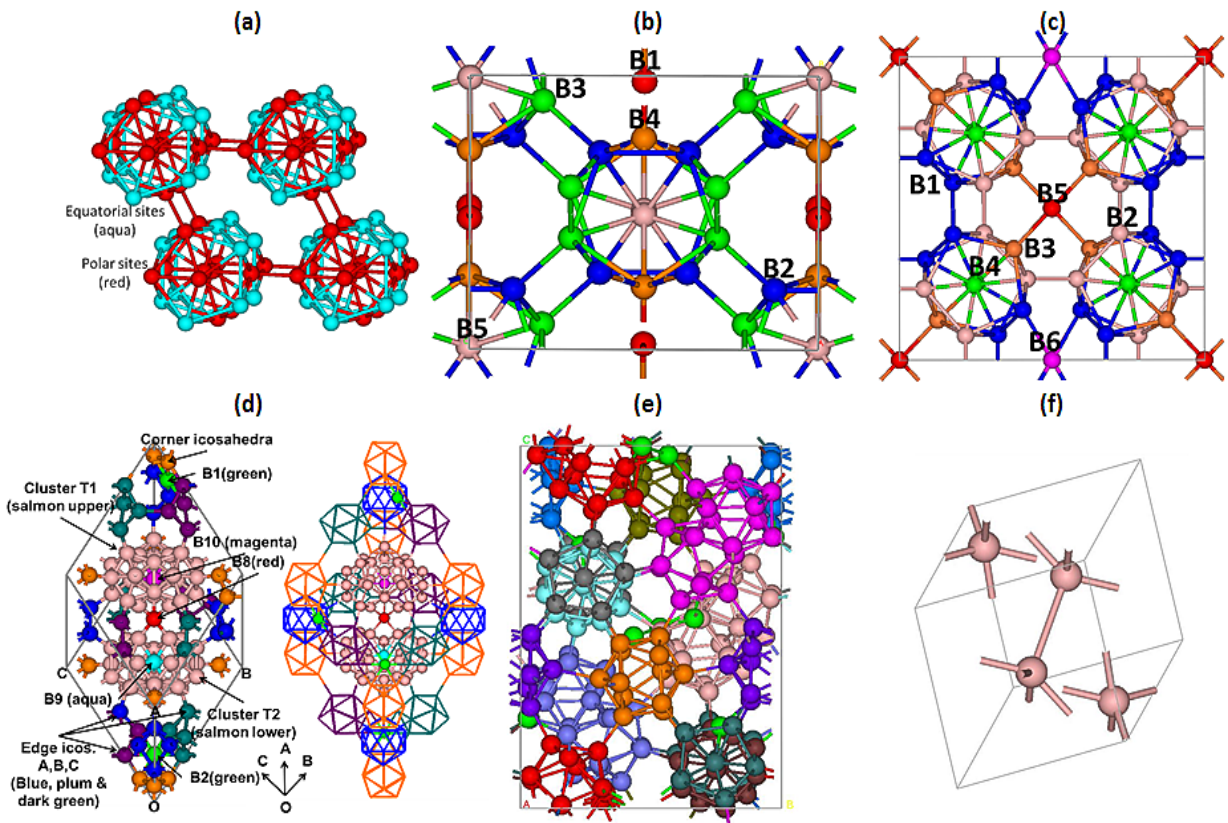


Fig. 3 Crystal structures of (a) α -r-B₁₂, (b) γ -B₂₈, (c) α -t-B₅₁, (d) β -r-B₁₀₆, (e) β -t-B₁₉₀, and (f) α -Ga type boron. In ordered systems (α -r-B₁₂, γ -B₂₈, and α -Ga type boron), different colors represent the different nonequivalent sites. In disordered systems (α -t-B₅₁, β -r-B₁₀₆, and β -t-B₁₉₀), different colors represent geometrical clusters, such as isolated icosahedron, icosahedral cluster, and individual isolated site. The specific sites in β -r-B₁₀₆, such as B9 and B10, are colored magenta although they belong to clusters T2 and T1, respectively.

Fig. 3 (a) shows the structure of α -r-B₁₂, the simplest structure among all the crystalline elemental boron phases. The structure of α -r-phase determined by McCarty *et al.*^{45,46} was generally accepted as α -r-B₁₂ for three decades until recently questioned by Werheit *et al.*⁶⁸ who compared the IR-active phonon spectra of α -r-boron with those of B₆O, B_{4.3}C, and β -r-boron, and suspected that there may be some additional single boron atoms in the unit cell of α -r-boron. However, detailed structural information was not acquired. Therefore, the conventional α -r-B₁₂ is used in the present study. The structure of α -r-B₁₂ consists of a slightly distorted icosahedron at the vertices of the rhombohedral primitive cell. The distortion results in symmetry breaking that generates two boron sites: polar (B_p) and equatorial (B_e) shown in Fig. 3.

Fig. 3 (b) shows the crystal structure of the γ -phase (γ -B₂₈)⁴⁰, which has five different B sites (B1 to B5). The structure consists of two B₁₂ icosahedra and two B₂ dumbbells (also boron pairs) that are all arranged in a NaCl-like structure. The 3c-2e in γ -B₂₈ was also reported by Häussermann *et al.*⁹⁰

Fig. 3 (c) shows the model structure of the α -t-phase that was used in the present study. The α -t-phase was originally believed to have 50 atoms (α -t-B₅₀)⁴²⁻⁴⁴. However, its structure is not well defined due to the issue of electron deficiency^{2,67,73,84,91}. Ekimov *et al.*² lately reported that there are seven boron sites (B1 to B7) in the primitive cell with B6 and B7 being partially occupied with occupancies of 0.310 and 0.062, respectively. Based on their report, the B7 site was neglected in the present work due to the low occupancy. One of the four B6 sites was kept to closely match the partial occupancy. The α -t-phase now has 51 atoms in the primitive cell. The structure for the present α -t-B₅₁ model was relaxed by using the Vienna *ab initio* simulation package (VASP) (see Section 3 for details on

methods). As shown in Fig. 3 (c), non-icosahedral boron atoms are located at $(\frac{1}{2}, 0, \frac{1}{2})$ and $(0, \frac{1}{2}, 0)$ (B5 sites) and at $(\frac{1}{2}, 0, 0)$ (B6 site). These sites bond with B3 and B1 type atoms in the icosahedral units. Spatially, the four separate icosahedra create an irregular tetrahedron (if each icosahedron is viewed as one vertex of the tetrahedron). Each slightly distorted icosahedron consists of four types of sites (B1 to B4). In such an icosahedron, there are four B1, four B2, two B3, and two B4 sites, totaling twelve atoms. To my knowledge, there are no 3c-2e bonds reported for α -t-boron.

The β -r-boron phase has been the most contentious in the past two decades with disagreement over the number of atoms and the structure of icosahedral clusters in the primitive cell^{44,75-77,79-81}. Geist *et al.*⁷⁷ proposed a configuration of: $4B_{12} + B_{28}-B-B_{28}$. At almost the same time, Hoard *et al.*⁷⁶ reported a β -r- B_{105} model with a $B_{84} + B_{10}-B-B_{10}$ configuration in which B_{84} represents a cluster consisting of one central icosahedron and twelve surrounding half-icosahedra where each boron atom of the central icosahedron is bonded with one of the half-icosahedra. However, Bullett *et al.*⁸³ pointed out that the structure of the $B_{84} + B_{10}-B-B_{10}$ configuration was not consistent with XRD results and that the calculated density of states (DOS) using that model suggested a metallic character which was not consistent with experimental measurement⁸⁸. In 2001, Jemmis *et al.*^{92,93} applied their *mno* rule to the β -r- B_{105} model and concluded that it was electron deficient. Bullett *et al.*⁸³ showed that the valence band of β -r-boron contains 320 electrons per unit cell. However, the β -r- B_{105} model has only 315 valence electrons so that additional interstitial sites are required to compensate for the electron deficiency. Therefore, an improved model would have 106 or 107 atoms in the primitive cell. Setten *et al.*⁶⁶ performed density functional calculations with the generalized gradient approximation to

study the thermodynamic stability of elemental boron models that were constructed using experimental data^{80,81}, and analyzed the band structure near the Fermi surface for each of these models. Two of these models, “106B16b” and “320B19”, were found to have the lowest total energy and their DOS showed semiconductive character which agrees with Slack’s experiment⁸⁰. Hence, in the present work, Setten’s “106B16b” model (β -r-B₁₀₆) was used. Fig. 3 (d) shows the crystal structure of β -r-B₁₀₆. In total, there are four B₁₂ icosahedra per rhombohedral cell. One icosahedron is centered at the vertex origin of the cell while the other three are located near the centers of the a, b, and c crystallographic axes. A defective B₂₈-B-B₂₇ cluster (instead of an ideal B₂₈-B-B₂₈) is located along the body diagonal line of each rhombohedron. Regarding labels, the B1 and B2 sites are non-icosahedral boron sites and each of them has six nearest neighbors. B8 is also a non-icosahedral site that connects two icosahedron-based clusters T1 (B₂₈) and T2 (B₂₇). Due to the absence of one atom in T2, B8 in Fig. 3 (d) has five nearest neighbors.

The β -t-phase is another elemental boron structure with a very complex structure. It was initially believed to have approximately 190-192 atoms⁴⁷. There should be 196 atoms^{69,70} if all of the 49 sites in the β -t-phase are fully occupied, but the reported^{69,70} occupancies of three of the four-atom sites [B(25), B(25p), and B(26)] are 0.5, 0.5, and 0.47, respectively. This means that there are only two out of four possible boron atoms at each of the B(25) and B(25p) type sites. B(26) can also be considered to have two atoms missing, rounding the 0.47 occupancy up to 0.5. Therefore, a set of models for the crystalline β -t-phase were built up and optimized by VASP. A model with the lowest energy consists of 190 boron atoms (β -t-B₁₉₀) shown in Fig. 3 (e). In this model, there are

ten non-icosahedral B atoms, eight icosahedra, and four icosahedral clusters each having two face-contacting icosahedra (B₂₁).

Fig. 3 (f) shows the primitive cell of the α -Ga type phase⁴⁰, which does not contain any icosahedron. This is a key difference between the α -Ga type and the other phases that have icosahedra. The lattice constants for all six crystalline elemental boron phases are listed in Table 1.

Table 1 Cell parameters and space group symmetries for the six crystalline elemental boron phases

Phase	a (Å)	b (Å)	c (Å)	α	β	γ	Space group	Super cell	Number of sites in super cell
α -B ₁₂	4.927	4.927	12.564	90.00	90.00	120.00	166	2×2×2	96
α -t-B ₅₁ *	8.848	8.895	4.954	90.00	90.00	90.00	1	1×1×2	102
γ -B ₂₈	5.043	5.612	6.921	90.00	90.00	90.00	58	2×2×2	224
β -B ₁₀₆ *	10.104	10.153	10.136	65.03	65.08	65.19	1	1×1×1	106
β -t-B ₁₉₀ *	9.989	9.970	14.003	90.00	90.00	89.00	1	1×1×1	190
α -Ga type	2.939	5.330	3.260	90.00	90.00	90.00	64	3×2×3	72

* indicates phases that have partial occupations.

3.1.4 Distortion of Icosahedron In Elemental Boron

To have an overall picture of the interatomic separations in these six crystals of elemental boron, the radial pair distribution functions (RPDFs) in the discrete histogram form are shown in Fig. 4 which is used to facilitate quantitative characterization of the disorder of each phase. The RPDFs of α -r-B₁₂, α -t-B₅₁, γ -B₂₈, and α -Ga type boron are

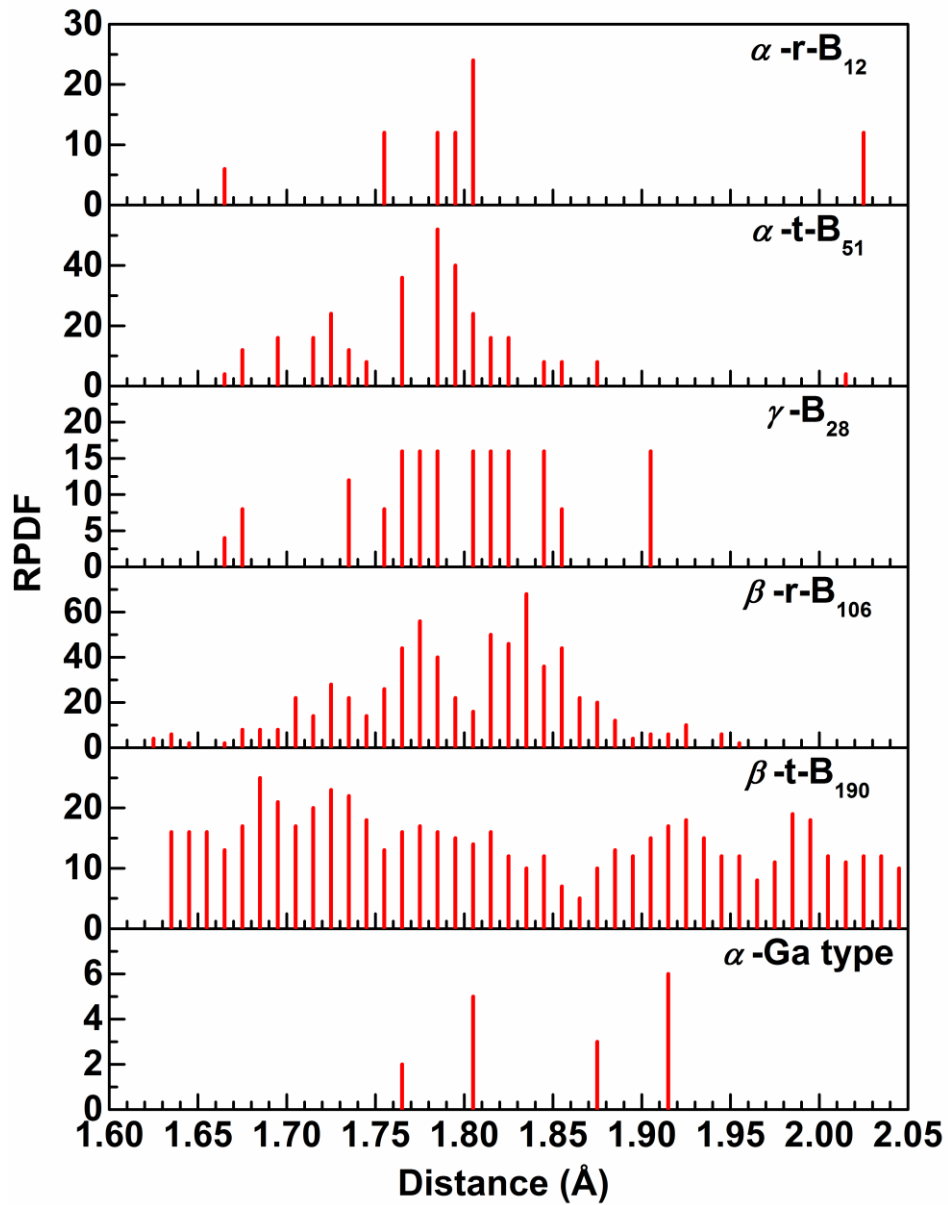


Fig. 4 Radial pair distribution function of crystalline elemental boron

restricted to relatively few specific distances, compared with those of β -t-B₁₉₀ and β -r-B₁₀₆. This is due to their more well-defined and simpler crystal structures that do not have any icosahedral clusters (for α -Ga type, there is no icosahedron). For example, the icosahedron in α -r-B₁₂ is only slightly distorted, preserving a relatively high order. The RPDF of α -r-B₁₂ shows that the majority of the bond lengths are in the range of 1.75 - 1.81 Å. The first line (at ~1.66 Å) and the last one (~2.02 Å) represents the inter-icosahedral B-B separations, while the others represent the intra-icosahedral atomic distances. In contrast, β -r-B₁₀₆ and β -t-B₁₉₀ have much broader distributions of bond lengths, especially in the case of β -t-B₁₉₀, indicating the complexity of the structures. RPDFs was used to interpret the distortion, as was the bond angle distribution (BAD).

All sites (12 sites) for a perfect icosahedron evenly distribute on a sphere with the same bond length and bond angles. These sites form 20 equilateral triangles and 12 equilateral pentagons. The characteristic angles for perfect icosahedron are 60° which is the interior angle of equilateral triangles and 108° which is the interior angle of normal pentagons. Since all sites of a perfect icosahedron distribute on a sphere, any position of a site which deviates from the original position (moving on/inside/outside sphere shown in Fig. 5) always results in distortion which can be displayed by BAD and RPDFs. Any deviation from the exact value implies that the structure of icosahedron is distorted. Tiny deviation represents a slight distortion while large differences indicates extreme distortion. Fig. 5(a-c) show that any of these three arrangements will lead to a deviation from the 60° or 108° angles. If the three points shown on these figures are the nearest neighbors each other, these figures can be used to interpret the deviation from 60° (such as \angle POQ in the visualized icosahedron model); if only two points are the nearest neighbors, the deviation

from the normal pentagon is considered (such as $\angle POS$ in a visualized icosahedron model). Fig. 5 (a) only occurs with very slight distortion as in α -r-B₁₂. Fig. 5 (b) and (c) can always be observed in a distorted icosahedron. Apparently, any movement for each site is related with the change of bond length and bond angle. For example, in Fig. 5 (b) with 108° angle

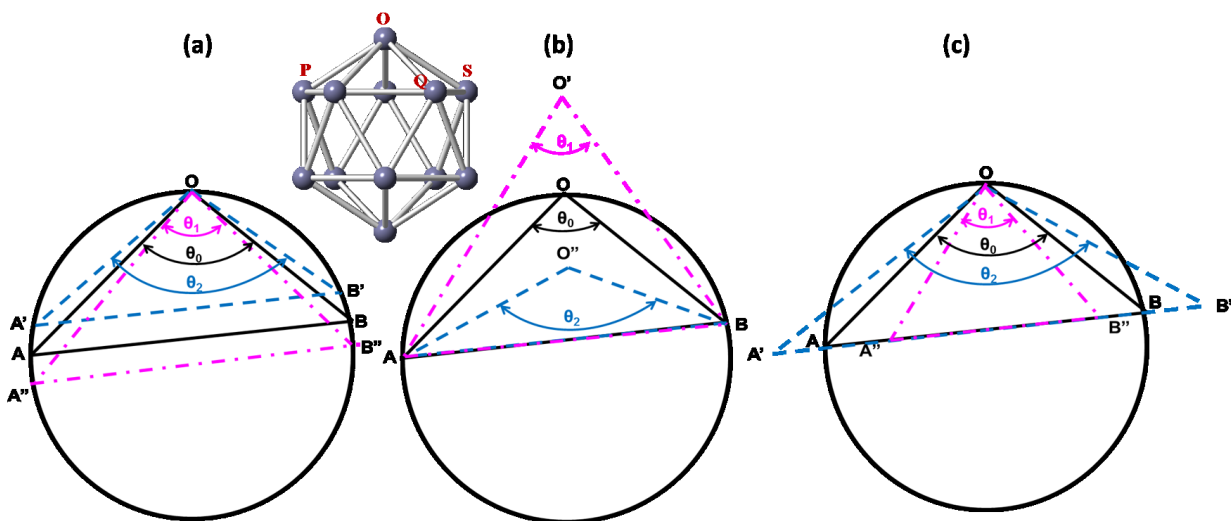


Fig. 5 Scheme for the variance of bond angles with (a) terminations of an angle moving on the sphere, (b) vertex moving outside/inside the sphere, and (c) terminations of an angle moving outside/inside the sphere. (the visualized model is used to demonstrate these figures.)

(the case for only two nearest neighbors), the distortion looks like the icosahedron “compressed” if the vertex site O moves to O’ (inside the sphere) or “pulled” if the vertex site moves to O’ (outside the sphere). The prior one is associated the angle is larger than 108° while the latter one is smaller than 108°. Apparently, this movement of site O leads to the angle $\angle OAB$ and $\angle OBA$ changing at $\sim 36^\circ$ which will not be shown in BAD since the upper limit for the bond length was set to stop counting the angle formed by atoms far away each other. The number difference between angles larger and that smaller than 108° indicates how distortion the icosahedron is. Thus, the RPDF and BAD can used to

demonstrate the distortion and the system disorder. RPDF and BAD will be used to observe the distortion of icosahedra in some crystals.

Fig. 6 (a) shows the number of angles larger than 60° is same to that of angles smaller than 60° , and that of angles larger than 108° is more than that of smaller than 108° . Roughly speaking, more polar sites in α -r-B₁₂ are slightly compressed in and more equatorial sites are slightly pulled out. Fig. 6 (b) shows the bonding including intra-icosahedron bonds and inter-icosahedron bonds. Later, it will be discussed in 3.1.5.

To clearly show the distortion of icosahedra in γ -B₂₈, only the BAD of intra-icosahedra is analyzed and shown in Fig. 7 (a). Obviously, the same BAD and RPDFs show that the same icosahedra result from the space symmetry in γ -B₂₈. Its distortion is more than α -r-B₁₂ since there are not exact 60° angles and the distributions around the

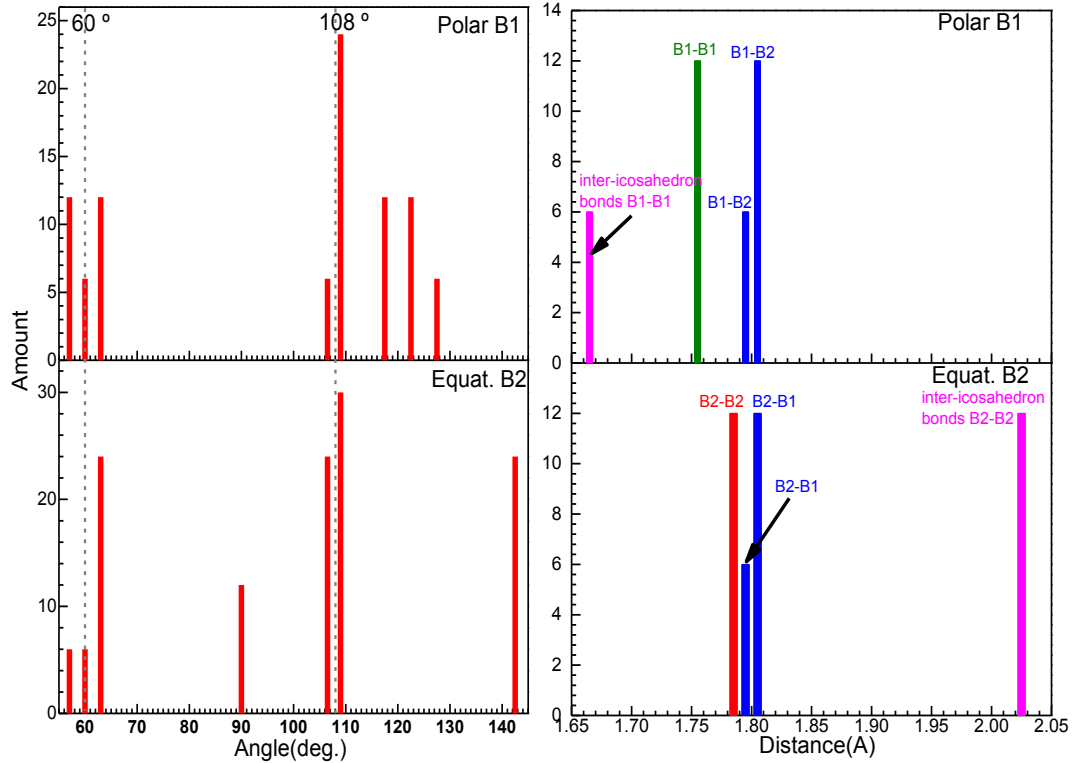


Fig. 6 (a) BAD and (b) RPDFs for α -r-B₁₂

characteristic angle value are not even. The number of angle smaller than 60° is more than that of larger than 60° . Same observation can be obtained for the 108° value. The distribution in the range of 117° to 127° originates from the incomplete icosahedra in a primitive cell (shown in Fig. 3 (b) at page 53) although the complete icosahedra can be observed in a periodic structure.

Similar observations of BAD and RPDFs of α -t-B₅₁, β -r-B₁₀₆, and β -t-B₁₉₀ can be achieved. Here, their decomposed BAD and RPDFs will not be extended in details. The models in Fig. 5 help to understand the distortion and also help to figure out different models with different bond length and. A set of models with different bond lengths were built up to find the characteristic features of icosahedron shown in section 3.3.2.

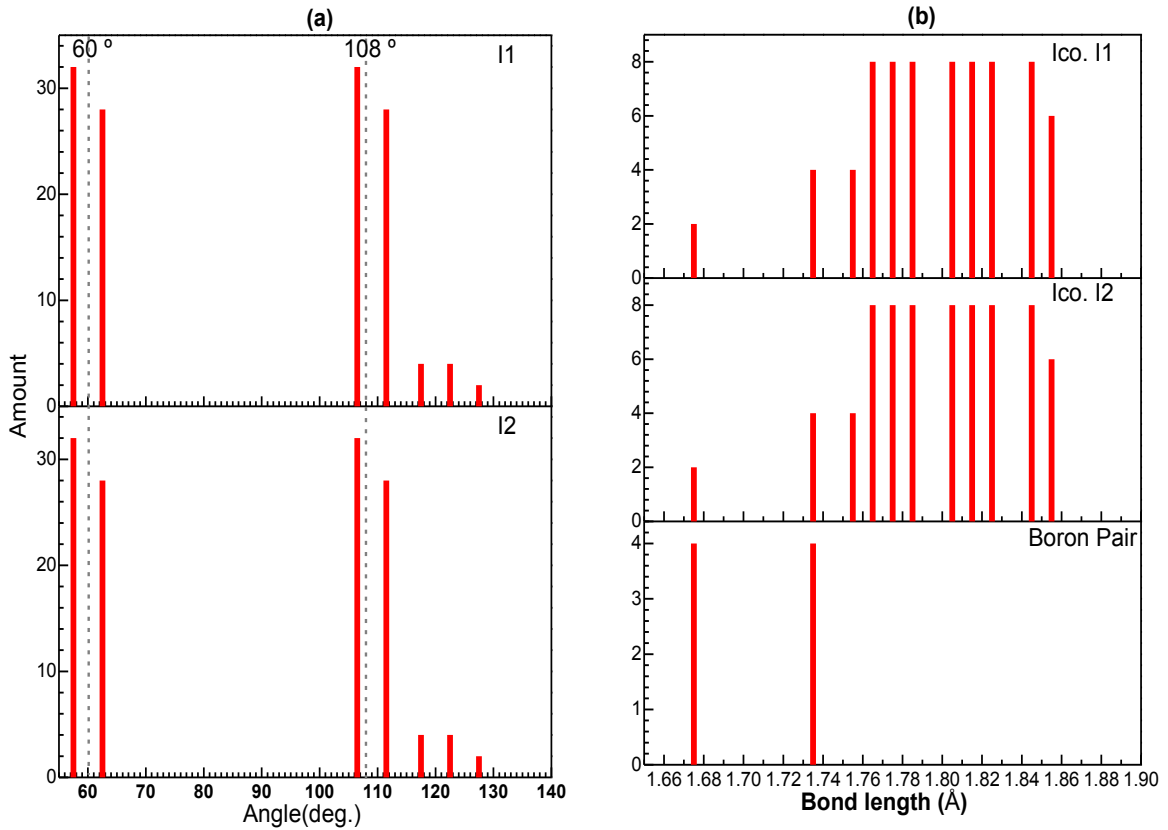


Fig. 7 (a) Bond angle distribution of intra-icosahedron and (b) RPDFs for γ -B₂₈.

3.1.5 Three-Center Two-Electron Bonds

The electron deficiency determines that there are existing unique bonds [three-center two-electron bonds (3c-2e)] in boron icosahedron. In this work, although 3c-2e bonds are not the primary section, they are related to the electron deficiency which also results in structural controversy. Thus, bond angle distribution (BAD) and RPDFs were used to briefly interpret the specific bonds in elemental boron.

Apparently, a constant or very similar bond length (associated with same or similar bond angles among the nearest neighbors) is one of required conditions to form 3c-2e bonds. However, since 3c-2e bonds is related to the electron deficiency, the two electrons should be shared by three atoms evenly and on a surface. This means that the 3c-2e bonds in the icosahedron are only formed by three polar boron atoms and that outside the icosahedra are only formed by three equatorial boron atoms.

Fig. 8 shows that the two sets of polar sites form two equatorial triangles in α -r-B₁₂. In Fig. 8, the top (bottom) three polar sites form a unique three center two electron (3c-2e) bonds⁹⁴. And each of three equatorial sites which are not neighbors to each other separately form a weak 3c-2e bond⁹⁵ which involves another two equatorial sites in two neighbor icosahedra. Fig. 6 shows the BAD and RPDFs calculated for each site in α -r-B₁₂. BAD includes the bond angles formed by inter-bonds and/or intra bonds, while RPDFs involves the distance between two sites in/out of the icosahedron/icosahedra/single sites. From Fig. 6 (a), the angle distribution in α -r-B₁₂ dominantly distributes at $\sim 60^\circ$ and $\sim 108^\circ$ which slightly diverge from the angle distribution (60° and 108°) of perfect icosahedron. The bond angle far from the two values is the bond angle of inter-icosahedra. Six 60° values imply that there are two equilateral triangles which are backed up by two sets of polar

atoms shown in Fig. 8. Another six 60° values are related to six equatorial sites associated with longer bond length [$>2.02\text{\AA}$ shown in Fig. 6 (b)]. From decomposed RPDFs for each site in α -r-B₁₂ shown in Fig. 6 (b), the bond length dominantly distribute in the range of $1.75 \sim 1.81\text{\AA}$ instead of a unique value. The bond length ($\sim 1.67\text{\AA}$) is the 1st nearest distance of two icosahedra, and the bond length (~ 2.02 to $\sim 2.03\text{\AA}$) is the 2nd nearest distance of two icosahedra. The prior one is the distance between two polar sites each of which is in different icosahedra; and the latter one is the distance between two equatorial sites which are in two different icosahedra. These two types of bonds are related to 3c-2e bonds which have been reported by Fujimori *et al.*⁹⁴ and He *et al.*⁹⁵. For γ -B₂₈, Fig. 7 shows that it is very possible for 3c-2e bonds to exist. Actually, this has been proved by Häussermann *et al.*⁹⁰

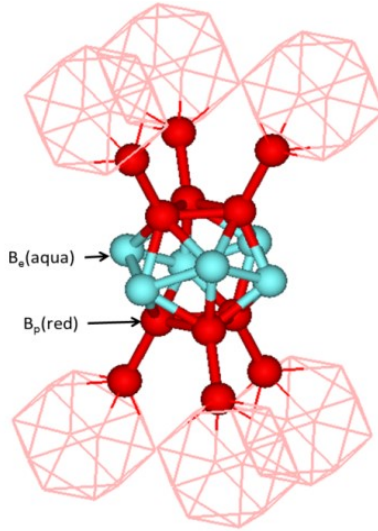


Fig. 8 Polar sites and equatorial sites in α -r-B₁₂.

3.2 Electronic Structure

Except for β -t-B₁₉₀, the electronic structures of the α -r-phase^{64,66,83,96-100}, γ -phase^{40,101}, α -t-phase^{67,83,99}, β -r-phase^{66,83,85}, and α -Ga type boron⁶⁴ have been studied by

many groups. For β -r-boron, Prasad *et al.*⁸⁵ predicted that the β -r-B₁₀₅ structure is metallic. But the calculated DOS of β -r-B₁₀₆ and β -r-B₃₂₀ using the VASP relaxed structure⁶⁶ show that β -r-boron is a semiconductor. Calculated band structures and total DOS (TDOS) obtained in this work for the six crystals are shown in Fig.9 and Fig. 10, respectively. These plots show that α -r-B₁₂, γ -B₂₈, and β -r-B₁₀₆ are all semiconductors with indirect band gaps; whereas α -t-B₅₁, β -t-B₁₉₀, and α -Ga type boron are metals. The calculated indirect (direct) band gap for α -r-B₁₂, γ -B₂₈, and β -r-B₁₀₆ are 2.68 (3.30), 2.10 (3.20), and 1.75 (1.83) eV, respectively. They are listed in Table 2 together with the reported experimental values, with agree which our calculations quite well. For α -t-B₅₁ and β -t-B₁₉₀, Fig.9(c) and (e) show flat states near the Fermi surface or the band edges which imply large effective masses for charge carriers in these crystals. Therefore, they are unlikely to be good electrical conductors. For the α -Ga type boron, there is a pseudo-gap, or a deep minimum at the Fermi level. This pseudo-gap will have influence on the optical dielectric properties which will be discussed in 3.4.

The TDOS in Fig. 10 shows the existence of three generally identifiable characteristic segments below the Fermi surface for each of the elemental boron phases except the α -Ga type. The ranges of the three segments for these phases are roughly from -20 to -15, -15 to -10, and -10 to 0 eV. To better understand the different TDOS from each elemental boron crystal, the atom-resolved partial DOS (PDOS) of each atom were regrouped to obtain the PDOS for each icosahedron or icosahedral cluster. This style of PDOS grouping is denoted as an ico-PDOS for both an individual icosahedron and an icosahedral cluster. The structure of α -r-B₁₂ consists of interconnected icosahedra only, thus the ico-PDOS of α -r-B₁₂ is the same as its TDOS. In γ -B₂₈, the two icosahedra are

crystallographically identical with the same ico-PDOS, hence only one ico-PDOS is shown in Fig. 11. The ico-PDOS of γ -B₂₈ contains the three characteristic segments in the TDOS while the PDOS of the boron dumbbell pair does not show three segments. Although the four icosahedra in α -t-B₅₁ are slightly distorted, their PDOS do not show any apparent difference from each other. Therefore, only one averaged ico-PDOS is presented in Fig. 12. In the averaged ico-PDOS for α -t-B₅₁, a series of three segments can also be observed in energy ranges similar to those of the ico-PDOS segments for α -r-B₁₂ and γ -B₂₈. It is obvious that the three-segment feature is strongly correlated with the icosahedral structure.

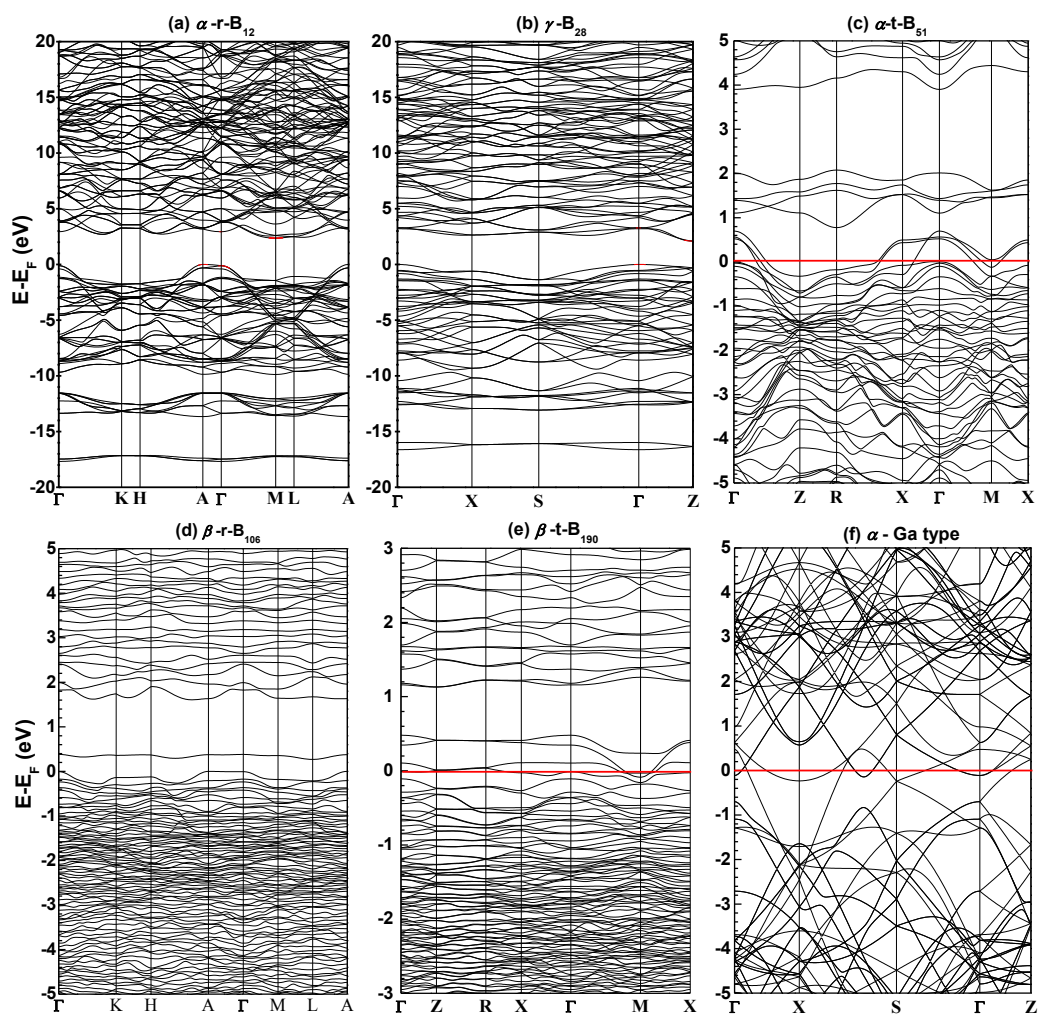


Fig.9 Calculated band structures of (a) α -r-B₁₂, (b) γ -B₂₈, (c) α -t-B₅₁, (d) β -r-B₁₀₆, (e) β -t-B₁₉₀, and (f) α -Ga type boron.

Table 2 Measured and calculated band gaps (eV) of α -r-B₁₂, γ -B₂₈, and β -r-B₁₀₆

Phase	Calculated band gaps		Measured band gaps (eV)
	Indirect gaps (eV)	Direct gaps at Γ point (eV)	
α -r-B ₁₂	2.68	3.30	2.4 ¹⁰²
α -t-B ₅₁	-	-	-
γ -B ₂₈	2.10	3.20	2.1 ¹⁰¹
β -r-B ₁₀₆	1.75	1.83	1.4 ⁸⁷ , 1.6 ⁶⁴ , 1.8 ¹⁰²
β -t-B ₁₉₀	-	-	-
α -Ga type	-	-	-

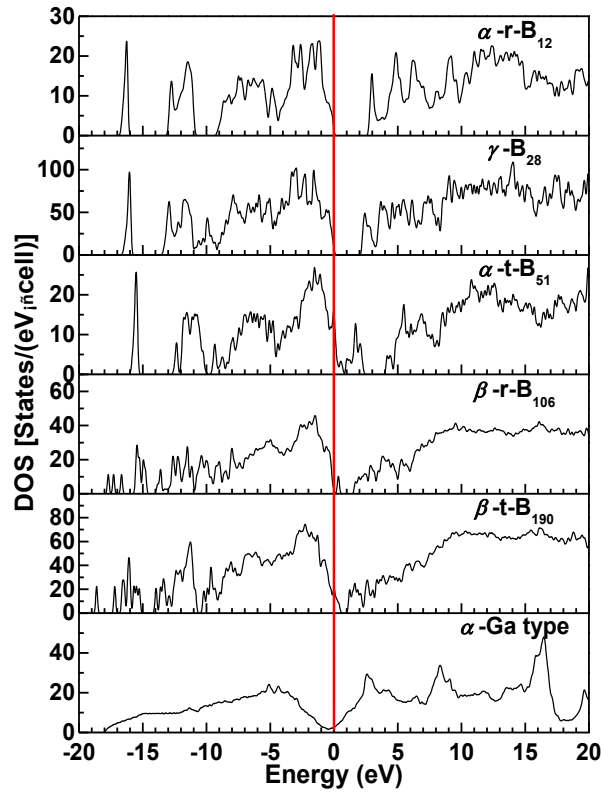


Fig. 10 Calculated TDOS of α -r-B₁₂, γ -B₂₈, α -t-B₅₁, β -r-B₁₀₆, β -t-B₁₉₀, and α -Ga type boron (The vertical red line denotes the Fermi level).

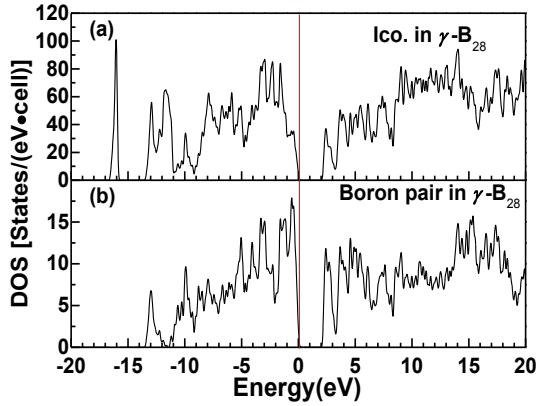


Fig. 11 Calculated PDOS of (a) the icosahedron and (b) the boron pair in γ -B₂₈.

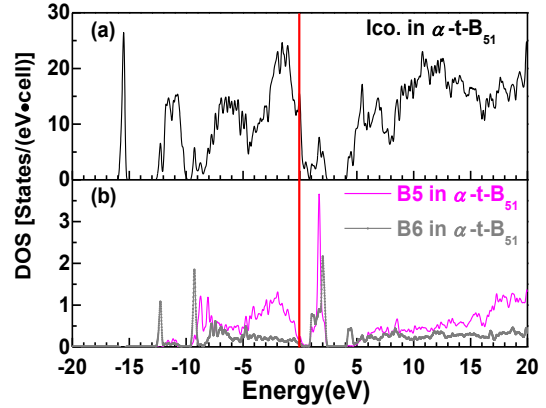


Fig. 12 Calculated PDOS of (a) the icosahedron and (b) the isolated boron atoms in α -t-B₅₁.

When it comes to β -r-B₁₀₆ and β -t-B₁₉₀ which have more complex crystal structures, the electronic structure becomes more complicated. The ico-PDOS for β -r-B₁₀₆ are shown in Fig. 13(a) and the atom-resolved PDOS of the non-icosahedral atoms (B1, B2, and B8) and specific atoms (B9 and B10) are shown in Fig. 13(b). Although β -r-B₁₀₆ is a semiconductor, there is a “defect-like” state above the VB edge at 0.27 eV. This “defect-like” state was attributed to a core-hole trapping center by Prudenziati⁷⁸ using transient photoconductivity measurements and by Werheit *et al.*⁸⁸ using optical absorption measurements. Fig. 13 shows that this “defective” state originates from the T2 cluster which has one boron atom missing from the more regular 28-atom cluster. From a broader viewpoint, the TDOS near the bottom of the CB is primarily contributed to by the T1 and T2 clusters (~88%) and secondarily by the B1 and B2 non-icosahedral sites (~12%). Comparing the ico-PDOS of β -r-B₁₀₆ with that of α -r-B₁₂ and γ -B₂₈, one can see that the band gap of β -r-B₁₀₆ is narrower because of the presence of the icosahedral clusters and the two non-icosahedral atoms. However, the contributing structures in β -r-B₁₀₆ are fairly

separate from each other in the crystal. This might suggest that there is relatively low carrier mobility unless foreign atoms are present. Also in Fig. 13 (a), there exist three distinct peaks in the energy range from -20 to -15 eV labeled as a, b, and c, which clearly originate from clusters T1, T2, and the icosahedron at the vertex, respectively.

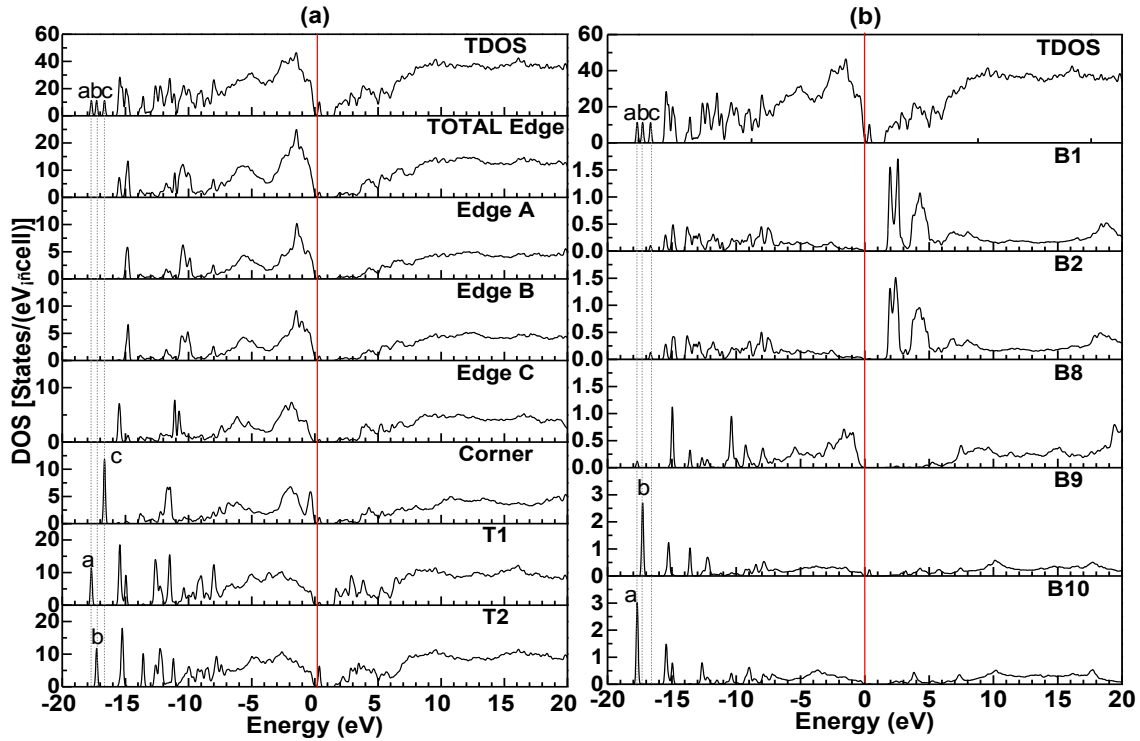


Fig. 13(a) TDOS and Ico-PDOS of β -r-B₁₀₆; (“TOTAL Edge” represents the sum of density of states of icosahedra along edges A, B and C; “Edges A”, “Edges B”, and “Edges C” represent the DOS of each single icosahedron along the edges; “Corner” represents the DOS of the icosahedron at the lattice corner; “T1” and “T2” represent grouped PDOS for icosahedral clusters); (b)TDOS and PDOS of special sites in β -r-B₁₀₆ (“B1”, “B2”, “B8”, “B9”, and “B10” represent specific sites in β -r-B₁₀₆).

Fig. 14 shows the ico-PDOS of the icosahedra (I1 - I8), the icosahedral clusters (C1 - C4), and the non-icosahedral atoms (S1 - S10) in β -t-B₁₉₀. In general, the ico-PDOS of icosahedron and icosahedral cluster show very complex electronic structures, making it almost impossible to correlate directly with the crystal structure. There still exist three

segments in the ico-PDOS of I1-I8 and C1-C4, similar to the three segments in the ico-PDOS of α -r-B₁₂, γ -B₂₈, α -t-B₅₁, and β -r-B₁₀₆ except with less clear boundaries between the segments. The alignment of PDOS peaks can give some indication of the nature of the electronic interaction between each of these groups of atoms. The ico-PDOS of clusters C1 and C3 are very similar and so are those of C2 and C4. Clusters C1 - C4 each have two face-contacting icosahedra. Each cluster is bonded to either two (for C1 and C3) or four (for C2 and C4) boron atoms from neighboring icosahedra. The bond distances between the clusters and the neighboring icosahedra are 1.83 and 1.84 Å for the four atoms in C2 and C4, and 1.77 Å for the two atoms in C1 and C3. Obviously, these bond-forming distances can be attributed to the distortion of the icosahedra which is also reflected in the ico-PDOS.

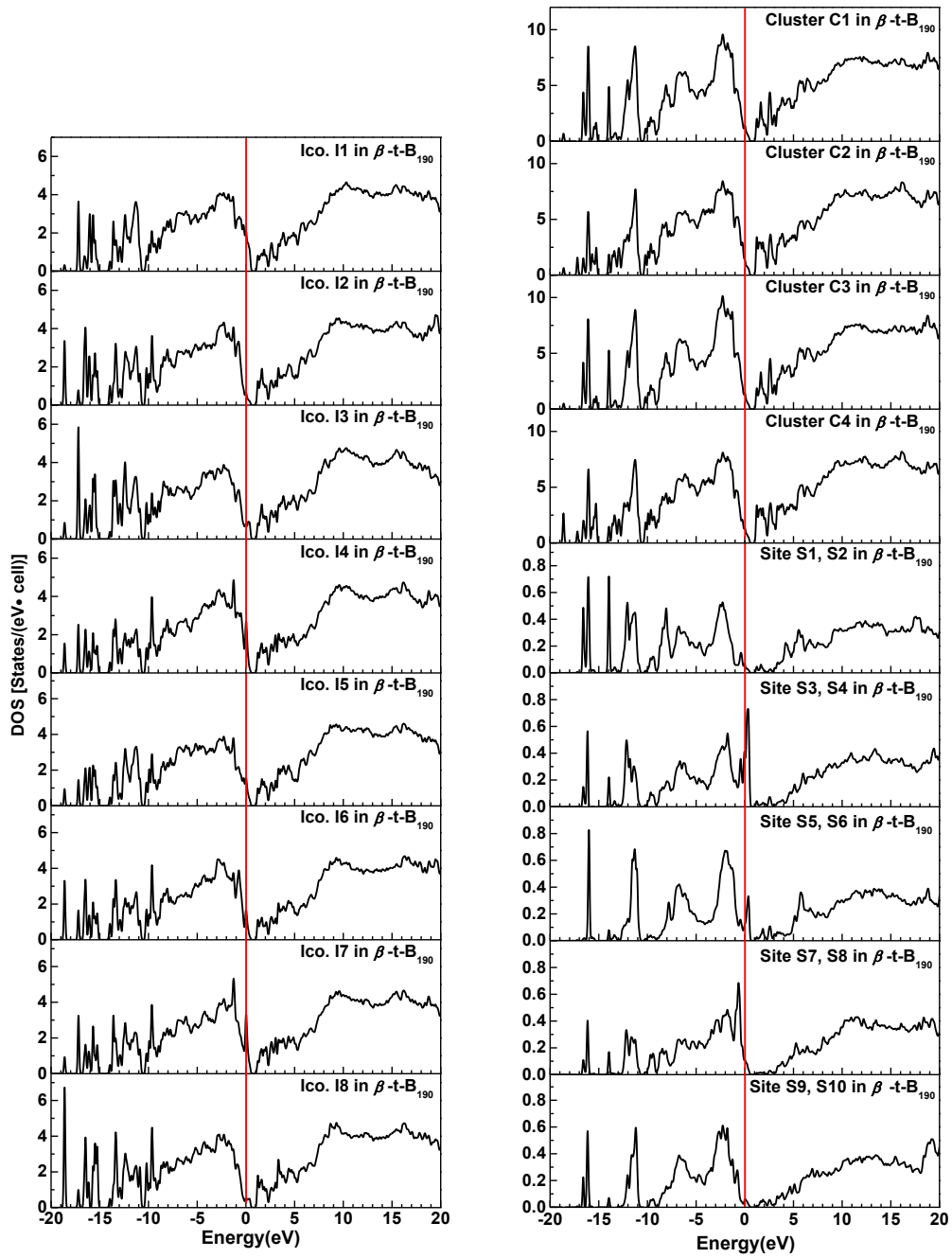


Fig. 14 Ico-PDOS of isolated icosahedron (I1 to I8), icosahedral cluster (C1 to C4), and isolated sites (S1 - S10, group in two each) in β -t-B₁₉₀. The atom-resolved PDOS of sites S1 and S2 (also S3 and S4, S5 and S6, etc.) are the same and are put together.

3.3 XANES Spectra

The XANES spectra or the B-K edges for every crystallographically non-equivalent boron atom in each of the six elemental boron crystals were calculated using the supercell OLCAO method. These spectra can then be added together with a weighting factor based on the population of each site to study the whole crystal spectrum or the spectrum associated with specific components of the crystal (*e.g.* an icosahedron).

3.3.1 XANES Spectra of α -r-B₁₂ and β -r-boron

To the authors' knowledge, there are only two papers^{102,103} reporting the experimental XANES spectra of two crystalline elemental boron phases: α -r-B₁₂ and β -r-boron. They are plotted in Fig. 15 (a) and (b) in comparison with our calculated XANES spectra. The calculated spectra are shifted downward by 4.09 eV and 2.48 eV respectively to align the most dominant peaks [B in Fig. 15(a) and A in Fig. 15(b)] with the experimental ones. For α -r-B₁₂, our calculated curve satisfactorily reproduces the features (A through F) of the experimental curve. As for β -r-boron, our calculated curve using the β -r-B₁₀₆ model⁶⁶ also agrees quite well with the experimental data. It should be noted that the experimental curves in Fig. 15 do not have the backgrounds subtracted. The good agreement for α -r-B₁₂ and β -r-boron give credence to our calculation and encouraged us to predict the XANES spectra of α -t-B₅₁, β -t-B₁₉₀, and α -Ga type boron without the support of experimental data.

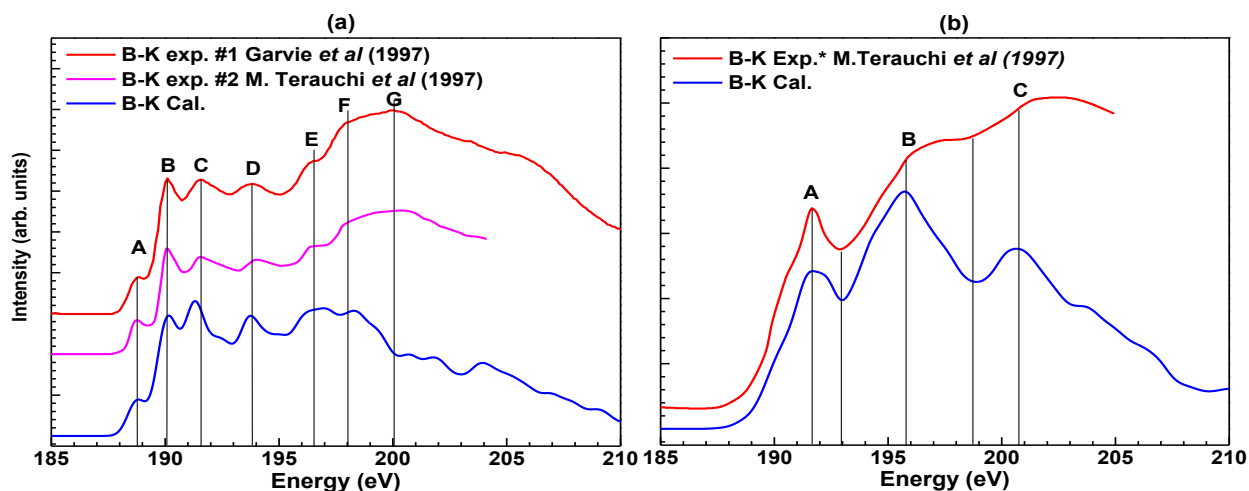


Fig. 15 Experimental and calculated XANES spectra of (a) α -r-B₁₂^{102,103} and (b) β -r-Boron¹⁰².

3.3.2 XANES Spectrum of an Isolated Boron Icosahedron and Elemental Boron Phases

For elemental boron, there is only one type of atom: boron. However, bond lengths, bond angles, and the number of nearest neighbors all affect the XANES spectrum of a target atom to varying degrees. To study the dependence that XANES spectra of B₁₂ icosahedra have on the B-B bond length (BL), the XANES spectra for a set of perfect isolated icosahedra with different BLs were calculated and shown in Fig. 16 (a). This simplified approach provides sufficient detail to allow us to identify characteristic groupings of XANES spectral features in the icosahedral structure. Fig. 16 (a) shows that the XANES spectra of isolated icosahedra are very sensitive to variations in the BL. In Fig. 16 (b), I plot the change in energy for each peak in Fig.11 (a) as a function of BL with each curve categorized according to the pattern of its slope. Fig. 16 shows that there are three characteristic features (A, B, and C) in the XANES spectra of the perfect icosahedra. Feature A is relatively narrow and sharp. The width of feature B (including sub-peaks B1, B2, and B3) is broader than A, but narrower than C (C1 and C2 combined). Noticeably, the peak intensity of A is slightly higher than B, and much higher than C. These features

will be applied to study the XANES spectra of the elemental boron crystals. Subsequently, the XANES spectrum of the isolated icosahedron with a B-B BL of a 1.99 Å is selected to compare with the XANES spectra of the icosahedra from the various elemental boron phases where the BL of the icosahedra ranges from 1.64 to 1.95 Å). This selection is based on the fact that the energy position of peak A closely matches those in the boron crystals.

Fig. 17 shows the calculated B-K edges of the perfect icosahedron (BL: 1.99 Å, top panel) and the XANES spectra (weighted sum) obtained from the six crystalline elemental boron phases. Except for the non-icosahedron containing α -Ga type boron, which has a

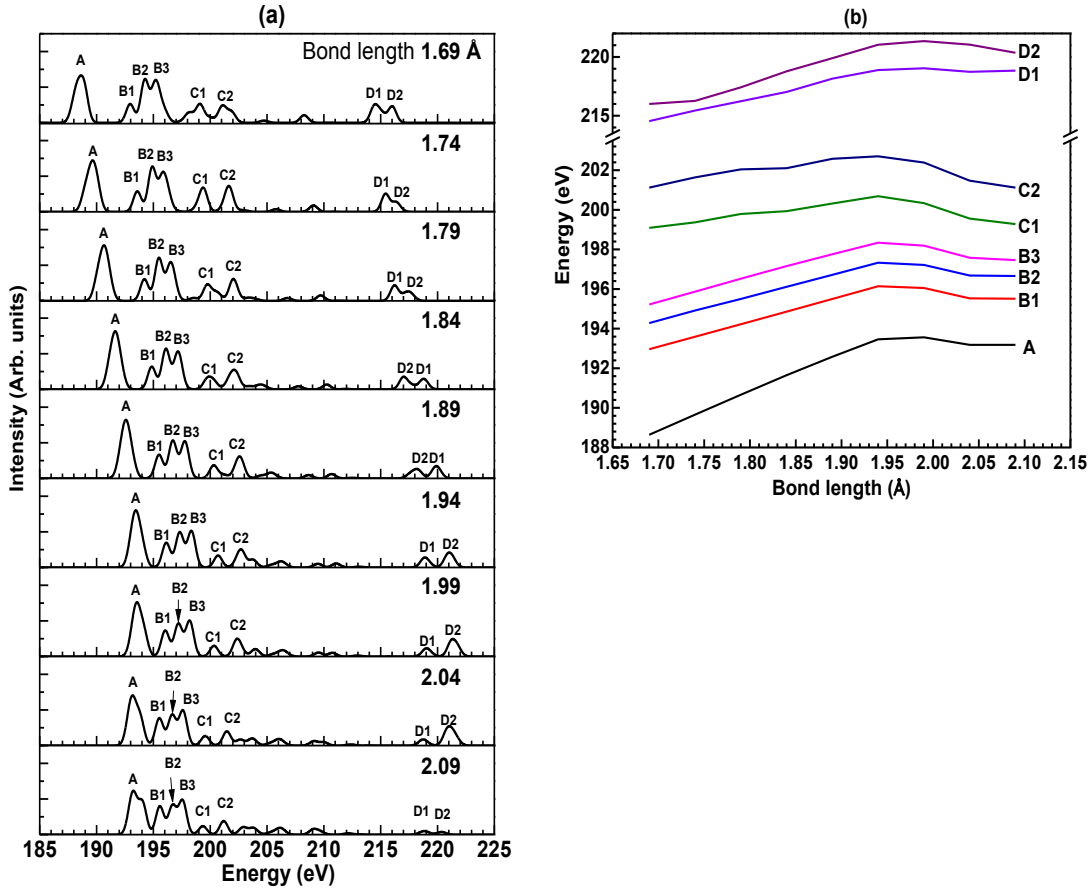


Fig. 16 (a) XANES spectra of perfect icosahedron models with different bond lengths; (b) Energy shifts of peak locations with the changes of the bond lengths.

primary absorption in the range from 188 to 206 eV, the absorptions in all other phases are

in a range from 190 to 215 eV. The XANES spectrum of the five icosahedron-containing phases can be roughly divided into four segments (A, B, C, and D), similar to those for the perfect icosahedron. The spectral features become smoother from α -r-B₁₂ to β -t-B₁₉₀ with an increasing number of icosahedra and icosahedral clusters. The XANES features of these five phases agree with those of the perfect icosahedron in terms of the width and intensity. The spectrum for the α -Ga type boron also has four segments but the shapes of the features and the energy ranges are quite different from those of the other phases. Such differences can be attributed to the lack of icosahedra in the α -Ga type boron. Therefore, the three peak features (A, B, and C) in the first five elemental boron phases can be considered as a signature of the presence of icosahedral units in these phases.

Next, the XANES spectra of Fig. 17 resolved into icosahedral clusters in all five of the crystalline phases (except α -Ga type) by summing up the spectra from the boron atoms in the respective icosahedra or icosahedral clusters. This is shown in Fig. 18. Structurally, γ -B₂₈ has two icosahedra in its primitive cell which are only slightly different and only one spectrum is shown. Similarly, α -t-B₅₁ has four icosahedra but only one spectrum is shown. The XANES spectrum of the icosahedra in α -t-B₅₁ is quite different from that of the icosahedra in γ -B₂₈ which can be attributed to the differences in geometrical and electronic structures. For example, the pre-peak in the XANES spectrum of α -t-B₅₁ is due to the core level transitions to the low-lying unoccupied states.

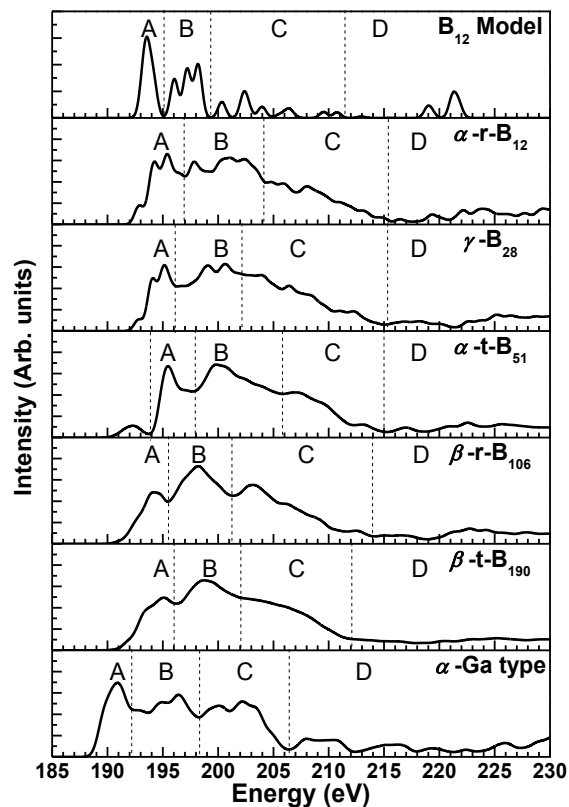


Fig. 17 XANES spectra of the perfect icosahedron model (B_{12}), α -r- B_{12} , γ - B_{28} , α -t- B_{51} , β -r- B_{106} , β -t- B_{190} , and α -Ga type boron.

In β -r- B_{106} , the spectra of the three icosahedra found on the crystallographic axes are somewhat different from the spectrum of the vertex icosahedron. In particular, the XANES spectra of the T1 and T2 clusters in β -r- B_{106} show a remarkable difference in the first 5 eV range from the edge onset. Such a difference is difficult to observe in experiments and it originates from the defect in T2.

For β -t- B_{190} , there are more icosahedral clusters and their XANES spectra are more broadened due to increased complexity in the structure. Noticeably, the local structure of different icosahedra is similar to those in α -t- B_{51} . Thus, the XANES spectra of different icosahedra in β -t- B_{190} are similar to those of α -t- B_{51} . However, the three peak features are

still in the same energy range from 190 to 215 eV for all the icosahedra and icosahedral clusters.

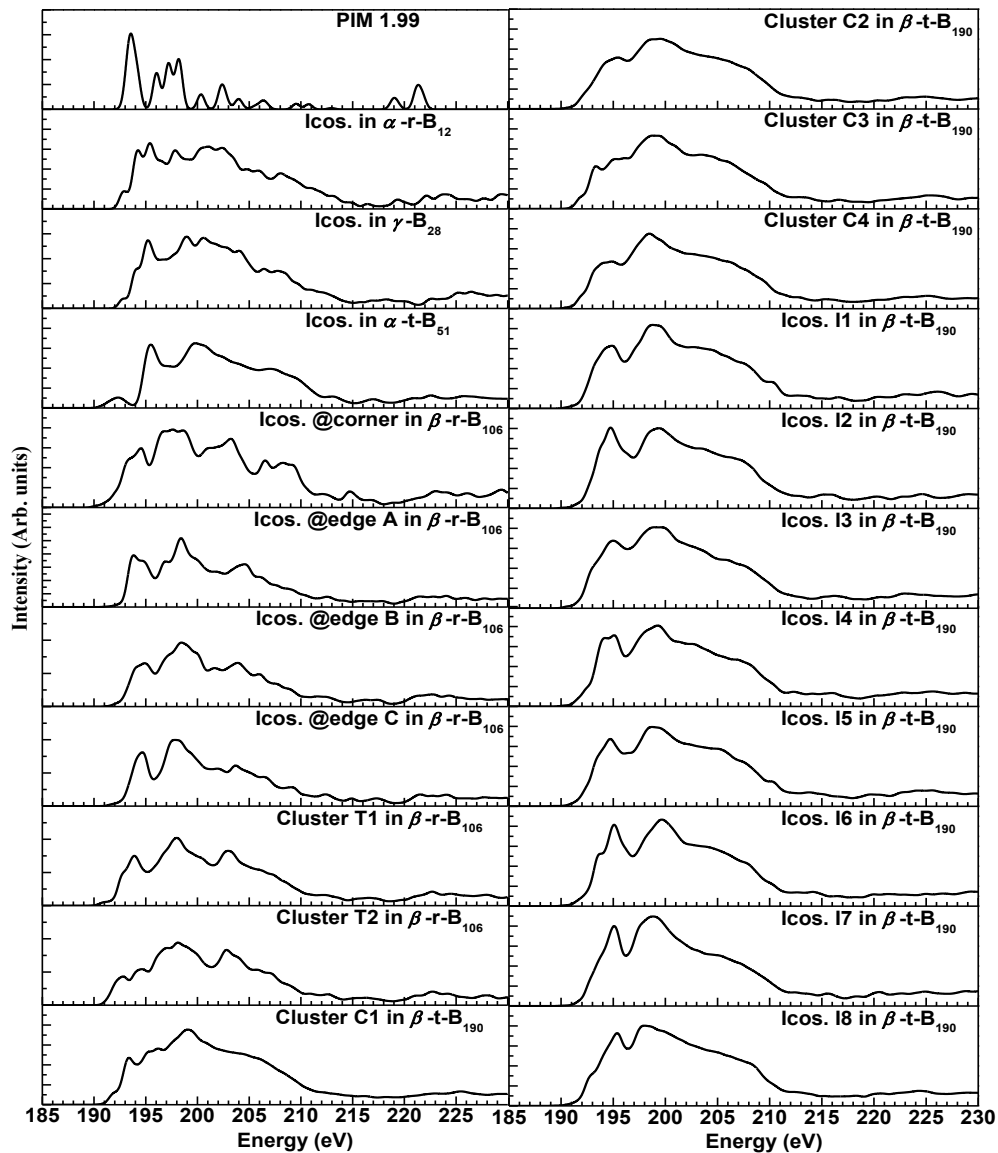


Fig. 18 XANES spectra of icosahedral clusters in α -r-B₁₂, α -t-B₅₁, γ -B₂₈, β -r-B₁₀₆, and β -t-B₁₉₀.

3.4 Valence Band Optical Properties

In addition to the XANES spectra, I calculated the interband optical properties in the form of the complex dielectric functions of the six elemental B crystals. To the best of the authors' knowledge, there is only one experimental report¹⁰² on the EELS of α -r-B₁₂ and β -r-boron. The EELS spectrum was converted into the complex dielectric function for comparison with the calculated data¹⁰⁴. Fig. 19 shows the comparison between the experimentally obtained $\epsilon(\omega)$ curves for α -r-B₁₂ and β -r-boron and our calculation. The $\epsilon_2(\omega)$ was first discussed, and then $\epsilon_1(\omega)$ which is derived from the Kramers-Kronig conversion of $\epsilon_2(\omega)$ ¹².

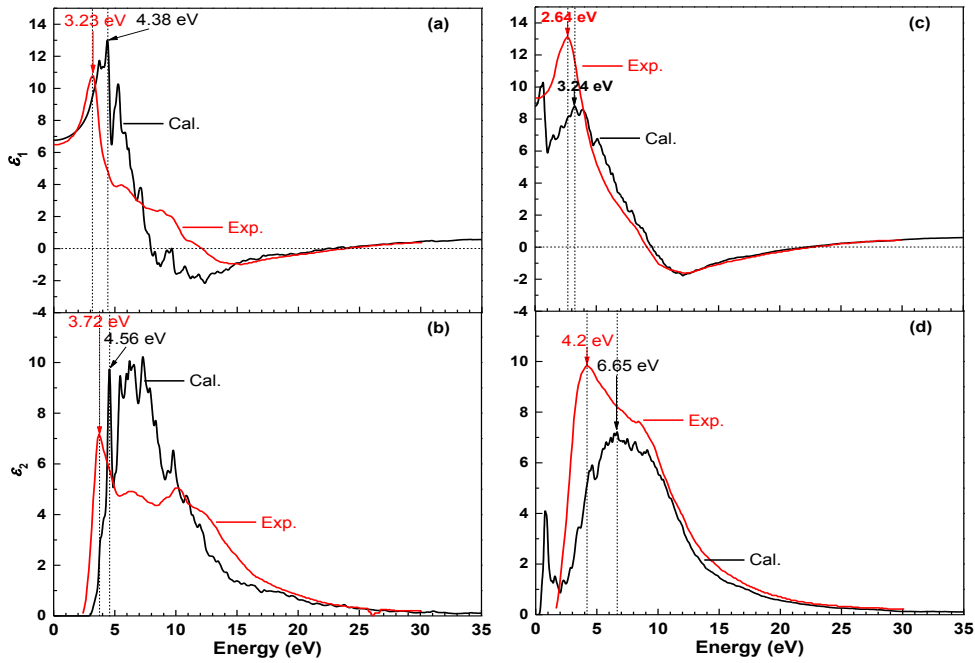


Fig. 19 Experimental¹⁰² (red) and calculated (black) dielectric functions (ϵ_1 , ϵ_2) for α -r-B₁₂ (a, b) and β -r-boron(c, d).

In Fig. 19 (b) the calculated absorption threshold of $\epsilon_2(\omega)$ for α -r-B₁₂ is 2.93 eV which is slightly larger than the experimental value of 2.4 eV. This is reasonable since it is between the direct (2.68 eV) and indirect (3.30 eV) band gaps of α -r-B₁₂. Although the

energy position of the first dominant peak of the calculated $\epsilon_2(\omega)$ is at 4.56 eV, which is a little larger than the experimental value of 3.72 eV, the contour of $\epsilon_2(\omega)$ is in modest agreement with that from the experimental measurement. For the semiconductive α -r-B₁₂, the first dominant peak of the calculated $\epsilon_1(\omega)$ is at 4.38 eV while the corresponding experimental peak is at 3.23 eV. The calculated value of $\epsilon_1(0)$ is 6.77, which is close to the experimental value of 6.5¹⁰². The calculated refractive index (n) is calculated to be 2.60. There are no corresponding experimental values for comparison.

Fig. 19 (d) shows that the calculated absorption threshold of $\epsilon_2(\omega)$ for β -r-B₁₀₆ is 0.27 eV, which agrees with the energy position of the calculated “defect-like” state in β -r-B₁₀₆. The pre-peak of $\epsilon_2(\omega)$ originates from the “defect-like” states in the electronic structure. Due to this absorption, the threshold for the dominant absorption is unclear. The minimum in the absorption before the dominant absorption is at 2 eV which is comparable with the calculated band gap (1.83 eV) for β -r-B₁₀₆. The experimentally measured $\epsilon_2(\omega)$ does not show any pre-peak. It implies that either the structure of β -r-B₁₀₆ used for the calculation needs improvement or that the experimental sample was not as pure and defect free as desired. In Fig. 19 (c), the $\epsilon_1(\omega)$ curve for β -r-B₁₀₆ shows a small peak structure at ~1 eV that can also be attributed to the “defect-like” state. The energy position of the dominant peak is at 3.24 eV which is a little larger than the experimental value of 2.64 eV. Above 1 eV, the contour of the calculated $\epsilon_1(\omega)$ is similar to that of the experimental curve. The calculated $\epsilon_1(0)$ is 8.80, which is slightly smaller than the experimental value¹⁰² of 9.3. According to the measurement and analysis by Terauchi *et al.*¹⁰², the smaller $\epsilon_1(0)$ value for α -r-boron compared to β -r-boron is due to the larger band gap of α -r-boron compared

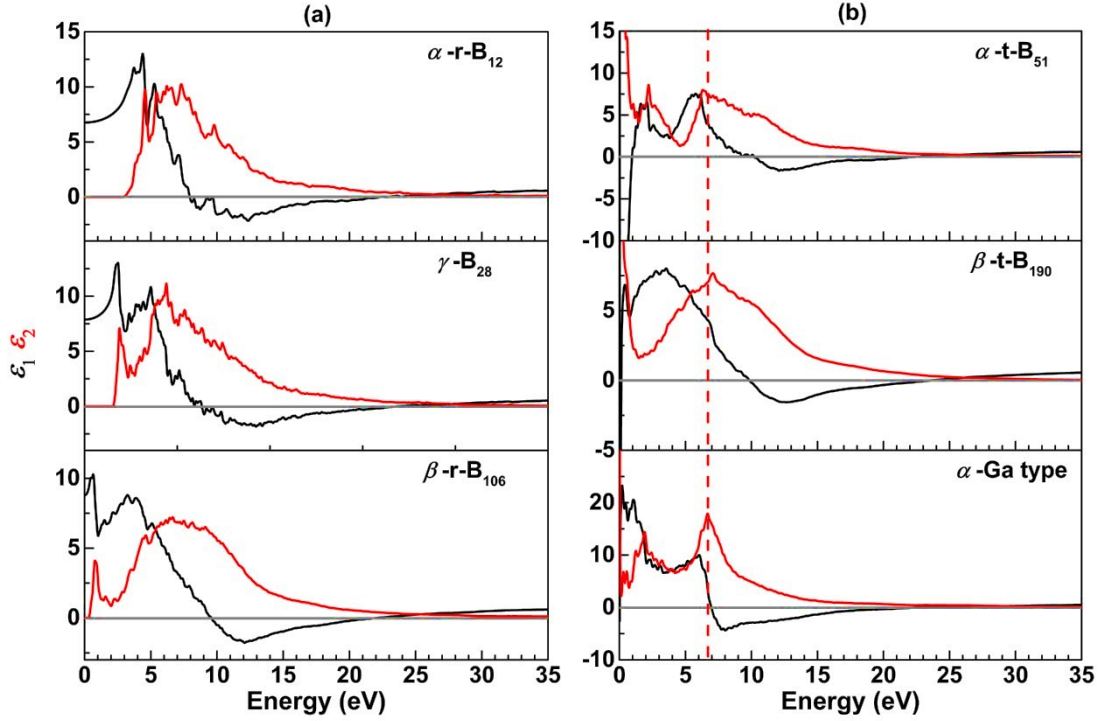


Fig. 20 Calculated real (ϵ_1 black) and imaginary (ϵ_2 red) component of the complex dielectric functions of (a) semiconductors (α -r-B₁₂, γ -B₂₈, and β -r-B₁₀₆) and (b) metals (α -t-B₅₁, β -t-B₁₉₀, and α -Ga type boron).

to that of β -r-boron. Our calculation and analysis support their explanation. In general, our calculation agrees reasonably well with the experimental results.

The calculated dielectric functions for all six phases are plotted in Fig. 20. The $\epsilon_2(\omega)$ curves for α -r-B₁₂, γ -B₂₈, and β -r-B₁₀₆ each consist of a sharp pre-peak and a broad peak. The absorption thresholds for these three phases are 2.93, 2.11, and 0.27 eV, respectively. Particularly, the absorption threshold of γ -B₂₈ is very close to the experimental value¹⁰¹ 2.1 eV. The values of $\epsilon_1(0)$ (also known as the static dielectric constant ϵ_s) for these semiconductors are 6.77, 7.88, and 8.80, respectively. Across these semiconductors, the $\epsilon_1(0)$ value increases with the decreasing band gap. The same observations have also been made¹⁰⁵ for other semiconductors, such as Ge, Si, and diamond.

The shapes of the $\epsilon_2(\omega)$ curves for the metallic phases (α -t-B₅₁, β -t-B₁₉₀, and α -Ga) are apparently quite different from each other. The most interesting case is the α -Ga type boron. The distinct $\epsilon_2(\omega)$ curve of α -Ga type boron is the result of the existence of a pseudogap at the Fermi surface discussed earlier. Such a pseudogap greatly reduces the absorption near the Fermi surface so that the absorptions in the $\epsilon_2(\omega)$ curve reduces as the photon energy approaches zero. For α -t-B₅₁ and β -t-B₁₉₀, the apparent differences in their $\epsilon_2(\omega)$ curves can be attributed to their different electronic structures. Nevertheless, the $\epsilon_2(\omega)$ curves for α -t-B₅₁, β -t-B₁₉₀, and α -Ga type boron have dominant peaks at photon energies of 6.31, 7.08, and 6.68 eV, respectively, which are rather close to each other despite the fact that these phases have quite different $\epsilon_2(\omega)$ curves. However, the exact reason underlying this interesting phenomenon is not clear.

3.5 Conclusion

The structural, electronic, and spectroscopic properties of the six crystalline elemental boron phases have been studied via *ab initio* calculations. To the authors' knowledge, this is the first calculation of the properties of β -t-B₁₉₀ which has a very complex crystal structure. It is shown that the ico-PDOS for α -r-B₁₂, γ -B₂₈, α -t-B₅₁, β -r-B₁₀₆, and β -t-B₁₉₀ have common features implying a correlation between the geometrical icosahedral structures and the calculated DOS. Our main result is a comprehensive study of the XANES spectra in the elemental boron phases. Using the characteristic XANES features of the perfect icosahedron as a baseline, it was concluded that there are three characteristic peak features for icosahedral clusters in the five icosahedron-containing elemental boron phases in the energy range from 190 to 215 eV. Our spectral calculations

also include the interband optical properties in these six elemental boron phases with reasonable agreements with experimental data on α -r-B₁₂ and β -r-boron.

CHAPTER 4

ELECTRONIC STRUCTURE AND SPECTROSCOPIC PROPERTIES OF BORON-RICH COMPOUNDS

4.1 Introduction

Boron carbide (B_4C) is the most well studied phase among the many types of boron compounds. It is believed to be one of the hardest materials known¹⁰⁶. However, boron carbide is not always stoichiometric and the C content can vary from 8 to 20%¹⁰⁷. There is growing evidence that many of the boron carbides are amorphous with a composition closer to B_5C ^{39,89,108}. They may also contain fragments of carborane or borane and are heavily saturated with H^{109,110}. Boron carbides also tend to contain layered amorphous-like microstructures within the crystalline B_4C ^{38,111–113} that are similar to intergranular glassy films in polycrystalline ceramics such as silicon nitride or silicon carbide. Thus, boron carbide should be considered as a class of boron rich compounds with highly complex structures and compositions that could influence their specific applications, and make their proper characterization a difficult task. Nevertheless, study of boron carbide has to start with the ideal stoichiometric B_4C phase. It is now well accepted that the structure of B_4C consists of a 12 atom icosahedron interconnected with a three carbon atom chain along the rhombohedral body diagonal [see Fig. 21(c)]. However, the exact locations of the three C are somewhat controversial because it is experimentally difficult to distinguish B from C due to their similar scattering cross-section. Lazzari *et al.* compared theoretical infrared and Raman spectra of different models with corresponding experimental spectra¹¹⁴ and concluded that the preferable structure is the one with C at a polar site along with a CBC chain (denoted as $B_{11}C$ -CBC). This result has been confirmed in various works (including

the present work) by comparing the total ground state energies of different structures obtained through highly accurate *ab initio* calculations. There are also studies on alternative structures such as $B_{13}C_2$ ^{115,116} and $B_{12}C_3$ ¹¹⁷.

There exist numerous other boron compounds with the B_{12} icosahedra as the main structural unit such as $B_{12}Si_2$, $B_{12}P_2$, $B_{12}As_2$, $B_{12}O_2$, etc.¹¹⁸. These compounds can also be doped with alkali or rare-earth elements^{119–123} to give additional compositional and structural variations and some of them may even result in superconductivity^{49,50}. Among them, boron suboxide ($B_{12}O_2$ or B_6O) has received great attention in recent years because of a combination of several favorable properties. It is a semiconducting optical material but is also one of the hardest substances known^{124–127}. One of the main problems is that $B_{12}O_2$ samples are always O deficient with compositions that can vary over a considerable range of O content. Wang *et al.*¹²⁶ argued that when $B_{12}O_2$ is released from high pressure it suffers structural instability indicating a critical weakness of this compound under dynamic impacts and concentrations of high stress. The structure of stoichiometric $B_{12}O_2$ is less controversial than B_4C and it is generally accepted that the two O atoms bond to the icosahedral B_{equat} but have little direct O-O interaction (See Fig. 21(d)).

Real samples of B and B-rich compounds tend to have quite complex structures that contain various types of defects which make large single crystals mostly unavailable for physical properties measurements. However, it is reasonable to consider stoichiometric α -r- B_{12} , B_4C , and $B_{12}O_2$ as the three most representative crystals that contain B_{12} icosahedra and have similar rhombohedral structure. In this work, I present the results of detailed calculations on these three crystals covering their physical properties including electronic, optical, and spectroscopic properties. There are numerous articles reporting the

structures and physical properties of these three compounds but most of them concentrate on one or two structures or on a particular aspect of their properties. A careful, detailed, and comparative study of these three crystals' properties will yield additional insights into the structure/property relationships present in B and B-rich compounds. Because of the structural variations in these three crystals and the associated differences in inter-icosahedral and intra-icosahedral bonding, studying them all simultaneously brings out new physics and insights that often escape attention in the single phase studies. In section 4.2, the structures of these three crystals are briefly described section 4.3 (electronic structures and optical properties) and 4.4 (XANES spectra and the applications of XANES spectra of icosahedra in $B_{11}C$ -CBC and $B_{12}O_2$). The main results are presented in section 4.5 with detailed discussions being presented in subsections. The conclusion will be presented in section V together with suggestions for further studies.

4.2 Crystal Structure and Structure Modeling

The structure of the three crystals (α -r- B_{12} , B_4C , and $B_{12}O_2$) are described briefly although α -r- B_{12} has been introduced in CHAPTER 3. They all have a rhombohedral structure with space group R-3m (No.166)^{118,128}. The most unique feature is that all three crystals contain molecule like icosahedral clusters. α - B_{12} has a relatively simple structure consisting of icosahedral B_{12} units in a rhombohedral cell characterized by two nonequivalent sites named polar (B_{polar}) and equatorial (B_{equat}) bound together in a cohesive unit (see Fig. 21(a) and 1(b)). The inter-icosahedral bonds come in two varieties. The B_{polar} form two-center two-electron (2c-2e) bonds with the B_{polar} of neighboring icosahedra while the B_{equat} participate in planar three-center two-electron (3c-2e) bonds with the B_{equat} of

neighboring icosahedra. The inter-icosahedral 3c-2e bonds are all in the a-b plane of the hexagonal cell. In the icosahedra of α -r-B₁₂ and B₁₂O₂ there are strictly two types of B sites, B_{polar} and B_{equat}, whereas in B₄C the symmetry is greatly reduced because of the presence of one C in a B_{polar} site. However, to a first order of approximation we can still make the same initial assignment. In all cases each B_{polar} participates in intra-icosahedral bonding to five nearest neighbors (NN) and inter-icosahedral bonding to one B_{polar} of a neighboring icosahedron. For α -r-B₁₂, the B_{equat} have five similar NN intra-icosahedral bondings but also participate in 3c-2e bonds to the B_{equat} of neighboring icosahedra⁹⁵. This is modified for B₁₂O₂ by the presence of an O near the center of the B_{equat} 3c-2e inter-icosahedral bonds. B₄C is more complicated because it is difficult to precisely identify the positions of C as previously mentioned in the introduction. To a first order approximation one B_{polar} is substituted by a C and a CBC chain exists in the crystal cell with the C endpoints assuming similar positions to the O in B₁₂O₂. In the present study, the experimentally reported structures were used as initial structures that were then optimized with the Vienna *ab-initio* simulation package (VASP)^{16,17,129}.

The arrangement of C and B atoms for B₄C described above is difficult to obtain experimentally. It is believed that at least two of the C atoms are in the chain. We used a theoretical approach to identify the most probable configuration by starting with a simpler structure of having three C atoms in the chain. Four additional models with different C locations were then constructed. They are labeled respectively as B₁₁C_p-CBC, B₁₁C_p-BCC, B₁₁C_e-CBC, and B₁₁C_e-BCC. The first part of the label is for atoms in the icosahedron and the second part is for the three atom chain. The choice of C_p or C_e indicates that the carbon substitutes for a polar or equatorial B. The displaced B atom is placed at the center of the

chain for the CBC configurations and at an endpoint for BCC. The structures of all five models were fully relaxed using VASP and the resulting total energies are listed in Table 3. It can be seen that $B_{11}C_p$ -CBC has the lowest energy consistent with the conclusions of previous studies^{114,130,131}. $B_{11}C_p$ -BCC and $B_{11}C_e$ -BCC all have much higher energy and are unlikely to exist. From now on the B_4C structure we refer to is the $B_{11}C_p$ -CBC structure unless otherwise stated.

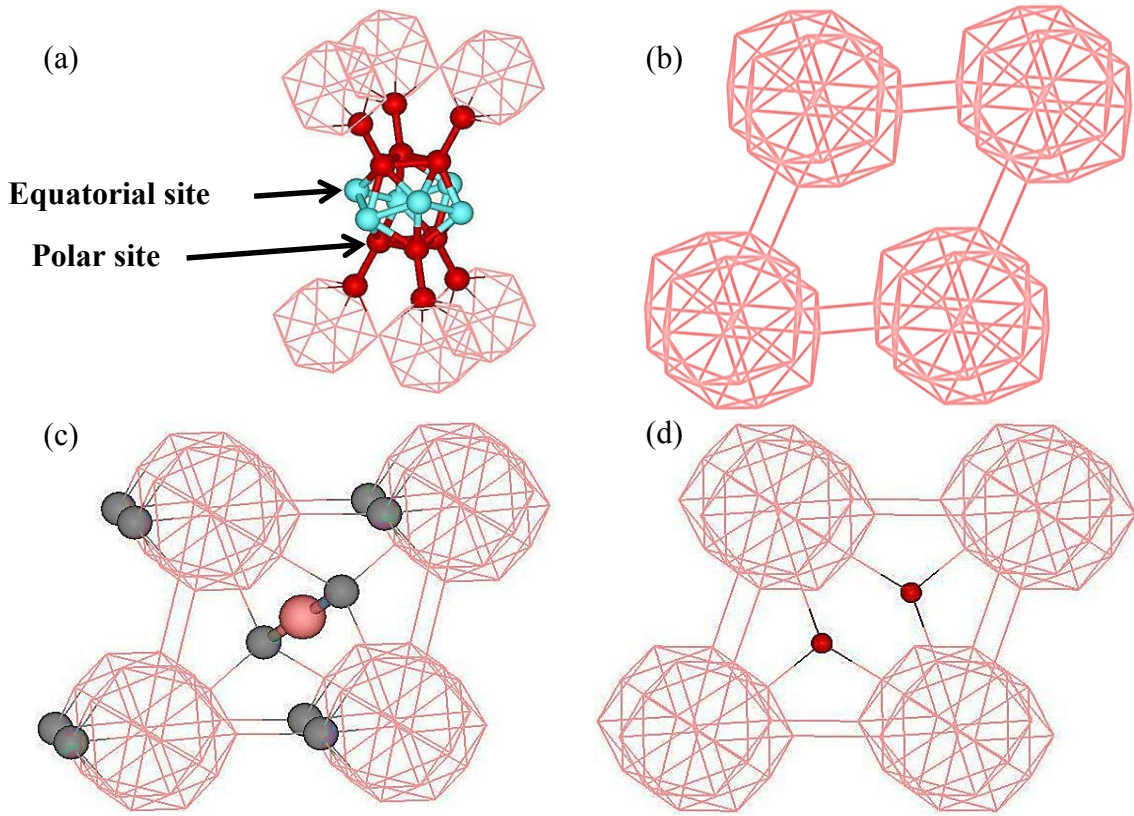


Fig. 21 (a) Scheme for polar and equatorial site in α -r- B_{12} ; crystal structure of (b) α -r- B_{12} , (c) $B_{11}C$ -CBC, (d) $B_{12}O_2$.

The structural data of these three crystals are listed in Table 4 and depicted in Fig. 21. Each B_{polar} atom has five intra-icosahedral bonds and one shorter inter-icosahedral bond. This is the main argument that these crystals are inverted molecular solids^{132,133}. Each B_{equat} atom in α -r- B_{12} has five intra-icosahedral bonds and participates in a three center inter-

icosahedral bond. In B_4C and $B_{12}O_2$, the B_{equat} also has one short bond with an atom at the endpoint of the chain or O instead of the three center inter-icosahedral bond. The key difference in these three crystals is the presence of a 3-atom chain along the rhombohedral body diagonal in B_4C and two O atoms in $B_{12}O_2$. This leads to the general observation that the $B_{\text{polar}}-B_{\text{polar}}$, $B_{\text{equat}}-B_{\text{equat}}$ and $B_{\text{polar}}-B_{\text{equat}}$ bond lengths (BLs) in α - r - B_{12} and $B_{12}O_2$ are comparable; both are shorter than that in B_4C . In B_4C , the middle B atom in the C-B-C chain has two short bonds of only 1.429 Å. In $B_{12}O_2$ the two O atoms are not in the form of a “chain” since they are well separated at 3.01 Å and are not consider to be bonded. The O- B_{equat} BL is also relatively short (1.493 Å). Both O atoms in $B_{12}O_2$ and the end C atoms in the chain in B_4C are bonded with three B_{equat} atoms in three neighboring icosahedra. The different bonding configurations result in the different electronic structure and optical properties in these crystals.

Table 3 Relaxation summary of five different configurations of boron carbide B₄C.

System	Configurations	Total Energy eV
B ₁₂ -CCC	All three C atoms in the chain.	-121.111
B ₁₁ C _p -CBC	One C at polar site other two in the chain with B at the middle.	-122.301
B ₁₁ C _e -CBC	One C at equatorial site, other two in the chain with B at the middle.	-121.767
B ₁₁ C _p -BCC	One C at polar site, other two in the chain with B atom at the end of the chain.	-102.986
B ₁₁ C _e -BCC	One C at equatorial site, other two in the chain with B atom at the end of the chain.	-107.524

Table 4 Crystals structure parameters of α -r-B₁₂, B₄C, and B₁₂O₂. Bond lengths are in Å.

Crystal	α -r-B ₁₂	B ₄ C	B ₁₂ O ₂
a(Å)	4.9888	5.1651	5.1346
α (°)	58.063°	65.705°	63.164°
Atoms/cell	12	15	14
Different atomic sites	2	4	3
B _p -B _p	1.656*, 1.725(2)	1.715*, 1.809(2)	1.691*,1.778(2)
B _p -B _e	1.778(2), 1.770	1.787, 1.802(2)	1.777(2), 1.808
B _e -B _e	1.760(2)	1.762 (2)	1.751(2)
B _p -C _p	-	1.715*, 1.809(2)	-
B _e -C _p	-	1.787, 1.802(2)	-
B _e -C _c	-	1.606	-
B _c -C _c	-	1.429	-
B _e -O	-	-	1.493
O-O separation	-	-	3.01

* Inter-icosahedral bonds; p=polar; e=equatorial; and c=chain.

4.3 Electronic Structure and Optical Properties

The electronic structure and bonding of elemental B and B-rich compounds have been extensively studied for more than 20 years both experimentally and theoretically^{66,83,100,117,134–138}. Extensive calculations using plane wave pseudopotential method have been done by Lee and coworkers^{100,117,136,137}. Li et al. used the same OLCAO method as in the present work to study the band structure and optical properties of elemental B, B₄C, and B₁₂O₂ using experimentally determined crystal structures more than 15 years ago^{115,139–141}. The present work is a logical extension of the earlier work with much higher precision and has used the VASP optimized structures instead of the experimentally reported structures for the three crystals along with a more detailed analysis. Other relevant work related to the electronic structure and spectroscopic properties includes that of Fujimori et al.⁹⁴ who measured distributions of electron density in α -r-B₁₂ using synchrotron radiation; Zhao et al.¹³⁸ who studied changes in band structure of α -B₁₂ with pressure and found that at high pressure (around 160 GPa) α -B₁₂ becomes metallic. XANES/ELNES spectroscopic data on these B and B-rich compounds have been measured by several groups^{103,142,143}

Fig. 22 and shows the calculated band structures of α -r-B₁₂, B₄C, and B₁₂O₂ crystals which are quite different from one another especially in the valence band (VB) region. They are all semiconductors with indirect band gaps of 2.61, 2.97, 2.94 eV and direct band gaps at the Γ -point of 3.30, 5.04, and 5.44 eV for α -r-B₁₂, B₄C, and B₁₂O₂ respectively. The actual band gap values may be somewhat larger than the calculated ones since LDA generally underestimates the band gap. These calculated band gaps are consistent with other recent calculations. We also note that the width of the upper VB in α -r-B₁₂ (9.97 eV)

is larger than that of B_4C (9.05 eV), and that both are much smaller than that of $B_{12}O_2$ (12.32 eV). We are unable to locate precisely quoted gap values in these crystals. The reason is quite obvious. As stated in the introduction, these crystals are mostly defective except for α -r- B_{12} which is not easy to fabricate in large single crystals. B_4C could have a large variations in C content and may even be amorphous and $B_{12}O_2$ has many defects such as O vacancy. Hence our calculated band gap values or other band structure characteristics are understood to be that of stoichiometric perfect crystals and used as guidelines for comparisons with any measured values which could vary over a wide range.

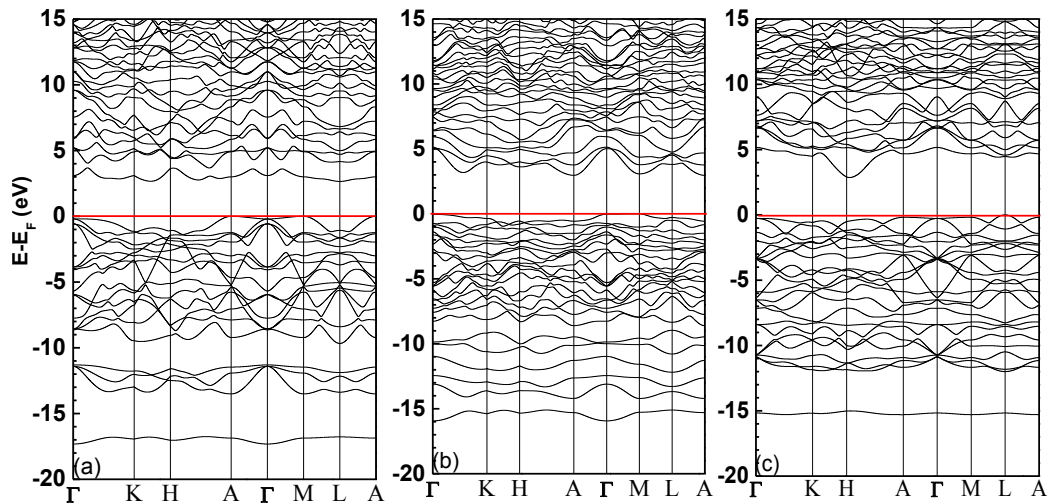


Fig. 22 Calculated band structures of: (a) α -r- B_{12} , (b) B_4C , and (c) $B_{12}O_2$ (The red line denotes the Fermi level).

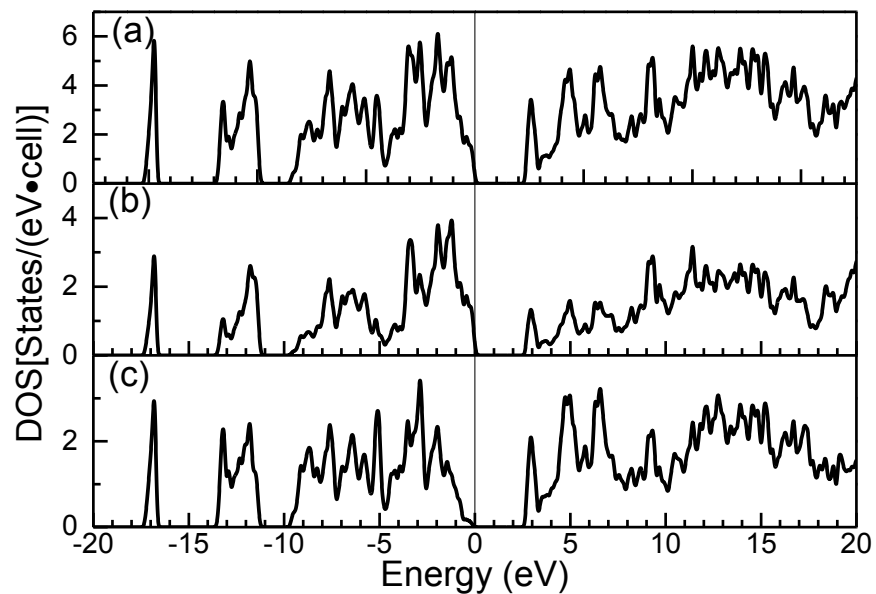


Fig. 23 Calculated total DOS and PDOS of α -r-B₁₂. (a) Total; (b) B_{polar}; (c) B_{equat}.

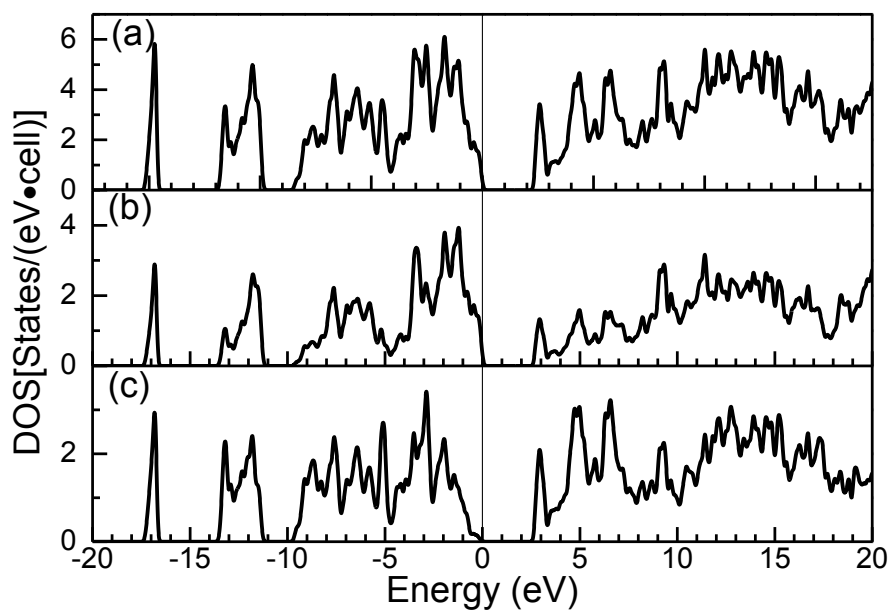


Fig. 24 Calculated total DOS and PDOS of B₁₂O₂. (a) Total; (b) B_{polar}; (c) B_{equat}; (d) O.

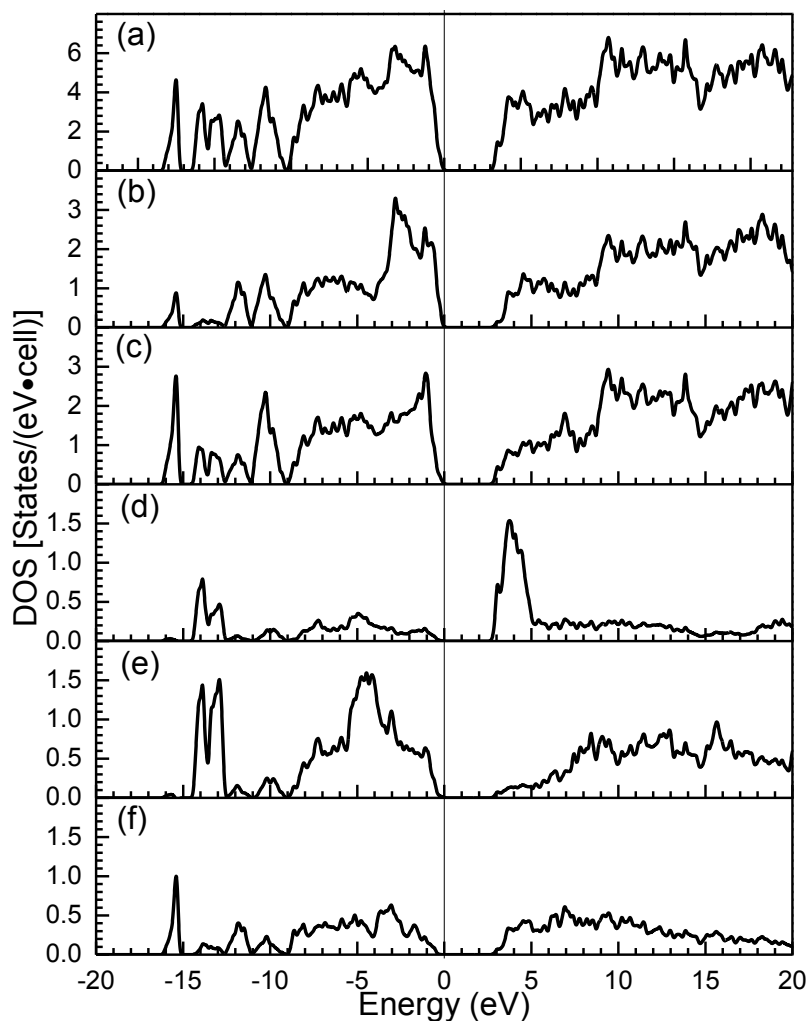


Fig. 25 Calculated total DOS and PDOS of B_4C . (a) Total; (b) B_{polar} ; (c) B_{equat} ; (d) B in the chain; (e) C in the center of the chain; (f) C in the icosahedron at the polar site.

The calculated total DOS (TDOS) and atom-resolved partial DOS (PDOS) for α - r - B_{12} , B_4C , and $B_{12}O_2$ are shown in Fig. 23, Fig. 24, and Fig. 25 respectively showing very different features. In α - B_{12} , the VB consists of three segments, the two lower segments (peak at -16.9 eV, and band from -13.3 to -11.8 eV) are similar for B_{polar} and B_{equat} but they are quite different for the upper segment (-9.9 to 0 eV) which involves the B $2p$ orbitals in the three center bond. The top of the VB consists of states mostly from B_{polar} . In the CB

region, the TDOS has highly pronounced peaks below 10 eV which will be reflected in the XANES spectrum to be discussed below. The lower part of the CB is mostly dominated by B_{equat} and the upper part by B_{polar} whereas the middle part has almost equal contribution from both sites.

The TDOS in the VB region of B_4C (shown in Fig. 24) is quite different from that (shown in Fig. 23) of $\alpha\text{-r-}B_{12}$. The lower and upper segments are not well separated. The lower part of the TDOS has multiple peaks while the upper part is quite broadened. These differences come from the presence of the C-B-C chain atoms. The two C atoms in the chain have significant contributions in the middle region of the lower VB and the middle part of the upper VB. In the CB region of B_4C , B_{equat} and B_{polar} have similar CB DOS features and the central B in the C-B-C chain dominates the lower part of the CB which will again be reflected in the XANES/ELNES spectral features.

In $B_{12}O_2$ the lower VB TDOS (shown in Fig. 25) has two highly pronounced peaks. The peak at -21.9 eV is from O 2s which interacts with B_{equat} . The other peak at -15.2 eV is from B_{equat} and B_{polar} similar to that in $\alpha\text{-}B_{12}$. In the upper VB region, the TDOS has several well defined peaks with the lower portion from O 2p orbitals and the upper portion from B 2p orbitals. In the CB region below 10 eV, there are no prominent peaks as in $\alpha\text{-}B_{12}$ due to the presence of the O ions. Above 10 eV, the DOS is similar to that of $\alpha\text{-r-}B_{12}$. Such differences in the CB DOS will be clearly reflected in very different XANES/ELNES spectra to be discussed below.

The interband optical transition spectra of $\alpha\text{-r-}B_{12}$, B_4C , and $B_{12}O_2$ crystals were also calculated using the OLCAO method. Such calculations have become quite common and the computational procedures will not be detailed here because they have been

described in many other papers^{23,85,144-146}. Basically, the electronic structure is calculated using an extended basis set with the fully converged potential at a large number of k points within the BZ. The dipole matrix elements of transition from the VB states to the CB states are evaluated and the transition rate (or the imaginary part of the dielectric function $\epsilon_2(\hbar\omega)$) is calculated within the random phase approximation by summation over the BZ up to a high photon energy of about 35 eV. The real part of the dielectric function $\epsilon_1(\hbar\omega)$ is obtained from $\epsilon_2(\hbar\omega)$ by Kramers-Kronig conversion. The calculated results in the form of the complex dielectric functions for the three crystals are shown in Fig. 10. All three crystals have multiple sharp absorption peaks within the first 8 eV from the edge on-set, reflecting the complex peak structures of the crystals in both the VB and the CB. These results are close to those obtained before using the same method^{99,115,139} except that the precision is now much improved. There are many peaks structures in the $\epsilon_2(\hbar\omega)$ of all three crystals. However the centroids of the main absorption peaks in these three crystals all lie within the range of 6.6 eV to 7.1 eV, indicating that the overall absorption spectra are controlled by the icosahedral B units. We have also resolved the optical transitions into axial (aligned along the c-axis of the hexagonal cell) and planar components (perpendicular to the axial direction). The results are shown in Fig. 11. As can be seen, there is considerable optical anisotropy in all three crystal that can be attributed to bonding differences between icosahedra in the axial and planar directions. In all three crystals, the icosahedra are relatively isotropic but they bond primarily through standard 2 center covalent bonds in the axial direction and through various mechanisms in the planar direction. This results in different electron states and optical components in the two directions. In α -B₁₂ the planar bonding is in the form of 3c-2e inter-icosahedral bonds,

while for the other two crystals the three B atoms have either a C or an O near the center of the original triangular formation of B atoms. The C and O are both located slightly off the plane of the triangle due to steric constraints which makes isolating the effect to the axial or planar spectra somewhat difficult. In B_4C , the situation is further complicated by the alignment of the C-B-C chain with the hexagonal cell's c-axis. All these factors contributed to the optical anisotropy in these three crystals. The refractive index n of the

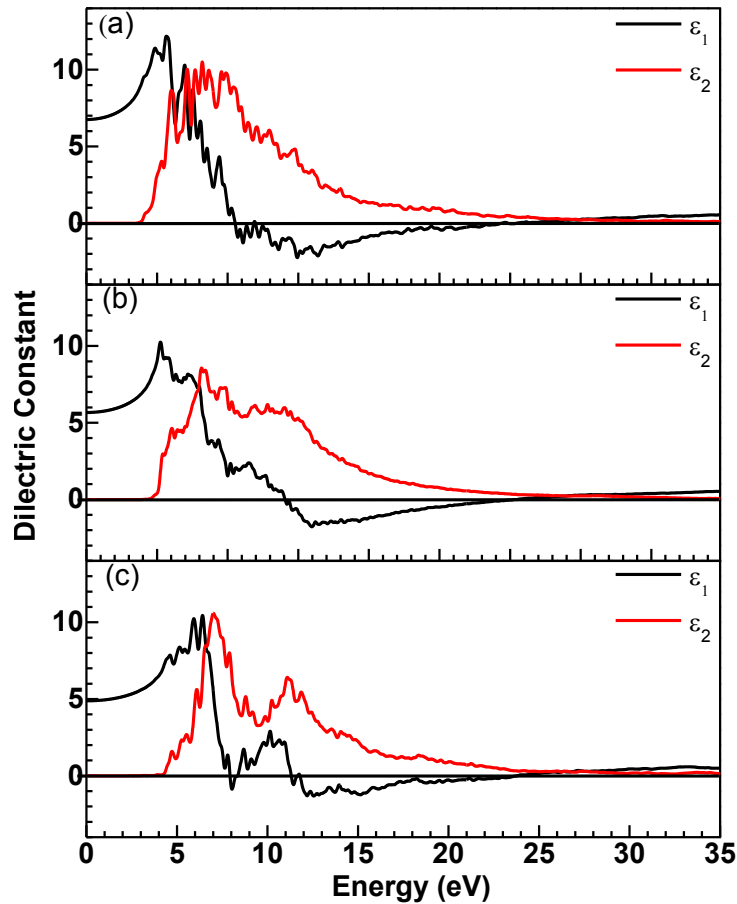


Fig. 26 Calculated directionally averaged real and imaginary of the optical dielectric function of: (a) α -r- B_{12} , (b) B_4C , and (c) $B_{12}O_2$.

crystal can be obtained as the square root of the static dielectric constant $\epsilon_1(0)$ (averaged over the three components). The estimated reflective index for α - B_{12} , B_4C , and $B_{12}O_2$ are

2.60, 2.56, and 2.21 respectively. We are not aware of any measured data on stoichiometric single crystal samples or other calculations on the optical properties of these three crystals.

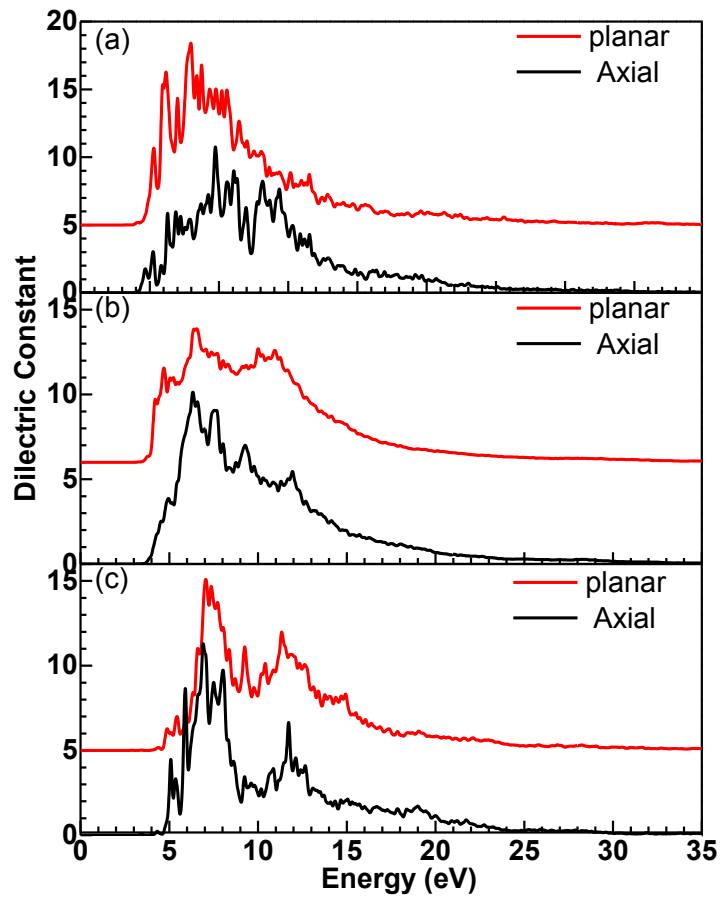


Fig. 27 Comparison of the axial and planar components of the imaginary part of the optical dielectric function in: (a) α -r-B₁₂, (b) B₄C, and (c) B₁₂O₂.

4.4 XANES/ELNES Spectra

In section 3.3.3 of CHAPTER 3, the XANES spectra of α -r-B₁₂ has been introduced associated with the other phases. In this chapter, the results achieved from section 3.3 will be applied to observe these boron-rich compounds. First, the XANES of α -r-B₁₂, B₁₁C-CBC, and B₁₂O₂ will be compared to learn themselves, then the results in Chapter 3 will be used to analyze the XANES spectra of boron-rich compounds.

4.4.1 XANES Spectra of α -r-B₁₂, B₁₁C-CBC, and B₁₂O₂

The B-K edge for α -r-B₁₂ has been shown in Section 3.3.1. To keep consistence in this chapter, it is briefly discussed again with decomposed XANES spectra shown in Fig. 28 which was briefly mentioned in a recent paper for comparison with the γ -B₂₈ phase spectra¹²⁰. The total spectrum (top panel) is the weighted sum of the spectra of B_{polar} and B_{equat} in equal proportions. They are quite different because of different bonding environments. B_{polar}-K has more peak features than B_{equat}-K. It is also noted that the edge on-set of B_{polar}-K is at a lower energy. In Fig. 28, we use the same labels for the peaks in the individual spectra as in the total spectrum so as to show which one contributes to which. The shoulder peak A at the edge (192.9 eV) comes from B_{polar}-K. Peak B (194.2 eV) has contributions from both B_{polar}-K and B_{equat}-K whereas peak C (195.4 eV) is unquestionably from B_{equat}-K. At intermediate energies, At the same energy value (~197 eV), peak D (only shown in the XANES of polar sites) and a valley (observed in the XANES of equatorial sites) make the total peak less prominent. Peak E in the total XANES is the average value since the energy values for peak E' (polar B-K) and E'' (equatorial B-K) are different. Peak F (201.0 eV) is mostly from B_{polar}-K and peak G (202.4 eV) is mostly from B_{equat}-K. At the higher energy range, peaks H, I, and J are identified in the total spectrum. The relatively

prominent peak J is exclusively from B_{polar}-K. In Fig. 15 (Section 3.3.1 page 48), we have compared the calculated XANES/ELNES spectrum of α -r-B₁₂ with the corresponding experimental spectrum¹⁰⁸. Our calculation has reproduced all peak features present in the experimental spectrum. This is achieved only if we take the total spectrum to be the weighted sum of different spectra from individual nonequivalent sites.

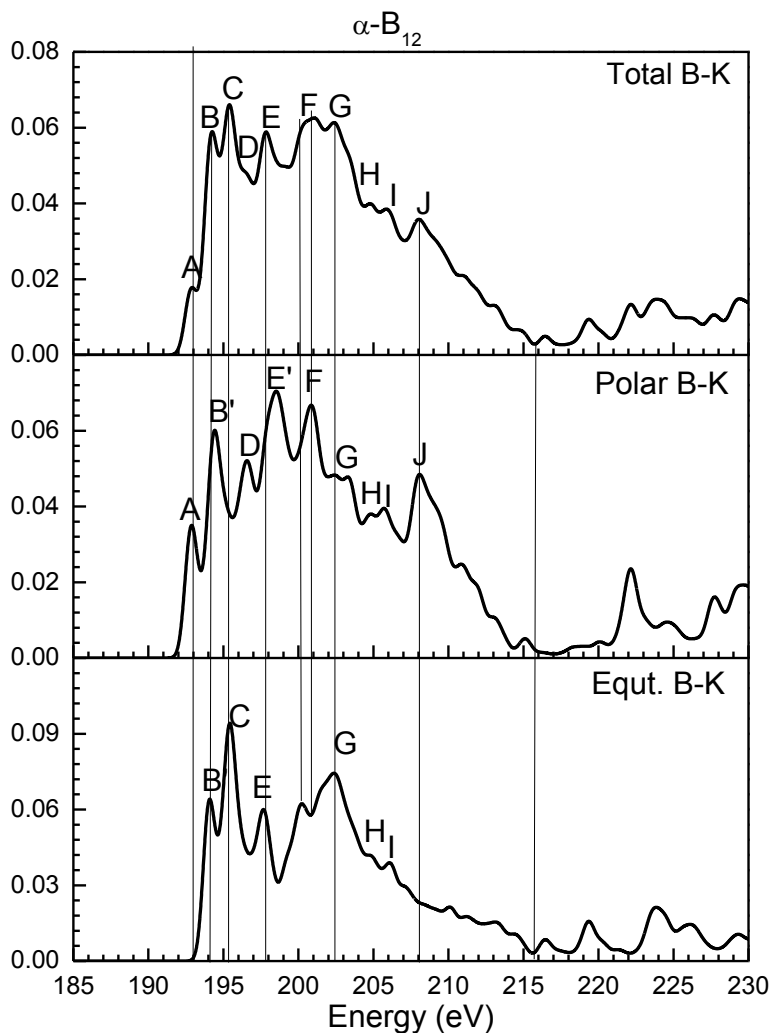


Fig. 28 Calculated B-K edge in α -B₁₂. Top panel is total weighted sum of individual spectra from polar and equatorial B atoms (lower panels).

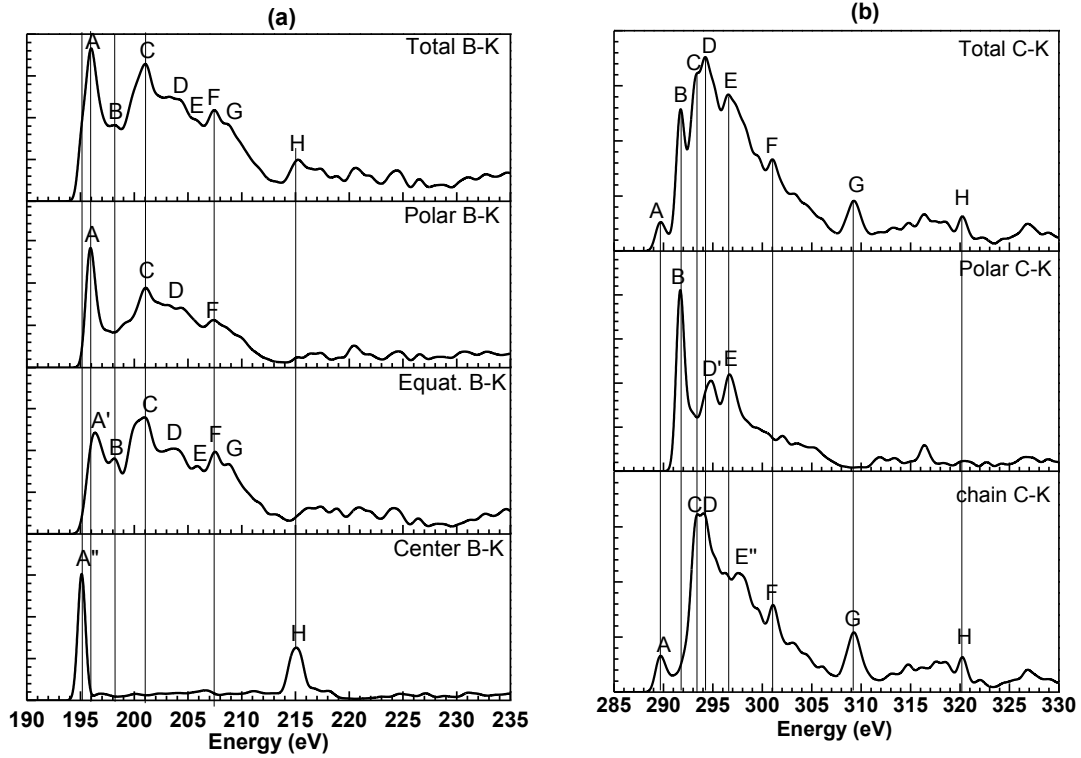


Fig. 29 Calculated (a) B-K edge and (b) C-K edge in $B_{11}C$ -CBC. For both figures, the top two panels individually show total K-edge, the rest panels show the K-edge for different sites.

The calculated B-K and C-K edges at different sites for B_4C are shown in Fig. 29 (a) and (b). As in the α - r - B_{12} case, spectra for individual sites have very different features especially for the B atom in the middle of the three atom chain. The peak A (196.0 eV) in the total spectrum is also the most pronounced peak and is the combined contribution from all three B sites. The minor peaks B (198.2 eV) and E are both from the $B_{\text{equat-K}}$. Another prominent peak C (201.1 eV) is almost equally contributed by $B_{\text{polar-K}}$ and $B_{\text{equat-K}}$. Similarly, peak F (207.5 eV) is shaped by both B_{polar} and B_{equat} . Peak H (215.3 eV) at a higher energy is exclusively from the B atom in the C-B-C chain. We can also identify

some minor peaks D and G which have contributions from both B_{polar} and B_{equat} . The K-edge spectrum of the chain boron has only two peaks, A'' and H. A'' contributes to the broadening of A in the total spectrum and H is the well pronounced peak H at higher energy. These spectroscopic features in the total spectrum are radically different from those of B_{polar} and B_{equat} because of their entirely different local geometries. The spectra of the K-edges for the polar and chain C atoms [Fig. 29 (b)] also have very different features because of the different local bonding configurations. As a matter of fact, the $C_{\text{polar}}\text{-K}$ more closely resembles the $B_{\text{polar}}\text{-K}$ than the chain C-K edge spectrum. This seems to imply that the local bonding geometry is more important than the difference of one valence electron between B and C. Such new findings were never been anticipated or discussed before. The total C-K spectrum has a main peak D (294.2 eV) which is almost equally contributed to from both C sites. There are some less prominent shoulder-like peaks on both sides of peak D. As can be clearly seen, the edge peak A (289.7 eV) is from the chain C whereas the sharp peak B (291.8 eV) is from polar C. The well-produced peaks G (309.3 eV) and H (321.0 eV) at the higher energy are exclusively from the chain C-K. In Fig. 30(a) and (b), we compare the calculated B-K and C-K with the corresponding experimental spectra in B_4C ^{108, 109}. In the B-K comparison, the edge peak A which is also the most pronounced peak is used to align the energy scale by shifting the calculated spectrum 4.47 eV. The agreement is very satisfactory. The calculated spectrum has reproduced all the peak features present in the experiment. The calculated total B-K spectrum in B_4C is also in good agreement with the XANES spectra obtained by Li *et al.* ¹¹⁹. In the case of the C-K edge in B_4C (Fig. 30 (b)), it is clearly shown that the calculated spectrum is the sum of two different C sites and has a much richer spectrum than either the measured ELNES data ¹⁰⁹ or the x-ray absorption

data of Jiménes *et al.*¹¹⁰ on polycrystalline samples. Both experimental data have limited resolution, but their general shapes are similar and are in reasonably good agreement with the calculation. In these comparisons, we have to contend that some of the disagreement could be rooted in the different samples of boron carbide used and the limited instrumental resolution available at the time for both experimental techniques, especially in the higher energy range where the background absorption could mask some spectral features.

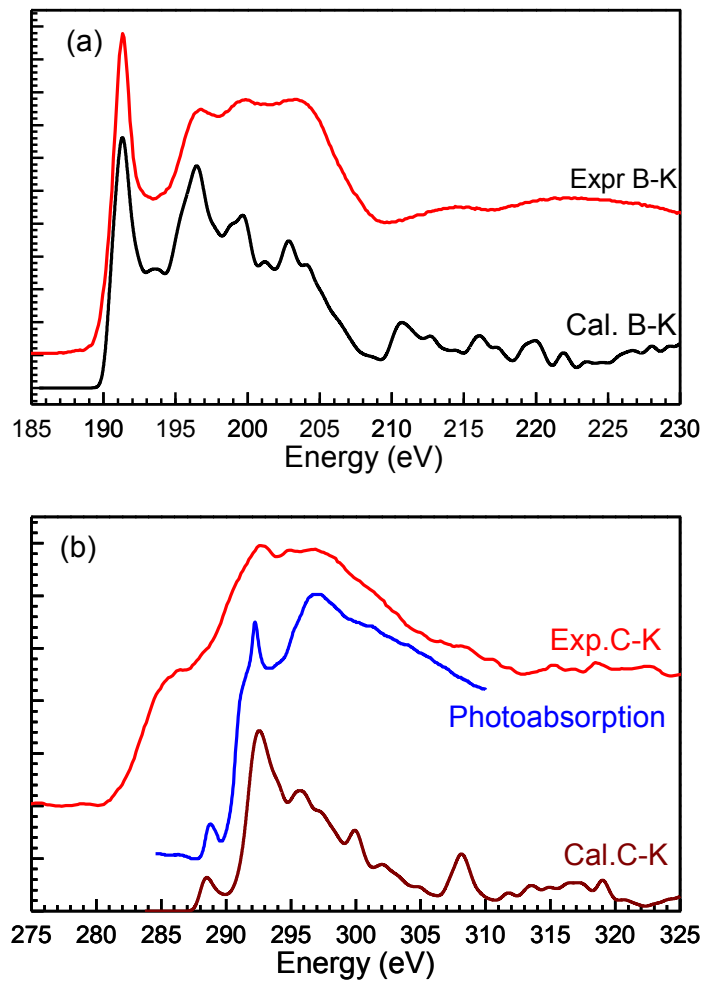


Fig. 30 Comparison between the calculated and the measured ELNES spectra in B_4C : (a) B-K; The calculated spectrum is shifted by 4.47 eV to align the main peak with experiment¹⁰⁸; (b) C-K. The calculated spectrum is shifted by 4.50 eV to align the main peak with experiment (ref.¹⁰⁹, top,¹¹⁰, middle.).

The calculated B-K edge spectra of $B_{12}O_2$ are shown in Fig. 31. Interestingly, B_{polar} and B_{equat} have rather similar peak features but with different edge on-sets. This shift in energy on-set between polar and equatorial sites results in more peak features in the total B-K spectrum. The prominent peak A (196.5 eV) at the edge on-set and other two peaks D (201.5 eV) and F (207.6 eV) in the total are from the related peaks in the B_{polar} -K spectrum whereas the main peak B (198.2 eV), peak E (203.0 eV), and peak G (209.6 eV) are from the B_{equat} -K spectrum.

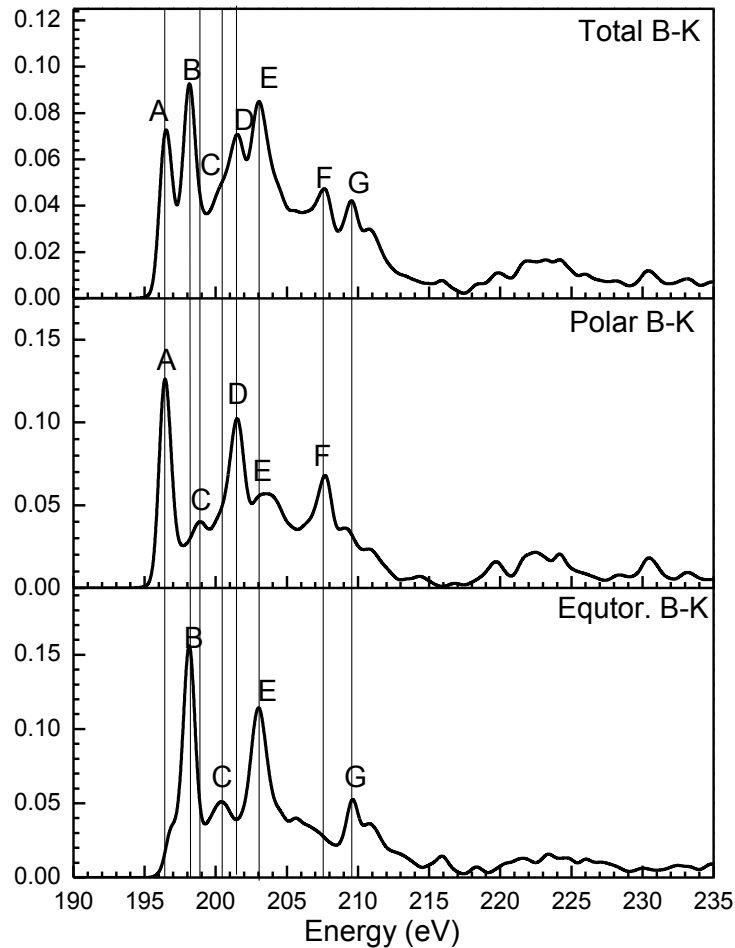


Fig. 31 Calculated B-K edge in $B_{12}O_2$. Top panel is the weighted sum and the lower panels are the spectra from polar and equatorial B sites.

In Fig. 32 (a) and (b), we compare the calculated B-K and O-K spectra in $B_{12}O_2$ with the corresponding experimental spectrum ¹⁰⁸. As can be seen, all the peak features in the B-K edge present in the measured spectrum are reproduced by the calculation. Not only peak positions but also the overall shape of the spectrum is in good agreement. Thus, we can identify that some peaks, such as A, D, F, comes from polar boron sites, and some peaks, such as B, C, E, dominantly originate from equatorial boron sites. The rest peaks are averaged by the signal from two sites so that it is hard to identify it. For the O-K edge, the calculated spectrum has a strong peak A and other well-resolved peaks at higher energy. Peak A is in good agreement with experiment, peak B is at a slightly higher energy whereas peak C in the calculated spectrum is somewhat less prominent but its relative position with B still matches with the experiment. The overall agreement seems satisfactory since the general spectral shape is similar even in the high energy range where the experimental resolution is limited. Some of the discrepancies can be attributed to the fact that the samples used in the experiment are not stoichiometric and may be O deficient ^{56, 93, 108}.

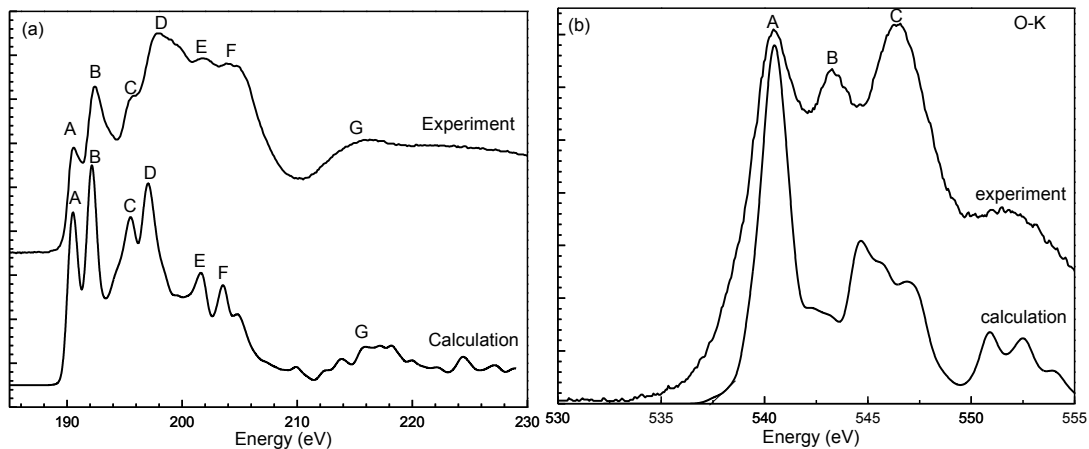


Fig. 32 Comparison of the calculated (total) and the measured B-K edge (a), and O-K edge (b). The calculated spectrum is shifted by 3.94 eV for B-K and 5.69 eV for O-K to align the main peaks with experiment.

To assess the overall features of the B-K edges in α -r-B₁₂, B₄C, and B₁₂O₂ crystals, we compare their total B-K spectra in Fig. 33. Obviously, they have very different peak features as well as energy on-sets. The energy on-set of the B-K edge in α -r-B₁₂ is significantly lower than that of the other two. The edge on-set in B-K in B₄C is slightly lower than that of B₁₂O₂. The B-K edge in α -r-B₁₂ has more peak features and a more broadened overall spectral shape than in the other two crystals in spite of the fact that α -B₁₂ is an elemental material. The fact that all the experimentally observed features of such complicated spectra can be reproduced so well is truly amazing and is a strong testament to the theory and techniques used in the supercell-OLCAO method for XANES/ELNES calculations. In ref. ¹²⁰ where the XANES/ELENES spectrum of γ -B₂₈ was compared with that of α -r-B₁₂, it was pointed out that there are resemblances in the spectral features of the B-K edges of B_{polar} and B_{equat} with similar sites in γ -B₂₈ in the icosahedral unit. Such similarities no longer exist in the present case with B₄C and B₁₂O₂. This underscores the importance of the presence of the chain atoms or O atoms in the crystal in modifying the spectral features of the B-K edge.

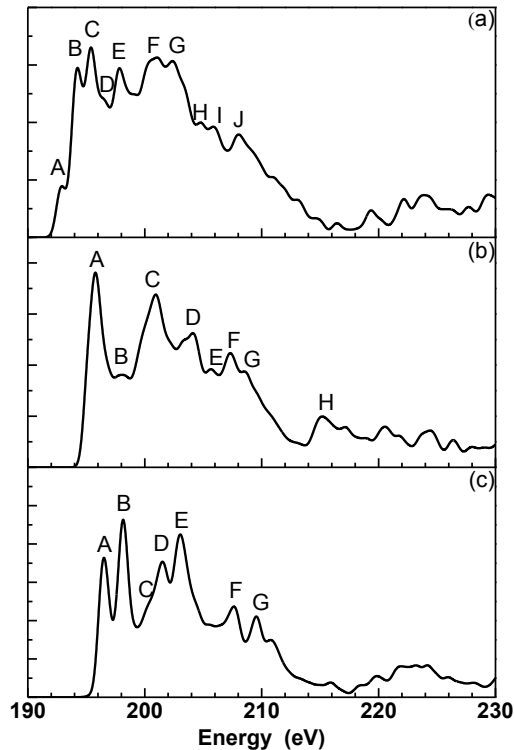


Fig. 33 Comparison of the calculated B-K spectra (total) of (a) α -r-B₁₂, (b) B₄C, and (c) B₁₂O₂.

4.4.2 Comparison of XANES Spectra for Elemental Boron and B₁₁C-CBC and B₁₂O₂

The characteristic XANES features of the icosahedra in crystalline elemental boron (shown in section 3.3) can be used as a reference when analyzing the XANES spectra of B₁₁C-CBC and B₁₂O₂. The B₁₁C-CBC model (whose structure was described in detail previously¹⁴⁷) can be essentially understood as a modification of the α -r-B₁₂ structure with a carbon-boron-carbon (CBC) chain along the body diagonal and a substitution of one icosahedral boron atom with a carbon atom. The XANES spectrum of the icosahedron in B₁₁C-CBC still retains the three-peak characteristic feature in the B-K edge features [see Fig. 34] in the same energy range (194~215 eV) as that for the crystalline elemental boron. The peak features for the modified icosahedron B₁₁C are relatively complex, but can still

be sorted into three groups: A (194~197 eV), B (197~206 eV), and C (206~214 eV), similar to those for α -r-B₁₂. Noticeably, the XANES spectrum of the B atom in the -CBC- chain [shown in Fig. 34] is entirely different from the other B-K edge spectra. It has two distinguishable peaks with the higher energy one clearly visible at ~215 eV in the total B-K edge of B₁₁C-CBC. The experimental observation of this absorption peak in clean and well characterized samples can be used as evidence of the presence of a boron atom in the chain. Unsurprisingly, the XANES spectrum of the carbon [shown in Fig. 29 (b)] in the modified icosahedron (C3 also polar C) with peaks at 292 and 295 eV is very different from those of the carbon in the -CBC- chain (C1 and C2). The main absorption peak at 292 eV in the total C-K edge is therefore identified as due to polar C.

For B₁₂O₂, Fig. 31 shows that the energy range for the dominant peaks of Ico-XANES (also total B-K since no non-icosahedral boron in the primitive cell) is in 195~215 eV which is a little smaller than the range for α -r-B₁₂ but the low limit is higher than that of α -r-B₁₂. Interestingly, the upper limits of energy range of α -r-B₁₂, B₁₁C-CBC, and B₁₂O₂ are almost same while the lower limits become higher in the same order. Based on the principle of XANES calculation using OLCAO, it implies that the energy gap between the core state and the bottom of the conduction band increases with the atomic number *Z* of foreign atoms increasing.

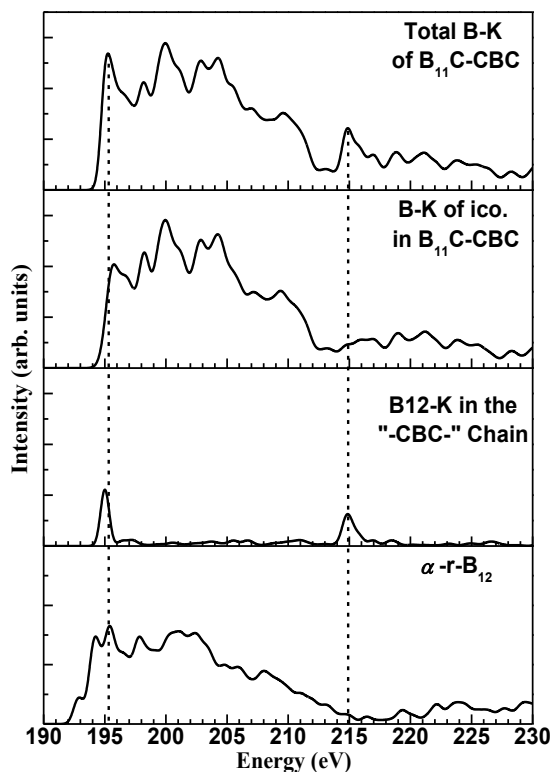


Fig. 34 Calculated XANES spectra of B-K of $B_{11}C-CBC$ and $\alpha-r-B_{12}$.

4.5 Conclusions

The electronic structures and spectroscopic properties of $\alpha-r-B_{12}$, $B_{11}C-CBC$, and $B_{12}O_2$ are studied and compared. $B_{11}C-CBC$ and $B_{12}O_2$ can be considered as modifications of $\alpha-r-B_{12}$ since they are both boron-rich compounds. The electronic structures of them all show that they are semiconductors with bond gap (indirect band gap) 2.68eV (3.30eV), 2.97eV (5.04eV), and 2.94eV (5.44eV), respectively. The dielectric functions also support the results of electronic structures.

The second equally important new physics is the remarkable agreement of the calculated and measured XANES/ELNES core level absorption spectra in these compounds which are exceedingly complicated. This is achieved only if all the B-K edges

for the crystallographically non-equivalent sites are calculated individually and their weighted sums are taken to compare with the experimental spectra. The site-specific spectra in these three crystals provide a much deeper understanding of the electronic structure of the B and B-rich compounds in relation to their bonding configurations. Such excellent agreement give credence to the supercell-OLCAO method used. Such calculations are far superior to the conventional approach of simply using the local DOS of the unoccupied states to explain the XANES/ELNES spectra. It is shown that the α -r-B₁₂ crystal with only one type of atom actually has more complicated spectral features than either B₁₁C-CBC or B₁₂O₂, defying common intuition because simpler crystal systems tend to have simpler spectra. The deviation may be related to the unique (3c,2e⁻) inter-icosahedral bonds present in α -r-B₁₂ but absent in the other crystal systems. This is further affected by the variations in energy on-set between the crystallographically nonequivalent B sites for each crystal. We also note that the similarity between the C_{polar}-K edge and B_{polar}-K edge in B₄C along with the distinct difference between the C_{polar} and C_{chain} K edge could be useful to help characterize various C concentrations in the boron carbides. The important implication is that the same theoretical technique can be applied to other more complicated phases of boron-rich compounds such as those under high pressure and temperature, containing microstructures and defects, in amorphous forms or mixed with borane or carborane molecular fragments. This will open the door to a more effective characterization of the samples used in laboratory measurements. As already alluded to in the introduction, the laboratory samples of boron and boron-rich compounds can be far more complicated because they contain various types of defects and other atomic species, intended or unintended.

Furthermore, the XANES research results of elemental boron are used to observe XANES spectra of boron-rich compounds. The ico-XANES spectra for all elemental boron and boron-rich compounds have three dominant characteristic peak groups which are in the energy range of 190-215 eV. For $B_{11}C$ -CBC having non-icosahedral boron sites, specific features may be identified comparing with ico-XANES spectra. The isolated non-icosahedron boron atoms can be identified if their XANES spectra have specific features which may be outside the energy range of the characteristic features of icosahedron or have rather stronger absorption than that of icosahedron. In $B_{11}C$ -CBC case, the center boron in the -CBC- chain has a distinguished peak at 215 eV which is at the upper limit of the energy range for icosahedron characteristic peaks. This has specific significance for non-crystalline boron-rich compounds since the structures of these boron-rich compounds are usually amorphous materials. Using OLCAO method, the origin of those peaks in total XANES spectra can be tracked to the specific site or clusters. Based on the principle and procedure of OLCAO method, the energy gap between core state and the conduction band increases with the atomic number of foreign atoms rising.

CHAPTER 5

ELECTRONIC STRUCTURE AND SPECTROSCOPIC PROPERTIES OF MAX

PHASE MATERIALS

5.1 Introduction

MAX is the abbreviation of $M_{n+1}AX_n$ where M is an early transition metal, A is an A-group element with a subset of groups 12-16, and X is carbon or nitrogen. According to n value, " $M_{n+1}AX_n$ " is usually referred to (n+1 1 n) phase. For instances, " M_2AX ", " M_3AX_2 ", and " M_4AX_3 " are usually referred to (2 1 1), (3 1 2), and (4 1 3) phase, respectively. MAX phase materials, ternary carbides or nitrides, are developed from binary transition-metal carbides and nitrides (MX or $M_{n+1}X$). These binary transition-metal compounds are characterized by many amazing properties, such as high hardness, high strength, high melting point, good thermal shock and wear resistance, and chemical inertness¹⁴⁸. However, these materials have fatal weaknesses: poor oxidation resistance and intrinsic brittleness, which impede useful applications. To improve the properties, main group elements (groups 12 to 16) are introduced into the binary compounds. Nowotny *et al.* first explored a large number of layered ternary compounds which inherit those good properties of binary compounds and overcome the weakness of binary compounds. MAX phase materials arouses people's great interests to explore their good mechanical properties, low electrical resistivity, and thermal stability, all of which could be useful in industrial applications¹⁴⁸.

Those physical and chemical properties of MAX phase materials have been studied in the past decades, however, the research on spectroscopic properties¹⁴⁹, especially for XANES¹⁵⁰, is very limited. MAX phase materials, especially for single-phase epitaxial

growths of thin-film samples are ideal models for characterizations of different properties (such as electronic properties, spectroscopic properties) and their anisotropies. In this work, Ti_2AlN , Cr_2AlC , and Nb_2AlC , are selected to study the correlation between XANES and different elements in the same crystal structure. Ti_2AlC and Ti_3AlC_2 are selected to investigate the correlation between XANES and crystal structures which consists of same element types. Beyond that, the roles of aluminum in MAX phase will be studied to understand the change of the properties of ternary compounds. In addition, the anisotropy in the calculated element-resolved XANES/ELNES spectra is investigated along the c-axis ($//$) and perpendicular the c-axis (\perp).

Fig. 35 shows crystal structures of phase (2 1 1) and (3 1 2) phase with layered orderings of "...AMXMAMXM..." and "...AM₂XM₁XM₂A....," respectively, where M1 and M2 denote the same transition metal element with different nearest neighbors. Strictly speaking, the local environment of an atom is not restricted to the number of nearest neighbors and their interatomic distances, but it also depends on the longer range interaction with further neighbors. The two phases are good candidates to investigate the correlation between XANES and the local environment.

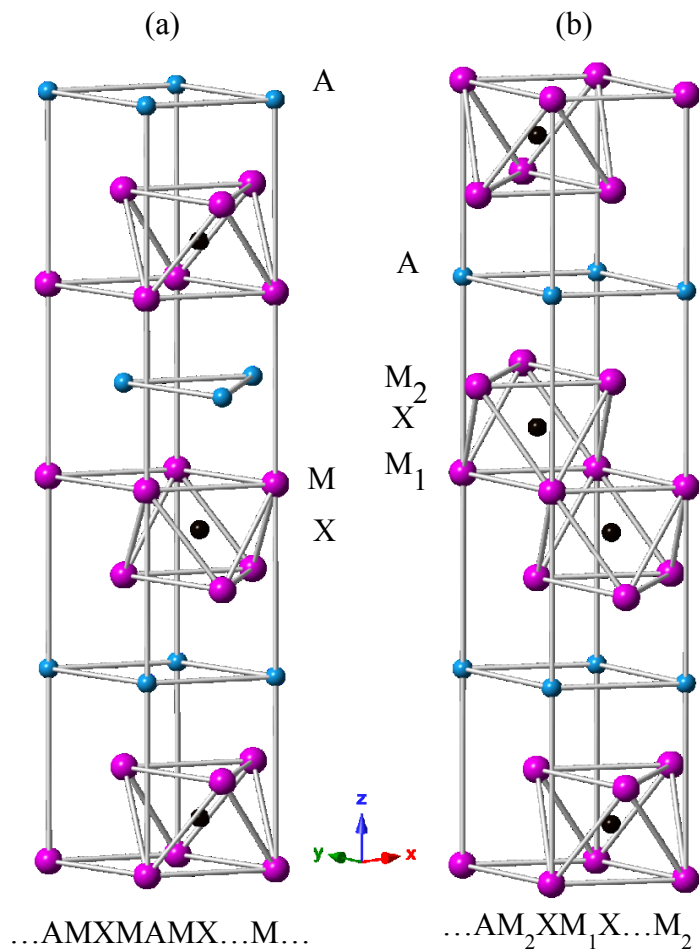


Fig. 35 Crystal structure of (a) (211) phase, (b) (312) phase.

5.2 Results on XANES/ELNES spectra

5.2.1 Electronic Structures of Ti_2AlC , Ti_2AlN , Cr_2AlC , Nb_2AlC , and Ti_3AlC_2

The electronic structures of MAX phases have been studied and reported by many groups.^{149–163} Electronic structures, especially for orbital- and element-resolved excited ones, are very important and useful to understand XANES/ELNES spectra. Here, the band structures and DOS of these five phases for the ground state are shown in Fig. 36 and Fig. 37, respectively. Research^{149,164–166} shows that the local features of the TDOS curve around the Fermi level can be used to indicate the intrinsic stability of a crystal. A local minimum

at E_F implies higher structural stability because it signifies a barrier for electrons below the Fermi level ($E < 0$ eV) to move into unoccupied empty states ($E > 0$ eV); whereas a local maximum at E_F is usually a sign of structural instability. This qualitative criterion could work well, only on those with prominent dips and peaks in the DOS at the Fermi level. In Fig. 37, these five phases have E_F located at a local minimum in the TDOS suggesting a higher level of stability.

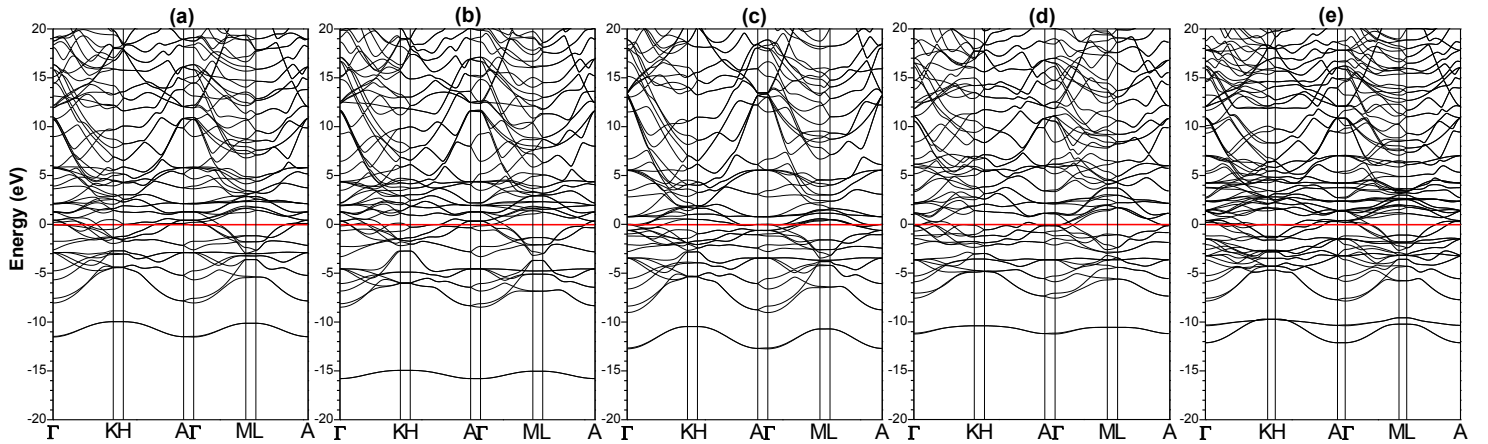


Fig. 36 Band structures of (a) Ti_2AlC , (b) Ti_2AlN , (c) Cr_2AlC , (d) Nb_2AlC , (e) Ti_3AlC_2 (red line denotes Fermi level).

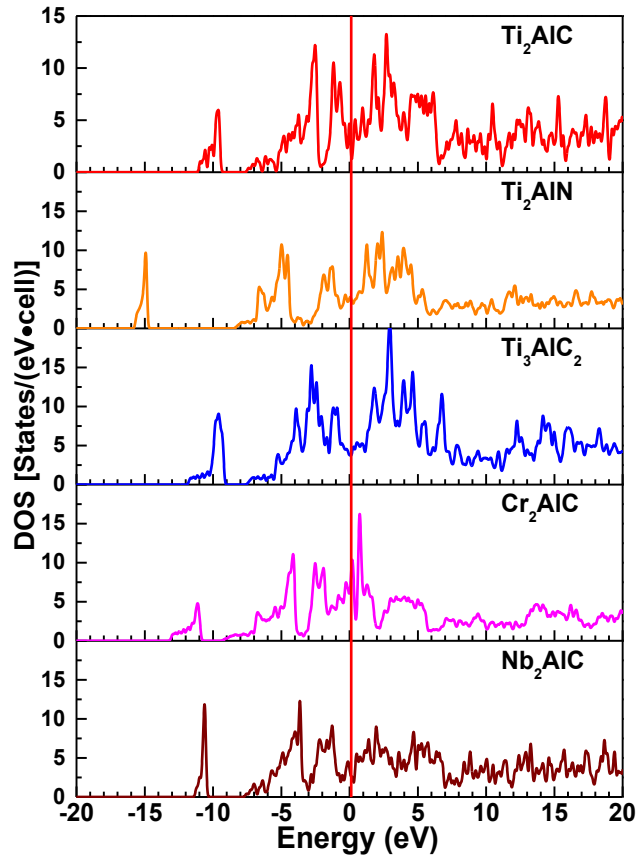


Fig. 37 Band structures of (a) Ti_2AlC , (b) Ti_2AlN , (c) Cr_2AlC , (d) Nb_2AlC , (e) Ti_3AlC_2 (red line denotes Fermi level).

5.2.2 Comparison with Experiment on the K-edges in Ti_2AlC , Ti_2AlN , and Nb_2AlC

Crystals

In Fig. 38, five experimental measurements (Ti-K and C-K in Ti_2AlC , Ti-K and N-K in Ti_2AlN , and Nb-K in Nb_2AlC) are compared to the calculated spectra. Both the calculated and the measured spectra have many spectral features in the form of peaks, valleys, and shoulders, signifying the complexity of the electronic states in the unoccupied bands of the MAX-phase compounds. The calculated spectra have more minor fluctuations than the experimental curves. The more than usual minor wavy structure come from

complicated p-component of the DOS (PDOS) in the final state conduction band (CB) (see Fig. 44 and the later discussion in page 51) and is not a result of computational inaccuracy since the supercells used in the simulation are sufficiently large and the stringent convergence criteria in the calculation have been satisfied. The features in the experimental curves are marked by A, B, C, D, E, etc. including the less recognizable shoulder-like structures. As can be seen, Ti-K edges in Ti_2AlC and Ti_2AlN have more such features followed by the N-K edge in Ti_2AlN . The C-K edge in Ti_2AlC has four well-resolved peaks A, C, E, and G. The measured Nb-K edge in Nb_2AlC has only two very broad peaks A and B. This lack of peak structures in Nb-K edge is clearly related to the overlapped element-orbital-resolved PDOS (will be interpreted in section 5.2.5 at page 103). To facilitate comparison, the calculated curves are further smoothed using a weighted adjacent averaging scheme since the more spikey features cannot be related to the measured curves. A small rigid shift in the energy scale has been applied to the calculated curves to line them up with experimental curves. After the smoothing procedure, the agreements between the calculated and measured spectra are reasonable overall, but many of the details cannot be fully reproduced. For the Nb-K edge, there are only two broad peaks in the experimental curve. Although the first broad peak A is well reproduced by the calculation, peak C at 19054 eV is not. The calculation actually shows two smaller peaks at 19030 eV and 19057 eV instead. There is some evidence that a broad shoulder at the edge onset in the calculation can be barely identified in the measured curve. Obviously, it is far more challenging to achieve good agreement between the two for XANES spectra measured at such a high energy.

Table 5 Shift in energy to align the main peak in the calculated spectra with experiment.

Phases	$\Delta E_M = E_{\text{cal.}} - E_{\text{exp.}}$ (eV)	$ \Delta E_M /E_{\text{edge}}$ (%)	$\Delta E_X = E_{\text{cal.}} - E_{\text{exp.}}$ (eV)	$\Delta E_X/E_{\text{edge}}$
Ti ₂ AlC	-8.10	0.16	-4.50	1.6
Ti ₂ AlN	0.58	0.12	4.50	1.1
Nb ₂ AlC	-368.53	1.9	-	-

For MAX-phase compounds, there is only one paper¹⁵⁰ reported using the XANES/ELNES calculation which has used self-consistent full multiple-scattering theory (FEFF8.2 code) to simulate the same five K-edge spectra. The calculated result performed by Hug *et al* reproduce the experimental spectral features quite well especially the Nb-K edge with very smooth curves. In spite of the modest agreement between our calculation and the measure spectra in fine details, it has to be emphasized that the present spectra obtained from the supercell-OLCAO method contain no experimental information other than the crystal structure and do not incorporate any input from the calculated DOS of these crystals.

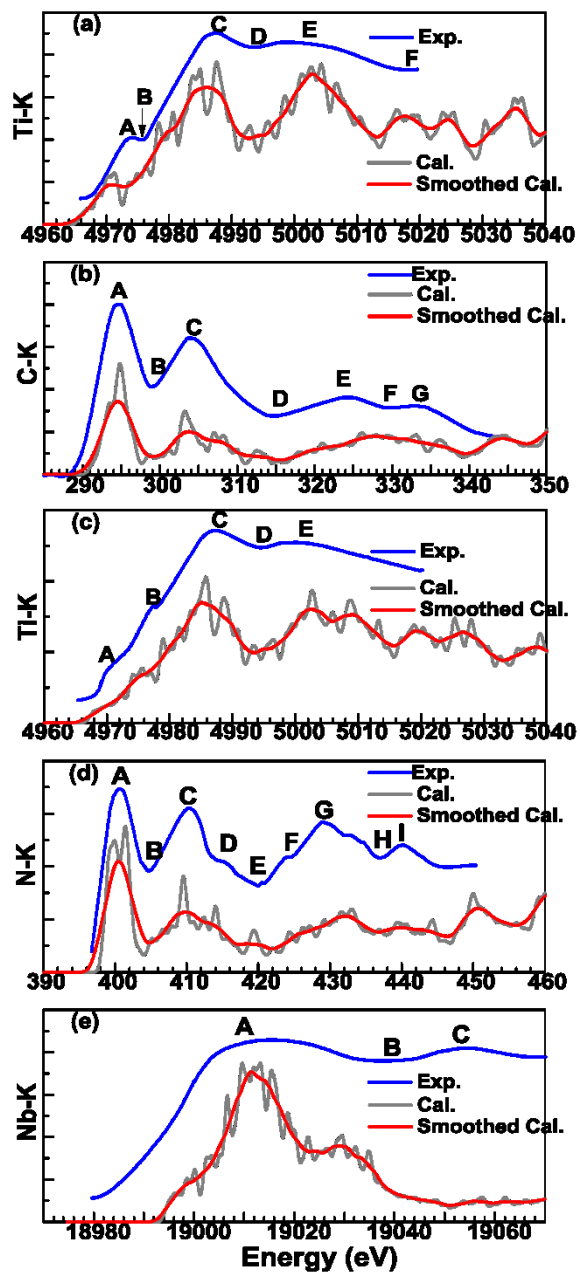


Fig. 38 Comparison of experimental (from ref. xx) and calculated XANES spectra: (a) Ti-K of Ti_2AlC , (b) C-K of Ti_2AlC ; (c) Ti-K of Ti_2AlN , (d) N-K of Ti_2AlN ; (e) Nb-K of Nb_2AlC .

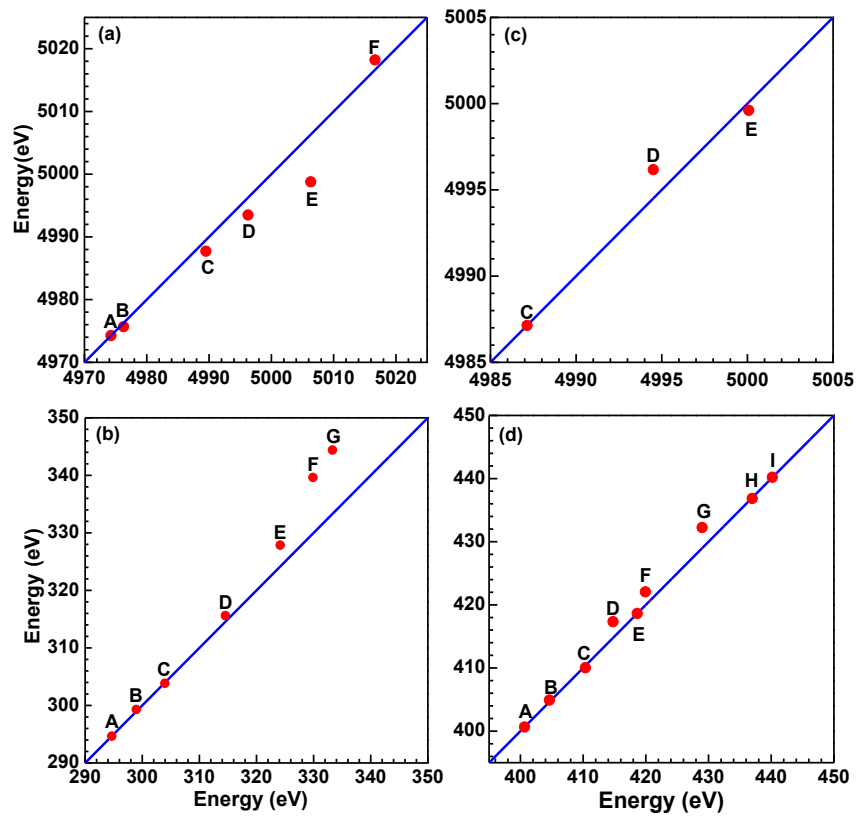


Fig. 39 Calculated (y-axis) vs. experimental (x-axis) values of spectral features of: (a) Ti-K in Ti_2AlC , (b) C-K in Ti_2AlC , (c) Ti-K in Ti_2AlN and (d) N-K in Ti_2AlN

5.2.3 Calculated Edge Spectra in Cr_2AlC and Ti_3AlC_2

Based on the reasonable agreement shown above, the K edge spectra for two more crystals (Cr_2AlC and Ti_3AlC_2) were performed. The goal is to ascertain the difference between Cr-K and Nb-K edges (and also other edges) in the same (2 1 1) structure, and the difference in the Ti-K and other edges in the (2 1 1) and (3 1 2) structures. The results are shown in Fig. 40 and Fig. 41, respectively, without the smoothing process. The differences in the calculated Cr-K edge and the Nb-K edge in Cr_2AlC and Nb_2AlC are quite substantial. This is due to the fact that early transition metal Cr and late transition metal Nb have different numbers of d electrons hence different electronic structures. Cr-K edge has many peaks that can be very roughly organized into four groups with centroids around 5975 eV, 5992 eV, 6012 eV, and 6038 eV above the edge onset whereas the Nb-K edge has the main broad peak centered at around 17 eV above the edge onset. An unexpected finding is the large difference in the C-K edges in Cr_2AlC and Nb_2AlC . We focus our discussion on the first 10 eV range with large absorptions. The C-K edge in Cr_2AlC consists of a near-symmetric peak at 290.5 eV with one shoulder 2.0 eV above and the other shoulder 1.5 eV below the central peak. On the other hand, the C-K edge in Nb_2AlC has two well defined peaks, one at 289.5 eV and a sharper one at 292 eV. One can trace this large difference to the very difference in the next NN bonding configurations between Nb and C vs. Cr and C, as shown in recent work by Mo *et al.*¹⁴⁹

For spectral comparison between Ti_2AlC and Ti_3AlC_2 , the situation is quite different. In spite of the multiple peak structures in the Ti-K edge spectra, the general features are very close considering that Ti_3AlC_2 has two M sites, Ti1 and Ti2, which have different local environments and slightly different spectra. However, the spectral features

of Ti2 in Ti_3AlC_2 are very similar to that of Ti in Ti_2AlC and less so for Ti1. The differences in the C-K edges are not as spectacular as in the case between Cr_2AlC and Nb_2AlC . Both have two sharp peaks roughly 10 eV apart but with different secondary structures due to differences in the Ti-C bonds in these two crystals. These fine differences clearly reflect the level of accuracy in the present method for XANES/ELNES calculation in delineating the subtle dependency of the calculated spectra on local geometry.

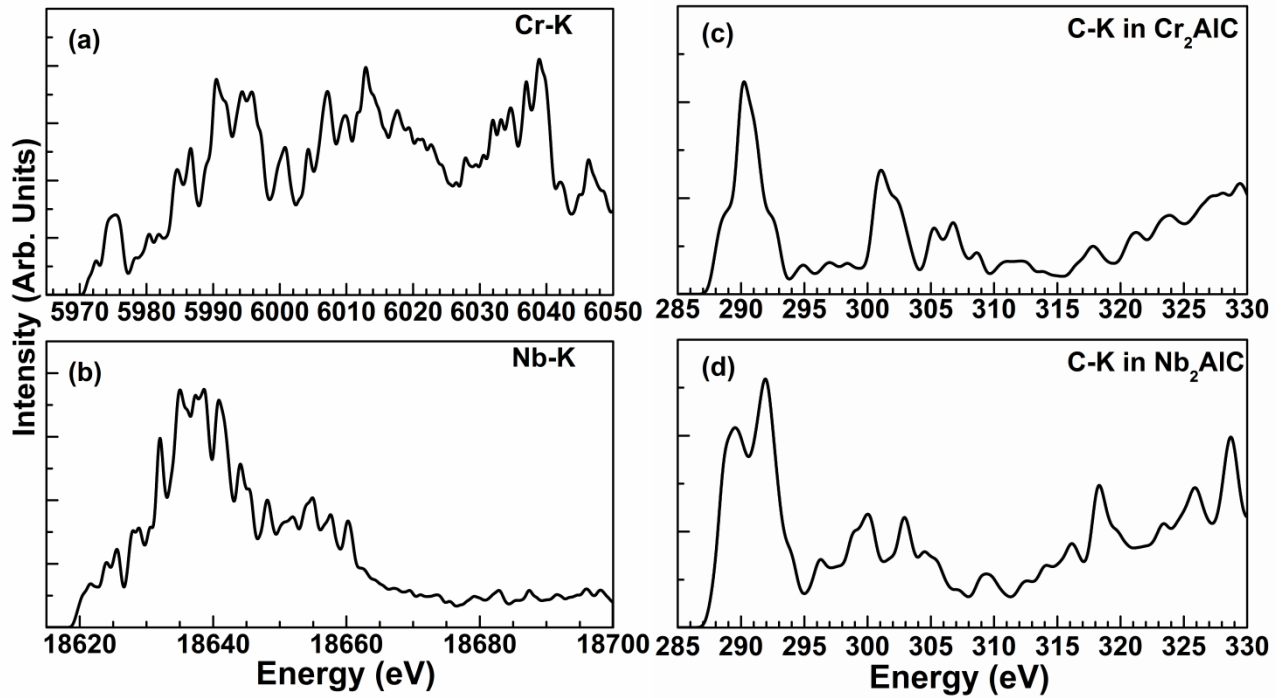


Fig. 40 Calculated spectra of (a) Cr-K in Cr_2AlC compared with (b) Nb-K in Nb_2AlC , and (c) C-K in Cr_2AlC and (d) C-K in Nb_2AlC .

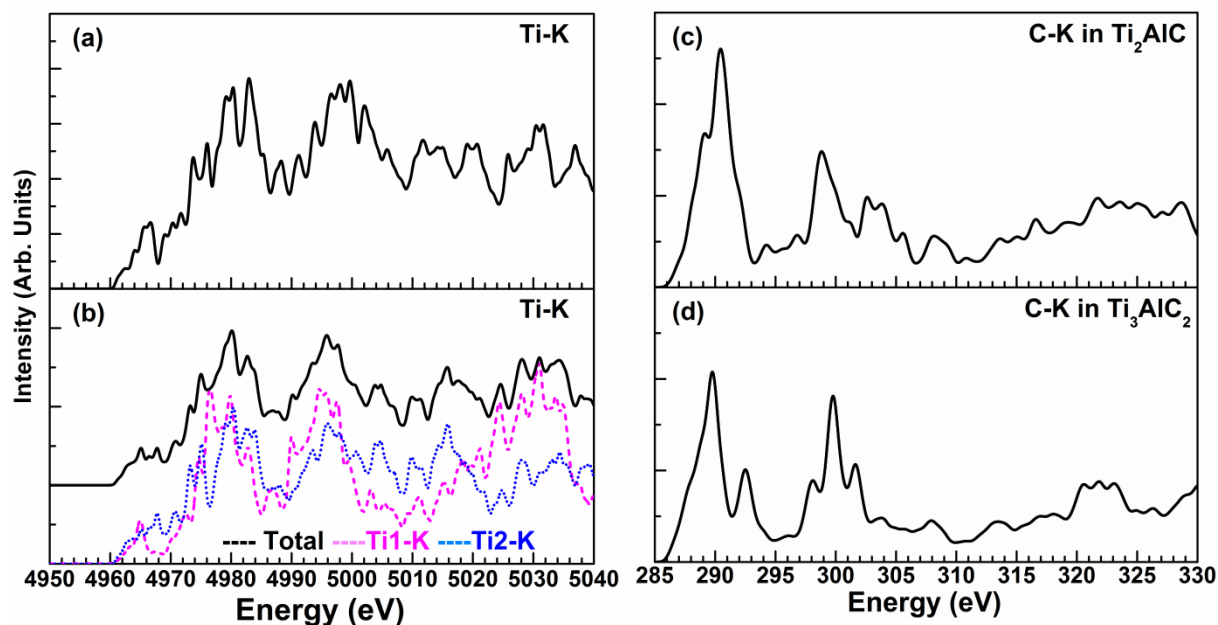


Fig. 41 Comparison of calculated Ti-K in (a) Ti_2AlC and (b) Ti_3AlC_2 , and C-K in (c) Ti_2AlC and (d) Ti_3AlC_2 .

5.2.4 Results on Al-K and Al-L₃ Edges in All Five MAX phases

Al plays a pivotal role in the structure and properties of MAX-phase compounds with $A = \text{Al}$. Many researchers believe that the MAX-phase compounds are essentially derived from the binary TM carbides and nitrides by inserting Al layers. In fact, the synthesis of MAX-phase compounds in the early days was motivated by the improvement of mechanical properties by the addition of Al to binary carbides and nitrides^{148,158}. It is therefore quite intriguing that no XANES or ELNES spectra for Al in the MAX-phase compounds have been reported so far. The Al-K and Al-L₃ edges in the five MAX crystals have been calculated. The results are presented in Fig. 42 and Fig. 43, respectively which can be used to compare with future measurements. We roughly divide the absorption energy range into two regions, I and II. For the Al-K edge, region I covers the range from the edge onset to 1597 eV. In this region, the Al-K edges for Ti_2AlC , Ti_2AlN , and Ti_3AlC_2

are quite similar to each other, all having three peaks after the onset. They differ from the Al-K edge of Cr_2AlC and Nb_2AlC . In region II, above 1597 eV, there is a sharp and prominent peak around 1601 eV in Ti_2AlC and Ti_3AlC_2 , but not in Ti_2AlN . The same single sharp peak is in Cr_2AlC at 1605 eV. In Nb_2AlC , there is a double peak feature at 1599 eV and 1601 eV. These differences certainly reflect the near-neighbor environments of the Al atoms in these crystals, especially the difference in Al-C or Al-N bonding. The greater than 4 eV difference between Nb_2AlC and Cr_2AlC in the position of the peak in region II reflects the influence of the different number of d electrons on the p -orbital dominated states of Al in the CB.

The Al- L_3 edge describes the transitions from the Al- $2p$ core levels to the $(s+d)$ dominated states in the CB. In region I, from the edge onset to about 100 eV, the spectral features show multi-peak structures and steadily increasing absorption that reaches a maximum in the range between 90 and 100 eV with minor structures varying from one crystal to another. Nevertheless, the variations are much smaller in Ti_2AlC , Ti_2AlN , and Ti_3AlC_2 and somewhat larger in Nb_2AlC and Cr_2AlC with respect to the locations of the centroids of the spectral weight. The same observation in the spectral variation can also be found in region II from 100 eV onward.

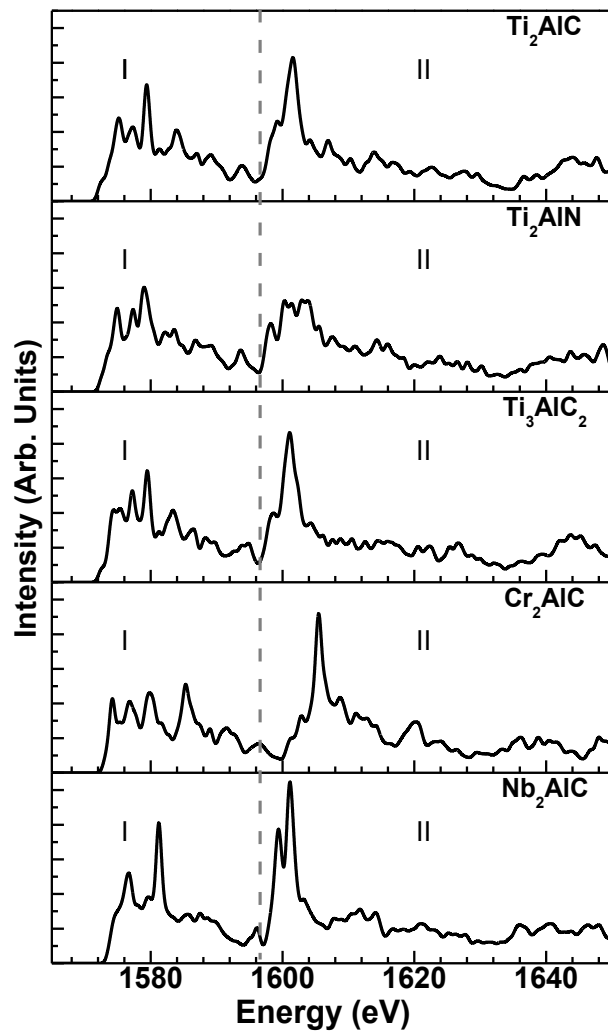


Fig. 42 Calculated Al-K edges in Ti_2AlC , Ti_2AlN , Ti_3AlC_2 , Cr_2AlC and Nb_2AlC

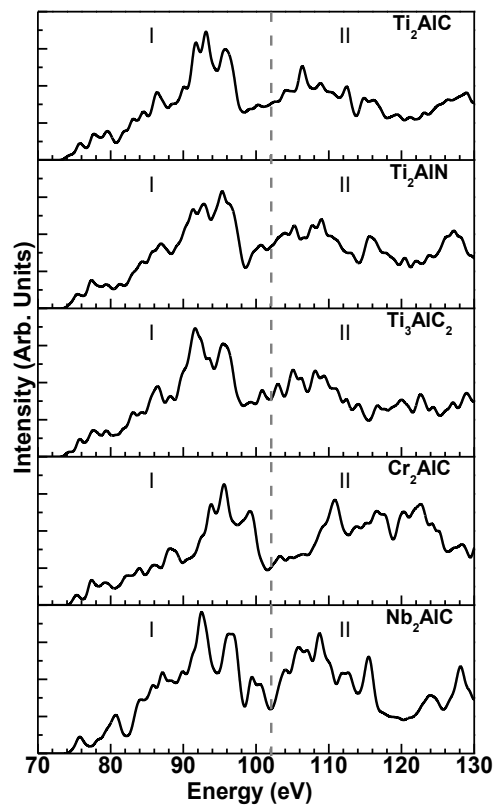


Fig. 43 Calculated Al-L₃ edges in Ti₂AlC, Ti₂AlN, Ti₃AlC₂, Cr₂AlC and Nb₂AlC.

5.2.5 Relation to the Electronic Structure of the MAX Phases for Excited State

Although the electronic structures of the five MAX-phase compounds have been studied by many groups^{150,151,155–157,160}, including recent work from us¹⁴⁹, the excited state orbital-resolved PDOS was rarely reported to help understand the XANES/ELNES spectra. We have calculated the atom- and orbital-resolved partial DOS (PDOS) of the final states in the five MAX crystals. This is illustrated in Fig. 44 in which we displayed the total *p*-components of the total and the atom-resolved PDOS in all five crystals properly aligned with the calculated K-edge spectra. This figure further supported the explanation of the seemingly wavy spectra for the M-K edges discussed in section 5.2.2 and the difference in the Cr-K and Nb-K edges in section 5.2.3 in spite of the fact that Cr and Nb differ by only one electron in the 3d shell. Noticeably, *p*-orbital PDOSs of Nb, Al, and C are overlapped each other. This explains why the Nb-K edge is lack of structures. We have also listed in Table 6 the nearest and next nearest neighbor distances of the metal ion in the five crystals. It shows that the bond distance can differ considerably even when they have the same crystal structure and differ by only one valence electron in one of the elements. This is particularly true in Cr₂AlC and Nb₂AlC since Nb is a much larger atom than Cr. Except for simple crystals, interpretation of the spectra through the DOS cannot be performed beyond general trends because of the inherent complexity of the spectra and PDOS, but also because the computation of the spectra involves the explicit inclusion of the momentum matrix connecting the initial and final states (core-hole state). The momentum matrix modulates the peaks of the DOS, and with complex crystals such as the MAX-phase compounds the degree of modulation can often completely mask the connection between the DOS and the XANES/ELNES spectra. Regardless, based on the procedure of XANES/ELNES

calculation within OLCAO method, the excited state orbital-resolved PDOS was computed and some general trends were observed.

For the C-K edge (N-K edge) spectra the p-orbital DOS from different elements indicates that the Al and C (N) are the most likely final states from the edge onset up to about 15eV. After 15eV the M element becomes dominant. For Al-K edge spectra the situation is similar. Al-L₃ edge spectra the final states are (*s* + *d*) orbitals so that the transition metal M element has the most substantial impact in the first few eV, but beyond that there is no clear trend. Thus the prospect of using spectral features in XANES/ELNES spectra to characterize the electronic structure and vice versa is quite limited. A more fruitful practice is to study the spectral anisotropy in layered compounds such as MAX phases which can be easily measured.

Table 6 Distances (Å) between M and the 1st (2nd) nearest neighbors in the five MAX phases

Crystal	M-M	M-Al	M-X
Ti ₂ AlC	2.924 (3.040)	2.838	2.109
Ti ₂ AlN	2.899 (2.899)	2.844	2.082
Ti ₃ AlC ₂	2.968 (3.075)	2.879	2.137
Cr ₂ AlC	2.754 (2.858)	2.672	1.984
Nb ₂ AlC	3.026 (3.119)	2.864	2.173

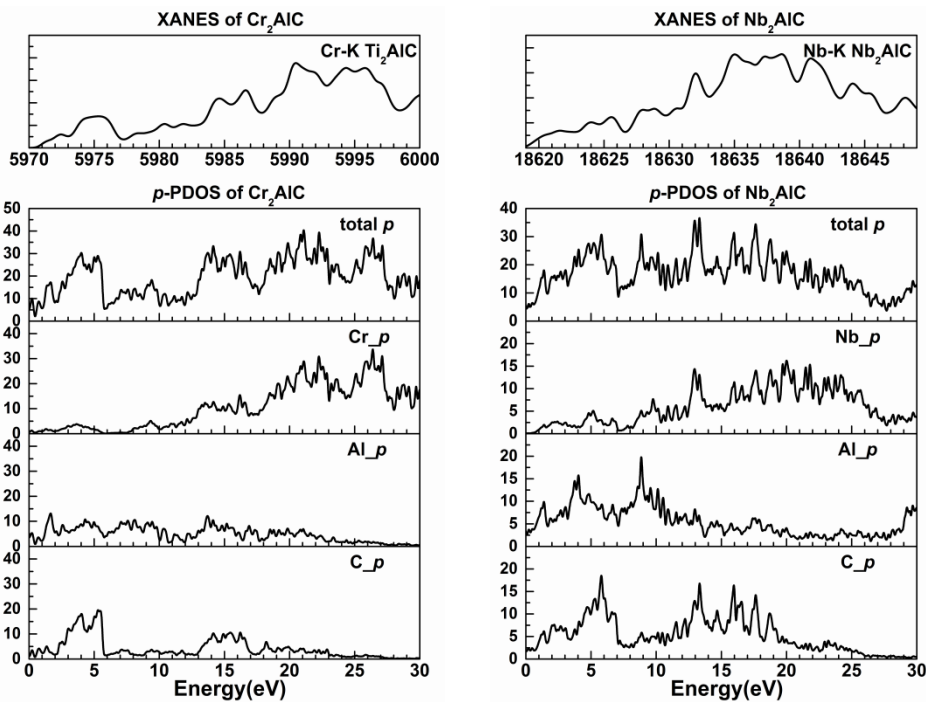
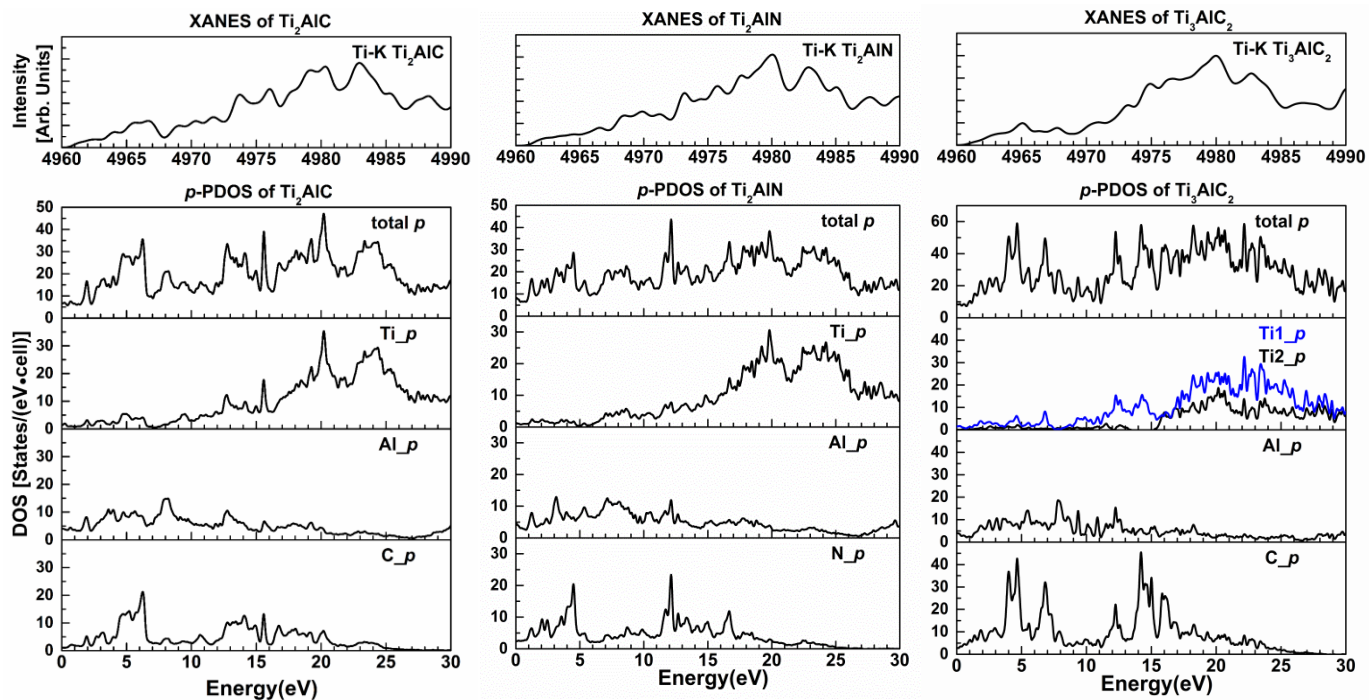


Fig. 44 Top panel: Calculated M-K edges in Ti_2AlC , Ti_2AlN , Ti_3AlC_2 , Cr_2AlC , and Nb_2AlC . Lower panel, the excited calculated total PDOS for the p-components in the CB and their contribution from each type of elements M, Al, X.

5.2.6 Anisotropy in the XANES/ELNES Spectra

MAX-phase materials exhibit anisotropy in geometrical structures and the anisotropy of XANES spectra will be an important part of experimental observation related to their structures. Experimental measurements of anisotropy in XANES spectra are technically more challenging and have been measured only in crystals with simpler structures²⁵. Here we present the calculated results on the directionally resolved XANES spectra of M (Ti, Cr, and Nb), Al, and X (C and N) in the x - y plane and along the z direction. It can be seen that for all of the crystals studied, anisotropy in the XANES/ELNES spectra exists with the component in the x - y plane having larger integrated strength than the z -component over the range of absorption displayed. This anisotropy is most pronounced in the case of the Al-K edge (Fig. 46 (a)) where the leading peak is due almost entirely to in-plane excitation. There are also numerous other anisotropic structures, but the trends are less clear. In the case of the Al-L₃ spectra (Fig. 46 (b)) there is an overall much weaker anisotropy but the exception appears in the first 5-8 eV range after the edge onset. Here, each crystal has a consistent set of three peaks where the first and third have little to no anisotropy while the second peak is due almost entirely to the in-plane excitation. This point in particular may be of value for spectral measurements via ELNES where the direction of the beam can be more easily controlled.

Fig. 35 shows that Al atoms in MAX-phase compounds form a plane so that the intra-plane interaction is solely between the Al atoms. Those in the axial direction are with the metal ions at different angles. For the same reason, Fig. 47 shows that the z -component of the spectra in C-K and N-K edges are less strong than that of the planar components

since there are no metal atoms directly above or below the X atoms (C or N) whereas there are large planar components from multiple metal atoms. The anisotropy for the spectra from metal ions (Fig. 45) also lacks a clear pattern. One observation is that the anisotropy in the Ti-K edge in Ti_2AlC and Ti_2AlN are almost the same, indicating that as long as directional bonding is concerned, the X atom (C or N) makes little difference in their bonding to metal ions. On the other hand, there are substantial differences in the anisotropy in the Ti-K edge between Ti_2AlC and Ti_3AlC_2 . This can of course be traced to the fact that in Ti_3AlC_2 , there are two metal sites (Ti1 and Ti2) of different local geometry as already discussed above. Such differences not only affect the Ti-K edge but also its anisotropy. In the Cr-K edge, the anisotropy is most obvious in the energy range above 6005 eV where the planar component almost doubles the axial component. The situation for anisotropy in the Nb-K edge is quite different. Although there is considerable anisotropy along the entire spectrum, there are no places where it particularly stands out such that it might be easily detectable within the limits of resolution at that high energy.

The above results on the spectral anisotropy in MAX compounds show that there is subtle information that may be explored experimentally and computationally to analyze the XANES/ELNES spectra that may be useful in identify new MAX phases and their solid solutions.

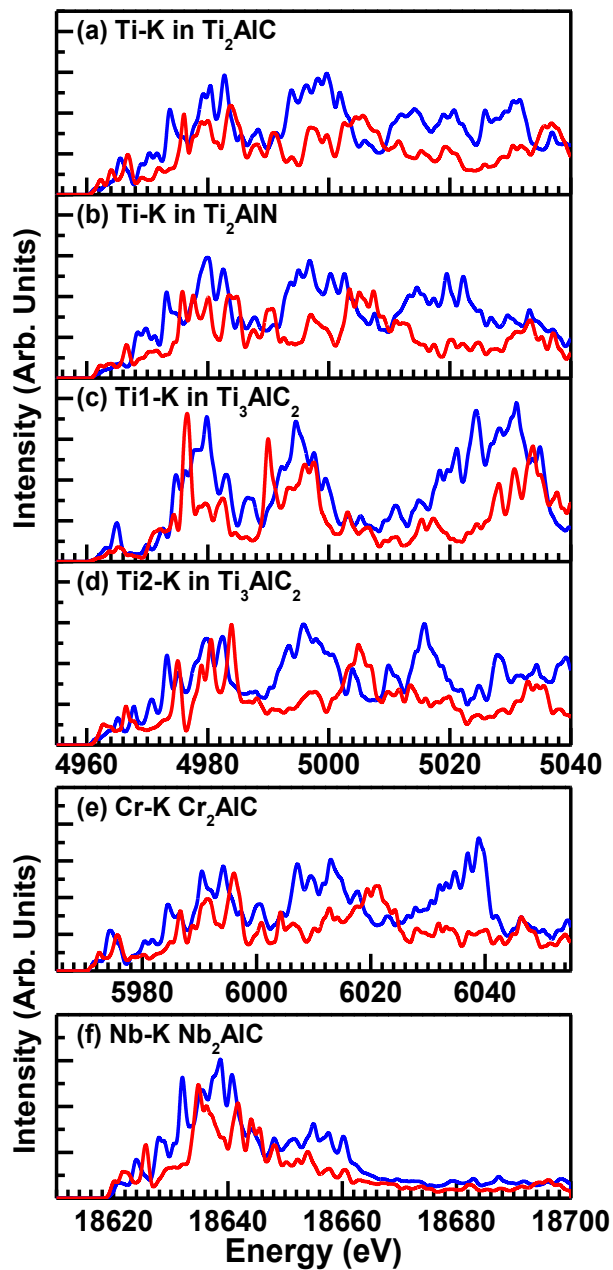


Fig. 45 Directionally resolved XANES spectra of (a) Ti-K in Ti_2AlC , Ti_2AlN , Ti_3AlC_2 ; (b) Cr-K in Cr_2AlC ; (c) Nb-K in Nb_2AlC (blue solid line denotes x-y plane; red dot line denotes z-direction).

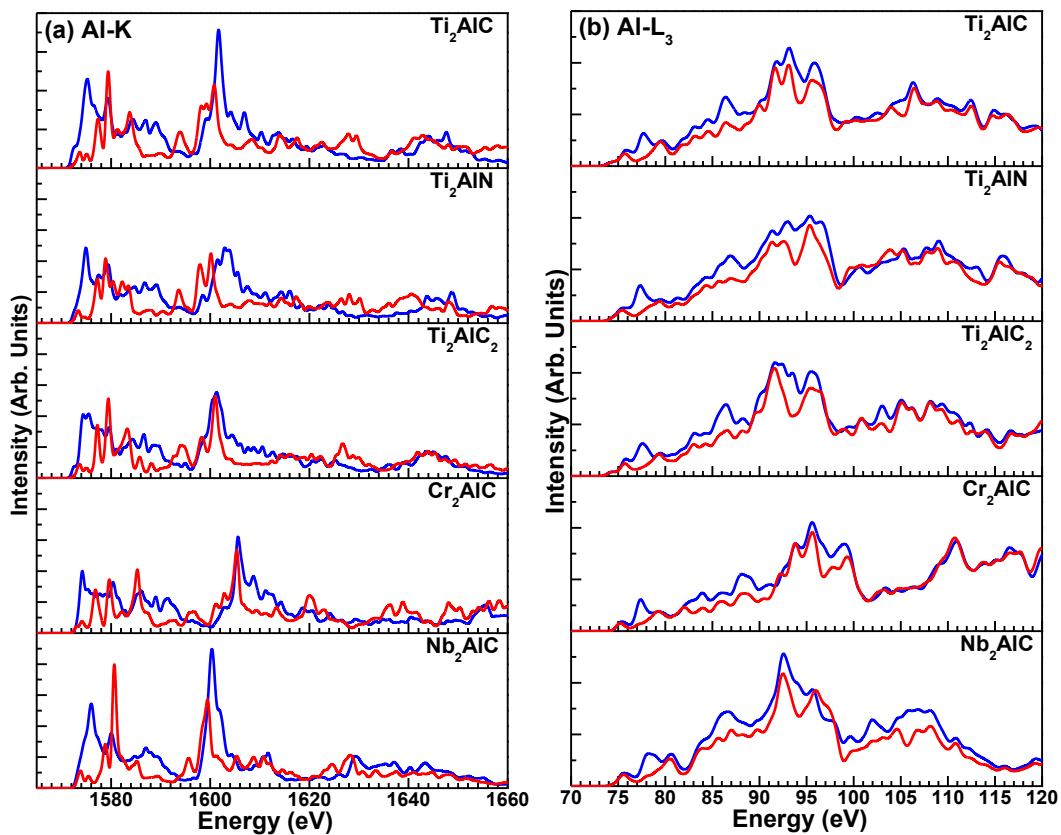


Fig. 46 Directionally resolved XANES spectra of (a) Al-K and (b) Al-L₃ in Ti₂AlC, Ti₂AlN, Ti₃AlC₂, Cr₂AlC and Nb₂AlC (blue solid line denotes x-y plane; red dot line denotes z-direction).

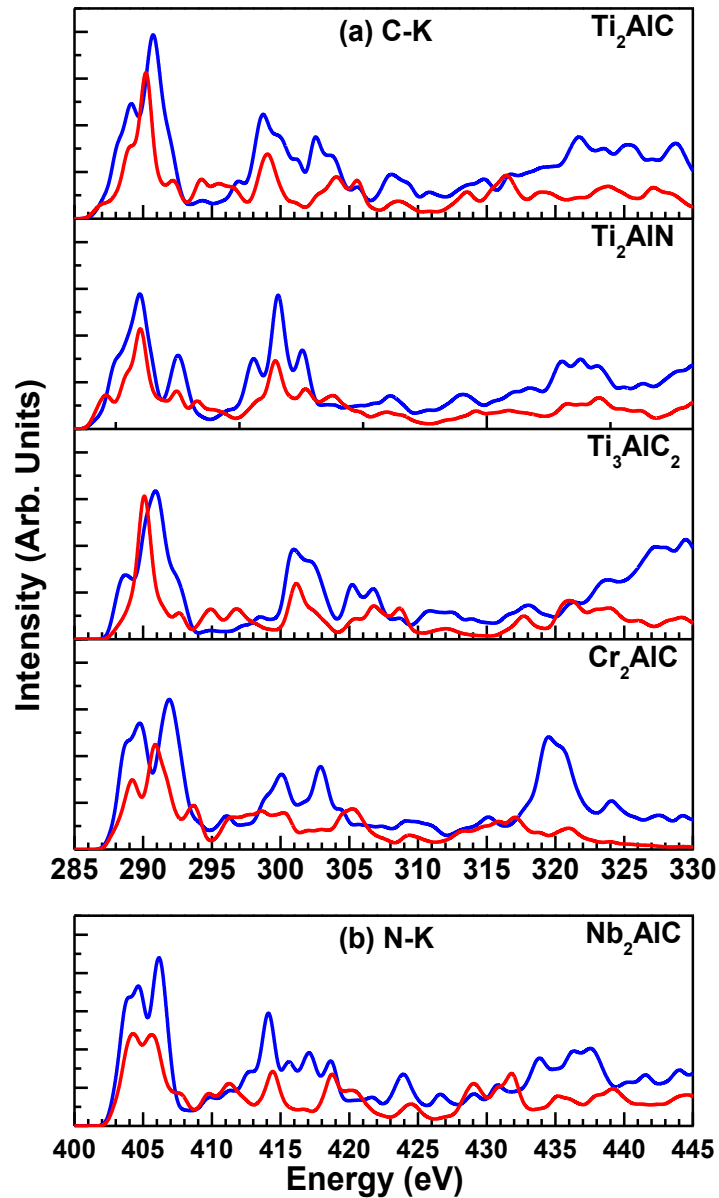


Fig. 47 Directionally resolved XANES spectra of (a) C-K in Ti_2AlC , Cr_2AlC , Nb_2AlC , Ti_3AlC_2 ; (b) N-K in Ti_2AlN (blue solid line denotes x-y plane; red dot line denotes z-direction).

5.3 Conclusion

The calculated XANES/ELNES edge spectra in five MAX-phase compounds (Ti_2AlC , Ti_2AlN , Ti_3AlC_2 , Cr_2AlC , and Nb_2AlC) are in reasonable agreement with the five experimental spectra available. Based on this agreement, the Al-K and Al-L₃ edges of all phases, the Cr-K and C-K edges of Cr_2AlC , and the C-K edge of Nb_2AlC are predicted. We further resolved all calculated spectra into planar and axial components according to the anisotropic geometry of the crystals. The complex features observed in both the measured and calculated spectra may be difficult to interpret in terms of the empty conduction band states in the context of electronic interactions among the M, A, and X elements in the MAX-phase compounds. However, the anisotropy in the spectrum at specific sites could offer additional opportunity to understand the local bonding in MAX phase compounds. One of the goals of this work is to stimulate additional experimental measurements on MAX-phase compounds, especially the Al-K and Al-L₃ edges, along with their anisotropic features so that comparison can be made with our theoretically predicted spectra. With additional calculations and measurements on many other MAX-phase compounds and on their quaternary solid solutions, further advances in the fundamental understanding of the structure and properties of this fascinating class of metallic compounds can be anticipated.

CHAPTER 6

SUMMARY AND FUTURE WORK

6.1 Overview

The electronic structures and spectroscopic properties of elemental boron, boron-rich compounds, and MAX phases were studied and investigated using an *ab initio* OLCAO method which is DFT based. Simultaneously, the XANES technique was further understood and investigated as well. Although much work has been finished in the past six years, there are many problems and challenges left. The difficulties and challenges are presented below and the achievements are also summarized. Then, the perspective for future work will be given.

XANES/ELNES, as a tool to explore the unoccupied conduction band or unoccupied top of valence band, is element specific since the various elements have different core level energies. It is very sensitive to local environment and permits extraction of the signal from a surface monolayer or even a single buried layer in the presence of a huge background signal. XANES can also determine the chemical state of elements which are present in bulk in minute quantities; it has been widely used in environmental chemistry and geochemistry. Although XANES has been studied for a couple of decades, there are lots of questions waiting for solutions or clarifications.

First, interpretation of experimental XANES/ELNES needs a set of complete reference compounds which were used to identify the local environment of a specific element in a sample¹⁶⁷. The limitation is obvious when the reference spectra are hard to find or achieve. Even when the reference spectra can be achieved, the interpretation based on the reference spectra is still very limited since the experimentalists only can interpret

the XANES spectra of a sample through drawing comparisons between samples and references. Further deep insight is very hard to give without theoretical calculations.

Second, local environment is a very abstract term which includes multiple components, such as the element type of the target atom and the 1st and 2nd nearest neighbor atoms, the structure, bond length, bond angle, which can simultaneously influence the absorption. Although there are some packages which can perform the XANES/ELNES spectra and reproduce the experimental measurement well, it is still very difficult to interpret which factor plays a dominant role and which plays a lesser role. To interpret the spectra change with factors, we need to build up different models which only provide one or two varied factors and the others are fixed. This advances a pretty high requirement since these factors usually interact with each other so that it is very difficult to separate them from one another. For example, a perfect icosahedron has same bond length and bond angle. However, any change for the bond length or bond angle results in other factors changing.

Third, as mentioned above, XANES is sensitive to local environment. However, behind these specific components, there are many physical and chemical factors interacting with each other. How to connect these physical and chemical factors with those environmental components is a huge challenge which cannot and should not be avoided because understanding these parts can help to understand experimental phenomenon, design and conduct experiments in the right way. For example, the electron deficiency determines a specific bond, 3c-2e bond, in elemental boron. Fujimori *et al.*⁹⁴ proved that three polar sites form a 3c-2e bond which requires the distance between the three sites

should be same or very similar and the two electrons should be shared evenly. The question will be advanced naturally:

1. Is the 3c-2e bond the dominant factor which makes the inter-bonds shorter than the intra-bonds⁹⁴?
2. Will it exist if some foreign elements, such as carbon, nitrogen, oxygen, are introduced in the cell?
3. Does the 3c-2e bond influence the XANES spectra? If it does, how can we correlate the XANES to the 3c-2e?

.....

In addition, the number of different clusters in an amorphous material and the arrangements for these clusters might be infinite; however, the number of these basic clusters (models) is limited. Thus, it is significant to study these basic clusters. If we built up all these limited-amount models and achieve the character features for these models, we can judge the possible clusters from the experimental measurements. In section 3.3.2 (Fig. 16 (b) shown in page 51), the trial has been successfully applied to analyze XANES spectra of elemental boron and boron-rich compounds. Noticeably, the linear part might present a way to figure out the amount of clusters in a sample. It suggests a possible quantitative way to further study a sample although the model is overly simple.

6.2 Prospects of Future Work

The research on nano elemental boron and amorphous boron-rich compounds are confronting a big challenge: how to understand the properties without a determined structure. To author's knowledge, people use different packages, such as Molecular dynamics (MD) package, to get a specific model and simulate its properties. However, for a big system with thousands of atoms, the amount of possible arrangements is a tremendous number.

If we select a cluster with a suitable size, then the system can be greatly simplified and the work load of modeling and calculating can be acceptable. After all, the amount of arrangement for the basic clusters is limited. Once when we completely studied these clusters, then we can use these models to understand the phenomenon. Boron-rich compounds ($B_{11}C$ -CBC), for example, can be broken into two parts: non-icosahedral part and icosahedral clusters with different arrangements including defects. We can get the basic understanding for these cluster models. Then the whole system can be figured out based on the basic understanding or observation. In this work, the correlation between XANES and bond length has been investigated. Based on the perfect icosahedral models with different bond length, the characteristic features have been identified. Furthermore, if the models with varied bond angle, the models with different defective arrangements, such as vacancy, interstitial sites, alien atoms, can be built up, then the research will be greatly simplified.

REFERENCES

1. Albert, B. & Hillebrecht, H. Boron: Elementary Challenge for Experimenters and Theoreticians. *Angew. Chemie Int. Ed.* **48**, 8640–8668 (2009).
2. Ekimov, E. A. & Zibrov, I. P. High-pressure high-temperature synthesis and structure of α -tetragonal boron. *Sci. Technol. Adv. Mater.* **12**, 55009 (2011).
3. Isaev, E. I. *et al.* Impact of lattice vibrations on equation of state of the hardest boron phase. *Phys. Rev. B* **83**, 132106 (2011).
4. Landau, D. P. & Binder, K. *A guide to Monte Carlo Simulation in Statistical Physics*. 384 (2000).
5. Engel, E. & Dreizler, R. M. *Density Functional Theory*. Springer **2010**, 543 (Springer Berlin Heidelberg, 2011).
6. Hohenberg, P. & Kohn, W. Inhomogeneous Electron Gas. *Phys. Rev.* **136**, B864–B871 (1964).
7. Kohn, W. & Sham, L. J. Self-Consistent Equations Including Exchange and Correlation Effects. *Phys. Rev.* **140**, A1133–A1138 (1965).
8. Ching, W.-Y. & Rulis, P. X-ray absorption near edge structure/electron energy loss near edge structure calculation using the supercell orthogonalized linear combination of atomic orbitals method. *J. Phys. Condens. Matter* **21**, 104202 (2009).
9. Balbás, L., Martins, J. & Soler, J. Evaluation of exchange-correlation energy, potential, and stress. *Phys. Rev. B* **64**, 165110 (2001).
10. Slater, J. C. & Koster, G. F. Simplified LCAO Method for the Periodic Potential Problem. *Phys. Rev.* **94**, 1498 (1954).
11. Bloch, F. Über die Quantenmechanik der Elektronen in Kristallgittern. *Zeitschrift für Phys.* **52**, 555–600 (1929).
12. Ching, W.-Y. & Rulis, P. *Electronic Structure Methods for Complex Materials: The orthogonalized linear combination of atomic orbitals*. (Oxford University Press, USA, 2012). at <<http://www.amazon.com/Electronic-Structure-Methods-Complex-Materials/dp/0199575800>>
13. Rulis, P. Computational Studies of Bioceramic Crystals & Related Material. *Dep. Phys.* **PhD**, (2005).

14. Ching, W. Y. Theoretical Studies of the Electronic Properties of Ceramic Materials. *J. Am. Ceram. Soc.* **73**, 3135–3160 (1990).
15. Ouyang, L. Parallel computing and first-principles calculations: applications to complex ceramics and Vitamin B12. (2000).
16. G. Kresse & Furthmüller, J. Efficiency of ab initio total energy calculation for metals and semiconductors using plane wave basis set. *Comput. Mater. Sci.* **6**, 15–50 (1996).
17. Kresse, G. & Furthmüller, J. Efficient iterative schemes for ab initio total-energy calculations using a plane-wave basis set. *Phys. Rev. B* **54**, 11169 (1996).
18. Ching, W., Ouyang, L., Rulis, P. & Yao, H. Ab initio study of the physical properties of γ -Al₂O₃: Lattice dynamics, bulk properties, electronic structure, bonding, optical properties, and ELNES/XANES spectra. *Phys. Rev. B* **78**, 014106 (2008).
19. Rulis, P., Wang, L. & Ching, W. Y. Prediction of γ -B 28 ELNES with comparison to α -B 12. *Phys. status solidi - Rapid Res. Lett.* **3**, 133–135 (2009).
20. Ching, W.-Y. & Rulis, P. Ab initio calculation of the electronic structure and spectroscopic properties of spinel γ -Sn₃N₄. *Phys. Rev. B* **73**, 45202 (2006).
21. Rulis, P., Yao, H., Ouyang, L. & Ching, W. Y. Electronic structure, bonding, charge distribution, and x-ray absorption spectra of the (001) surfaces of fluorapatite and hydroxyapatite from first principles. *Phys. Rev. B (Condensed Matter Mater. Physics)* **76**, 245410–245415 (2007).
22. Ching, W. Y. & Rulis, P. Large differences in the electronic structure and spectroscopic properties of three phases of AlPO₄ from ab initio calculations. *Phys. Rev. B (Condensed Matter Mater. Physics)* **77**, 125116–125117 (2008).
23. Hussain, A., Aryal, S., Rulis, P., Choudhry, M. A. & Ching, W. Y. Density functional calculations of the electronic structure and optical properties of the ternary carbides Al₄SiC₄ and Al₄Si₂C₅. *Phys. Rev. B (Condensed Matter Mater. Physics)* **78**, 195102–195109 (2008).
24. Ching, W. Y. & Rulis, P. Ab initio calculation of the O-K, N-K, Si-K, Si-L₃, Y-K, Y-L₃ edges in the Y-Si-O-N system: A strategy for ELNES/XANES spectral modeling in complex materials. *Phys. Rev. B* **77**, 035125 (2008).
25. Mizoguchi, T. *et al.* First-principles calculations of ELNES and XANES of selected wide-gap materials: Dependence on crystal structure and orientation. *Phys. Rev. B* **70**, 045103 (2004).

26. Ching, W. Y., Ouyang, L., Rulis, P. & Tanaka, I. Prediction of the X-ray absorption near edge structure of the new high-density phase of SiO₂. *Phys. status solidi* **242**, R94–R96 (2005).
27. Ching, W.-Y., Mo, S.-D. & Chen, Y. Calculation of XANES/ELNES Spectra of All Edges in Si₃N₄ and Si₂N₂O. *J. Am. Ceram. Soc.* **85**, 11–15 (2004).
28. Mo, S.-D. & Ching, W. Y. X-ray absorption near-edge structure in alpha-quartz and stishovite: Ab initio calculation with core–hole interaction. *Appl. Phys. Lett.* **78**, 3809 (2001).
29. Rulis, P. & Ching, W. Y. Theoretical ELNES spectra of Si-K, Si-L, N-K, and O-K edges of an intergranular glassy film model in β-Si₃N₄. *J. Mater. Sci.* **46**, 4191–4198 (2011).
30. Liang, L., Rulis, P., Ouyang, L. & Ching, W. Y. Ab initio investigation of hydrogen bonding and network structure in a supercooled model of water. *Phys. Rev. B* **83**, 024201 (2011).
31. Ching, W. Y., Aryal, S., Rulis, P. & Schnick, W. Electronic structure and physical properties of the spinel-type phase of BeP₂N₄ from all-electron density functional calculations. *Phys. Rev. B* **83**, 155109 (2011).
32. Mo, S.-D. & Ching, W. Ab initio calculation of the core-hole effect in the electron energy-loss near-edge structure. *Phys. Rev. B* **62**, 7901–7907 (2000).
33. Wang, L., Rulis, P. & Ching, W. Y. Calculation of core-level excitation in some MAX-phase compounds. *J. Appl. Phys.* **114**, 023708 (2013).
34. Haines, J., Léger, J. M. & Bocquillon, G. SYNTHESIS AND DESIGN OF SUPERHARD MATERIALS. *Annu. Rev. Mater. Res.* **31**, 1–23 (2001).
35. Veprek, S., Zhang, R. & Argon, A. Mechanical properties and hardness of boron and boron-rich solids. *J. Superhard Mater.* **33**, 409–420 (2011).
36. Domnich, V., Reynaud, S., Haber, R. A. & Chhowalla, M. Boron Carbide: Structure, Properties, and Stability under Stress. *J. Am. Ceram. Soc.* **94**, 3605–3628 (2011).
37. Thévenot, F. Boron carbide—A comprehensive review. *J. Eur. Ceram. Soc.* **6**, 205–225 (1990).
38. Chen, M. W., McCauley, J. W., LaSalvia, J. C. & Hemker, K. J. Microstructural Characterization of Commercial Hot-Pressed Boron Carbide Ceramics. *J. Am. Ceram. Soc.* **88**, 1935–1942 (2005).

39. Werheit, H., Leithe-Jasper, A., Tanaka, T., Rotter, H. W. & Schwetz, K. A. Some properties of single-crystal boron carbide. *J. Solid State Chem.* **177**, 575–579 (2004).
40. Oganov, A. R. *et al.* Ionic high-pressure form of elemental boron. *Nature* **457**, 863–7 (2009).
41. Laubengayer, A. W., Hurd, D. T., Newkirk, A. E. & Hoard, J. L. Boron. I. Preparation and Properties of Pure Crystalline Boron. *J. Am. Chem. Soc.* **65**, 1924–1931 (1943).
42. Hoard, J. L., Geller, S. & Hughes, R. E. On The Structure of Elementary Boron. *J. Am. Chem. Soc.* **73**, 1892–1893 (1951).
43. Hoard, J. L., Hughes, R. E. & Sands, D. E. The Structure of Tetragonal Boron. *J. Am. Chem. Soc.* **80**, 4507–4515 (1958).
44. Sands, D. E. & Hoard, J. L. RHOMBOHEDRAL ELEMENTAL BORON. *J. Am. Chem. Soc.* **79**, 5582–5583 (1957).
45. Decker, B. F. & Kasper, J. S. The crystal structure of a simple rhombohedral form of boron. *Acta Crystallogr.* **12**, 503–506 (1959).
46. McCarty, L. V. V *et al.* A New Crystalline Modification of Boron. *J. Am. Chem. Soc.* **80**, 2592 (1958).
47. Talley, C. P., La Placa, S. & Post, B. A new polymorph of boron. *Acta Crystallogr.* **13**, 271–272 (1960).
48. Wentorf, R. H. H. & Wentorf Jr., R. H. Boron: Another Form. *Science* **147**, 49–50 (1965).
49. Eremets, M. I. *et al.* Superconductivity in Boron. *Science (80-.)*. **293**, 272–274 (2001).
50. Calandra, M., Vast, N. & Mauri, F. Superconductivity from doping boron icosahedra. *Phys. Rev. B* **69**, 224505 (2004).
51. Nagatochi, T. *et al.* Superconductivity in Li-doped α -rhombohedral boron. *Phys. Rev. B* **83**, 184507 (2011).
52. Shimizu, K. *et al.* Superconductivity in α -boron at Mbar pressure. *Phys. C Supercond.* **470**, S631–S632 (2010).
53. Boustani, I. New Convex and Spherical Structures of Bare Boron Clusters. *J. Solid State Chem.* **133**, 182–189 (1997).

54. Boustani, I. Systematic ab initio investigation of bare boron clusters: Determination of the geometry and electronic structures of B_n (n=2–14). *Phys. Rev. B* **55**, 16426–16438 (1997).
55. Boustani, I., Quandt, A., Hernandez, E. & Rubio, A. New boron based nanostructured materials. *J. Chem. Phys.* **110**, 3176–3185 (1999).
56. Wu, Y., Messer, B. & Yang, P. Superconducting MgB₂ Nanowires. *Adv. Mater.* **13**, 1487–1489 (2001).
57. Cao, L. M. *et al.* Well-Aligned Boron Nanowire Arrays. *Adv. Mater.* **13**, 1701–1704 (2001).
58. Otten, C. J. *et al.* Crystalline Boron Nanowires. *J. Am. Chem. Soc.* **124**, 4564–4565 (2002).
59. Ciuparu, D., Klie, R. F., Zhu, Y. & Pfefferle, L. Synthesis of Pure Boron Single-Wall Nanotubes. *J. Phys. Chem. B* **108**, 3967–3969 (2004).
60. Xu, T. T. *et al.* Crystalline Boron Nanoribbons: Synthesis and Characterization. *Nano Lett.* **4**, 963–968 (2004).
61. Zhang, D., Zhu, R. & Liu, C. Density functional theory study on the geometrical and electronic structures of a new thinnest boron nanotube. *J. Mater. Chem.* **16**, 2429–2433 (2006).
62. Yang, X., Ding, Y. & Ni, J. Ab initio prediction of stable boron sheets and boron nanotubes: Structure, stability, and electronic properties. *Phys. Rev. B* **77**, 41402 (2008).
63. Sato, Y. *et al.* Electron energy-loss and soft X-ray emission study of boron nanobelts. *J. Phys. Conf. Ser.* **176**, 12029 (2009).
64. Haussermann, U., Simak, S. I., Ahuja, R., Johansson, B. & Häussermann, U. Metal-Nonmetal Transition in the Boron Group Elements. *Phys. Rev. Lett.* **90**, 065701 (2003).
65. Solozhenko, V., Kurakevych, O. & Oganov, A. On the hardness of a new boron phase, orthorhombic γ -B₂₈. *J. Superhard Mater.* **30**, 428–429 (2008).
66. Van Setten, M. J., Uijtewaal, M. A., de Wijs, G. A. & de Groot, R. A. Thermodynamic stability of boron: the role of defects and zero point motion. *J. Am. Chem. Soc.* **129**, 2458–65 (2007).
67. Hayami, W. & Otani, S. First-principles study of the crystal and electronic structures of α -tetragonal boron. *J. Solid State Chem.* **183**, 1521–1528 (2010).

68. Werheit, H. & Kuhlmann, U. Is the established structure of α -rhombohedral boron correct? Comparative study of IR-active phonons with B₆O, B₄.3C and β -rhombohedral boron. *J. Phys. Condens. Matter* **24**, 305401 (2012).
69. Vlasse, M., Naslain, R., Kasper, J. S. & Ploog, K. Crystal structure of tetragonal boron related to α -AlB₁₂. *J. Solid State Chem.* **28**, 289–301 (1979).
70. Vlasse, M., Naslain, R., Kasper, J. S. & Ploog, K. The crystal structure of tetragonal boron. *J. Less Common Met.* **67**, 1–6 (1979).
71. Amberger, E. & Ploog, K. Bildung der gitter des reinen bors. *J. Less Common Met.* **23**, 21–31 (1971).
72. Ploog, K. & Amberger, E. Kohlenstoff-induzierte gitter beim bor: I-tetragonales (B₁₂)₄B₂C und (B₁₂)₄B₂C₂. *J. Less Common Met.* **23**, 33–42 (1971).
73. WILL, G. & PLOOG, K. Crystal structure of I-tetragonal boron. *Nature* **251**, 406–408 (1974).
74. Will, G. & Kossobutzki, K. H. X-ray diffraction analysis of B₅O₂C and B₅O₂N₂ crystal-lizing in the “tetragonal” boron lattice. *J. Less Common Met.* **47**, 33–38 (1976).
75. Hughes, R. E. *et al.* The Structure of β -Rhombohedral Boron. *J. Am. Chem. Soc.* **85**, 361–362 (1963).
76. Hoard, J. L., Sullenger, D. B., Kennard, C. H. L. & Hughes, R. E. The structure analysis of β -rhombohedral boron. *J. Solid State Chem.* **1**, 268–277 (1970).
77. Geist, D., Kloss, R. & Follner, H. Verfeinerung des β -rhomboedrischen Bors. *Acta Crystallogr. Sect. B Struct. Crystallogr. Cryst. Chem.* **26**, 1800–1802 (1970).
78. Prudenziati, M. Localized states in different samples of β -rhombo-hedral boron. *J. Less Common Met.* **47**, 113–117 (1976).
79. Callmer, B. An accurate refinement of the β -rhombohedral boron structure. *Acta Crystallogr.* **B33**, 1951–1954 (1977).
80. Slack, G. A., Hejna, C. I., Garbaskas, M. F. & Kasper, J. S. The crystal structure and density of β -rhombohedral boron. *J. Solid State Chem.* **76**, 52–63 (1988).
81. Slack, G. A., Hejna, C. I., Garbaskas, M. & Kasper, J. S. X-ray study of transition-metal dopants in β -boron. *J. Solid State Chem.* **76**, 64–86 (1988).
82. Hoard, J. L. & Newkirk, A. E. An Analysis of Polymorphism in Boron Based upon X-Ray Diffraction Results. *J. Am. Chem. Soc.* **82**, 70–76 (1960).

83. Bullett, D. W. Structure and bonding in crystalline boron and B₁₂C₃. *J. Phys. C Solid State Phys.* **15**, 415–426 (1982).
84. Longuet-Higgins, H. C. & de V. Roberts, M. The Electronic Structure of an Icosahedron of Boron Atoms. *Proc. R. Soc. A Math. Phys. Eng. Sci.* **230**, 110–119 (1955).
85. Prasad, D., Balakrishnarajan, M. & Jemmis, E. Electronic structure and bonding of β -rhombohedral boron using cluster fragment approach. *Phys. Rev. B* **72**, 195102 (2005).
86. Ogitsu, T. *et al.* Imperfect crystal and unusual semiconductor: boron, a frustrated element. *J. Am. Chem. Soc.* **131**, 1903–9 (2009).
87. Horn, F. H. Zone-Refined Boron. *J. Appl. Phys.* **30**, 1612 (1959).
88. Werheit, H., Laux, M. & Kuhlmann, U. Interband and Gap State Related Transitions in β -Rhombohedral Boron. *Phys. status solidi* **176**, 415–432 (1993).
89. R Schmechel & Werheit, H. Correlation between structural defects and electronic properties of icosahedral boron-rich solids. *J. Phys. Condens. Matter* **11**, 6803 (1999).
90. Häussermann, U., Mikhaylushkin, A. S. & Häussermann, U. Structure and bonding of γ -B(28): is the high pressure form of elemental boron ionic? *Inorg. Chem.* **49**, 11270–5 (2010).
91. Ploog, K., Schmidt, H., Amberger, E., Will, G. & Kossobutzki, K. H. H. B₄₈B₂C₂ und B₄₈B₂N₂, zwei Nichtmetallboride mit der Struktur des sog. I tetragonalen Bors. *J. Less Common Met.* **29**, 161–169 (1972).
92. Jemmis, E. D. & Balakrishnarajan, M. M. Polyhedral Boranes and Elemental Boron: Direct Structural Relations and Diverse Electronic Requirements. *J. Am. Chem. Soc.* **123**, 4324–4330 (2001).
93. Jemmis, E. D., Balakrishnarajan, M. M. & Pancharatna, P. D. A Unifying Electron-Counting Rule for Macropolyhedral Boranes, Metallaboranes, and Metallocenes. *J. Am. Chem. Soc.* **123**, 4313–4323 (2001).
94. Fujimori, M. *et al.* Peculiar Covalent Bonds in α -Rhombohedral Boron. *Phys. Rev. Lett.* **82**, 4452–4455 (1999).
95. He, J., Wu, E., Wang, H., Liu, R. & Tian, Y. Ionicities of Boron-Boron Bonds in B₁₂ Icosahedra. *Phys. Rev. Lett.* **94**, 15504 (2005).

96. Armstrong, D. R., Bolland, J. & Perkins, P. G. The electronic structure of α -B12, B12P2 and B12AS2. *Theor. Chim. Acta* **64**, 501–514 (1984).
97. Van Schilfgaarde, M. & Harrison, W. A. Electronic structure of boron. *J. Phys. Chem. Solids* **46**, 1093–1100 (1985).
98. Perrot, F. First approach to the band structure of α -rhombohedral boron. *Phys. Rev. B* **23**, 2004–2010 (1981).
99. Li, D., Xu, Y.-N. & Ching, W. Electronic structures, total energies, and optical properties of α -rhombohedral B12 and α -tetragonal B50 crystals. *Phys. Rev. B* **45**, 5895–5905 (1992).
100. Lee, S., Bylander, D. & Kleinman, L. Bands and bonds of B12. *Phys. Rev. B* **42**, 1316–1320 (1990).
101. Zarechnaya, E. Y. *et al.* Superhard Semiconducting Optically Transparent High Pressure Phase of Boron. *Phys. Rev. Lett.* **102**, 185501 (2009).
102. Terauchi, M., Kawamata, Y., Tanaka, M., Takeda, M. & Kimura, K. Electron Energy-Loss Spectroscopy Study of the Electronic Structure of α -Rhombohedral Boron. *J. Solid State Chem.* **133**, 156–159 (1997).
103. Garvie, L. A. J., Hubert, H., Petuskey, W. T., McMillan, P. F. & Buseck, P. R. High-Pressure, High-Temperature Syntheses in the B–C–N–O System. *J. Solid State Chem.* **133**, 365–371 (1997).
104. Ryen, L., Wang, X., Helmersson, U. & Olsson, E. Determination of the complex dielectric function of epitaxial SrTiO₃ films using transmission electron energy-loss spectroscopy. *J. Appl. Phys.* **85**, 2828 (1999).
105. Fujiwara, H. *Spectroscopic Ellipsometry: Principles and Applications*. 392 (John Wiley & Sons, Inc., 2007). at <http://www.wiley.com/WileyCDA/WileyTitle/productCd-0470016086.html>
106. McColm, L. J. *Ceramic Hardness*. (Plenum, 1990).
107. Saal, J. E., Shang, S. & Liu, Z.-K. The structural evolution of boron carbide via ab initio calculations. *Appl. Phys. Lett.* **91**, 231915 (2007).
108. Jacobsohn, L. G. & Nastasi, M. Sputter-deposited boron carbide films: Structural and mechanical characterization. *Surf. Coatings Technol.* **200**, 1472–1475 (2005).
109. Hitchcock, A. P. *et al.* Inner-Shell Excitation Spectroscopy of closo-Carboranes. *J. Phys. Chem. B* **101**, 3483–3493 (1997).

110. King, R. B. Three-dimensional aromaticity in polyhedral boranes and related molecules. *Chem. Rev.* **101**, 1119–52 (2001).
111. Chen, M., McCauley, J. W. & Hemker, K. J. Shock-induced localized amorphization in boron carbide. *Science* **299**, 1563–6 (2003).
112. Fanchini, G., Gupta, V., Mann, A. B. & Chhowalla, M. In Situ Monitoring of Structural Changes in Boron Carbide Under Electric Fields. *J. Am. Ceram. Soc.* **91**, 2666–2669 (2008).
113. Fanchini, G., McCauley, J. W. & Chhowalla, M. Behavior of Disordered Boron Carbide under Stress. *Phys. Rev. Lett.* **97**, 35502 (2006).
114. Lazzari, R., Vast, N., Besson, J. M., Baroni, S. & Dal Corso, A. Atomic Structure and Vibrational Properties of Icosahedral B₄C Boron Carbide. *Phys. Rev. Lett.* **83**, 3230 (1999).
115. Li, D. & Ching, W. Fundamental studies on the structures and properties of some B₁₂-based crystals. *Phys. Rev. B* **52**, 17073–17083 (1995).
116. Bylander, D. M. & Kleinman, L. Structure of B₁₃C₂. *Phys. Rev. B* **43**, 1487 (1991).
117. Bylander, D., Kleinman, L. & Lee, S. Self-consistent calculations of the energy bands and bonding properties of B₁₂C₃. *Phys. Rev. B* **42**, 1394–1403 (1990).
118. D. Emin, T. Aselage, C.L. Beckel, I.A. Howard & C.Wood. Boron-rich Solids. in *AIP Conf. Proc.* **140** (1985).
119. Hyodo, H. *et al.* Structure and electronic properties of Mg-doped β -rhombohedral boron constructed from icosahedral clusters. *Phys. Rev. B* **77**, 024515 (2008).
120. Gunji, S. & Kamimura, H. First-principles study on metal-doped icosahedral B₁₂ solids. *Phys. Rev. B* **54**, 13665–13673 (1996).
121. Jemmis, E. D. & Prasad, D. L. V. K. Icosahedral B₁₂, macropolyhedral boranes, β -rhombohedral boron and boron-rich solids. *J. Solid State Chem.* **179**, 2768–2774 (2006).
122. Teredesai, P. *et al.* High pressure phase transition in metallic LaB₆: Raman and X-ray diffraction studies. *Solid State Commun.* **129**, 791–796 (2004).
123. Young, D. P. *et al.* High-temperature weak ferromagnetism in a low-density free-electron gas. *Nature* **397**, 412–414 (1999).

124. McMillan, P. F. New materials from high-pressure experiments. *Nat Mater* **1**, 19–25 (2002).
125. He, D. *et al.* Boron suboxide: As hard as cubic boron nitride. *Appl. Phys. Lett.* **81**, 643 (2002).
126. Wang, Z., Zhao, Y., Lazor, P., Annersten, H. & Saxena, S. K. In situ pressure Raman spectroscopy and mechanical stability of superhard boron suboxide. *Appl. Phys. Lett.* **86**, 41911 (2005).
127. Hubert, H. *et al.* High-Pressure, High-Temperature Synthesis and Characterization of Boron Suboxide (B₆O). *Chem. Mater.* **10**, 1530–1537 (1998).
128. D. Emin *et al.* Boron-Rich solids. in *AIP Conf. Proc.* 231 (D. Emin, T. Aselage, A.C.Switendick, B.Morosin & C.L.Beckel.) 195,202 (1990).
129. Kresse, G. & Hafner, J. Ab initio molecular dynamics for liquid metals. *Phys. Rev. B* **47**, 558–561 (1993).
130. Emin, D. Structure and single-phase regime of boron carbides. *Phys. Rev. B* **38**, 6041–6055 (1988).
131. Mauri, F., Vast, N. & Pickard, C. J. Atomic Structure of Icosahedral B₄C Boron Carbide from a First Principles Analysis of NMR Spectra. *Phys. Rev. Lett.* **87**, 85506 (2001).
132. Balakrishnarajan, M. M., Pancharatna, P. D. & Hoffmann, R. Structure and bonding in boron carbide: The invincibility of imperfections. *New J. Chem.* **31**, 473–485 (2007).
133. Emin, D. Icosahedral Boron-Rich Solids. *Phys. Today* **40**, 55 (1987).
134. Beckel, C., Yousaf, M., Fuka, M., Raja, S. & Lu, N. Lattice vibrations of the icosahedral solid α -boron. *Phys. Rev. B* **44**, 2535–2553 (1991).
135. Mailhiot, C., Grant, J. & McMahan, A. High-pressure metallic phases of boron. *Phys. Rev. B* **42**, 9033–9039 (1990).
136. Lee, S., Kim, S., Bylander, D. & Kleinman, L. Crystal structure, formation enthalpy, and energy bands of B₆O. *Phys. Rev. B* **44**, 3550–3554 (1991).
137. Lee, S., Bylander, D. M. & Kleinman, L. Elastic moduli of B₁₂ and its compounds. *Phys. Rev. B* **45**, 3245 (1992).
138. Zhao, J. & Lu, J. Pressure-induced metallization in solid boron. *Phys. Rev. B* **66**, 092101 (2002).

139. Li, D. & Ching, W. Y. Electronic structure and optical properties of the B12O2 crystal. *Phys. Rev. B* **54**, 13616–13622 (1996).
140. Li, D. & Ching, W. Y. Electronic structures and optical properties of low- and high-pressure phases of crystalline B₂O₃. *Phys. Rev. B* **54**, 13616–13622 (1996).
141. Ching, W. & Li, D. Electronic structure and optical properties of Si-containing icosahedral boron crystals. *Phys. Rev. B* **57**, 3737–3740 (1998).
142. Schmid, H. K. Phase Identification in Carbon and BN Systems by EELS. *Microsc. Microanal. Microstruct.* **6**, 99–111 (1995).
143. Jiménez, I. *et al.* Photoemission and x-ray-absorption study of boron carbide and its surface thermal stability. *Phys. Rev. B* **57**, 13167–13174 (1998).
144. Ching, W.-Y. Electronic Structure and Bonding of All Crystalline Phases in the Silica-Yttria-Silicon Nitride Phase Equilibrium Diagram. *J. Am. Ceram. Soc.* **87**, 1996–2013 (2005).
145. Aryal, S., Rulis, P. & Ching, W. Y. Density functional calculations of the electronic structure and optical properties of aluminosilicate polymorphs (Al₂SiO₅). *Am. Mineral.* **93**, 114–123 (2008).
146. Ouyang, L. & Ching, W. Y. Electronic structure and dielectric properties of dielectric gate material (ZrO₂)_x(SiO₂)_{1-x}. *J. Appl. Phys.* **95**, 7918–7924 (2004).
147. Aryal, S., Rulis, P. & Ching, W. Y. Mechanism for amorphization of boron carbide B₄C under uniaxial compression. *Phys. Rev. B* **84**, 184112 (2011).
148. Wang, J. & Zhou, Y. Recent Progress in Theoretical Prediction, Preparation, and Characterization of Layered Ternary Transition-Metal Carbides. *Annu. Rev. Mater. Res.* **39**, 415–443 (2009).
149. Mo, Y., Rulis, P. & Ching, W. Y. Electronic structure and optical conductivities of 20 MAX-phase compounds. *Phys. Rev. B* **86**, 165122 (2012).
150. Hug, G., Jaouen, M. & Barsoum, M. X-ray absorption spectroscopy, EELS, and full-potential augmented plane wave study of the electronic structure of Ti₂AlC, Ti₂AlN, Nb₂AlC, and (Ti_{0.5}Nb_{0.5})₂AlC. *Phys. Rev. B* **71**, 024105 (2005).
151. Magnuson, M. *et al.* Electronic structure and chemical bonding in Ti₄SiC₃ investigated by soft x-ray emission spectroscopy and first-principles theory. *Phys. Rev. B* **74**, 195108 (2006).

152. Zhou, Y. & Sun, Z. Electronic structure and bonding properties in layered ternary carbide Ti_3SiC_2 ternary carbide Ti_3SiC_2 . *J. Phys. Condens. Matter* **12**, L457 (2000).
153. Mattesini, M. & Magnuson, M. Electronic correlation effects in the Cr_2GeC $\text{M}_{(n+1)}\text{AX}_x$ phase. *J. Phys. Condens. Matter* **25**, 035601 (2012).
154. Magnuson, M., Mattesini, M., Nong, N. Van, Eklund, P. & Hultman, L. Electronic-structure origin of the anisotropic thermopower of nanolaminated Ti_3SiC_2 determined by polarized x-ray spectroscopy and Seebeck measurements. *Phys. Rev. B* **85**, 195134 (2012).
155. Lofland, S. E. *et al.* Elastic and electronic properties of select M_2AX phases. *Appl. Phys. Lett.* **84**, 508 (2004).
156. Magnuson, M. *et al.* Electronic structure investigation of Ti_3AlC_2 , Ti_3SiC_2 , and Ti_3GeC_2 by soft x-ray emission spectroscopy. *Phys. Rev. B* **72**, 245101 (2005).
157. Jiang, J.-X., Jin, S., Wang, Z.-H. & Tan, C.-L. Electronic Structure and Optical Properties of Layered Ternary Carbide Ti_3AlC_2 . *Chinese Phys. Lett.* **28**, 037101 (2011).
158. Barsoum, M. W. & Radovic, M. Elastic and Mechanical Properties of the MAX Phases. *Annu. Rev. Mater. Res.* **41**, 195–227 (2011).
159. Eklund, P., Beckers, M., Jansson, U., Högberg, H. & Hultman, L. The $\text{M}_{n+1}\text{AX}_n$ phases: Materials science and thin-film processing. *Thin Solid Films* **518**, 1851–1878 (2010).
160. Shein, I. R. & Ivanovskii, a. L. Graphene-like titanium carbides and nitrides $\text{Ti}_{n+1}\text{C}_n$, $\text{Ti}_{n+1}\text{N}_n$ ($n=1, 2, \text{ and } 3$) from de-intercalated MAX phases: First-principles probing of their structural, electronic properties and relative stability. *Comput. Mater. Sci.* **65**, 104–114 (2012).
161. Ramzan, M., Lebègue, S. & Ahuja, R. Electronic and mechanical properties of Cr_2GeC with hybrid functional and correlation effects. *Solid State Commun.* **152**, 1147–1149 (2012).
162. Ramzan, M. & Ahuja, R. $\text{M}_{N+1}\text{AX}_N$ ($\text{M}=\text{Ti}, \text{A}=\text{Al}, \text{X}=\text{H}$) phase class materials with hydrogen: Ti_4AlH_3 and Ti_3AlH_2 . *Appl. Phys. Lett.* **96**, 261906 (2010).
163. Daoudi, B., Yakoubi, a, Beldi, L. & Bouhafs, B. Full-potential electronic structure of Hf_2AlC and Hf_2AlN . *Acta Mater.* **55**, 4161–4165 (2007).

164. Hug, G. Electronic structures of and composition gaps among the ternary carbides Ti_2MC . *Phys. Rev. B* **74**, 184113 (2006).
165. Xu, J. & Freeman, A. Band filling and structural stability of cubic trialuminides: YAl_3 , $ZrAl_3$, and $NbAl_3$. *Phys. Rev. B* **40**, 11927–11930 (1989).
166. Xu, J., Oguchi, T. & Freeman, A. Crystal structure, phase stability, and magnetism in Ni_3V . *Phys. Rev. B* **35**, 6940–6943 (1987).
167. Tanaka, I. & Mizoguchi, T. First-principles calculations of x-ray absorption near edge structure and energy loss near edge structure: present and future. *J. Phys. Condens. Matter* **21**, 104201 (2009).

VITA

Liaoyuan Wang was born in Hefei, Anhui, People's Republic of China. He was educated in local public schools. In 1998, he enrolled national self-education examination and earned his Bachelor Degree of computer information management in December 2001. Meanwhile, he studied in the Department of Physics at the University of Science and Technology of China (USTC). After five years of undergraduate study, he became a graduate student in the Department of Physics at USTC in 2003 and received the Master Degree of Science in 2006.

After short working in Beijing, Mr. Wang came to the University of Missouri-Kansas City under the direction of Curators' Professor of Physics Wai-Yim Ching. He started his interdisciplinary Ph.D. program in the autumn of 2007 with physics as his coordinating discipline and chemistry as his co-discipline. He earned his Master Degree of Science in Physics in December of 2010. In addition to completing the degree requirements, he also worked variously as teaching assistant in general physics laboratories and research assistant.

Mr. Wang is a member of the American Physical Society and American Ceramics Society. He has published four papers in several journals. He has also presented two conference talks and one poster.

PUBLICATIONS

1. **Liaoyuan Wang**, Paul Rulis, Wai-Yim Ching “Spectroscopic properties of crystalline elemental boron and the implications on B₁₁C-CBC” *RSC Advance* 3: 25374 (2013)
2. **Liaoyuan Wang**, Paul Rulis, Wai-Yim Ching “Calculation of core-level excitation in some MAX-phase compounds” *Journal of Applied Physics* 114, 023708 (2013)
3. Paul Rulis, **Liaoyuan Wang**, Ben Walker and Wai-Yim Ching “Spectral analysis of the electronic structure of γ -B₂₈” *Journal of Superhard Materials*, 33(6): 394-400 (2011)
4. Paul Rulis, **Liaoyuan Wang**, and Wai-Yim Ching “Prediction of γ -B₂₈ ELNES with comparison to α -B₁₂” *Phys. Status Solidi RRL* 3(5):133-135 (2009)
5. Master Thesis (in Chinese): **Liaoyuan Wang** “Photocatalysis and Self-clean Properties of Nano TiO₂ and Preparation for Self-clean Glass” USTC library (2006)
6. X.L. Xu, **L.Y. Wang**, L.F. Yan, M.T. Yang, and C.S. Shi, ”Characteristics of low lasing threshold Zn_{1-x}Mg_xO films grown by RF magnetron sputtering.” *Solid State Phenomena*, Vols. 121-123: 487-490 (2007)
7. X.L. Xu, **L.Y. Wang**, “Photoluminescence property of Zn_{1-x}Mg_xO films grown by RF magnetron sputtering” *Chinese Journal of Functional Materials*. 36(1) : 319-321 (2006)